Mapping the Redistribution of Jet Energy in PbPb Collisions at the LHC with CMS

by

Christopher Francis McGinn

B.A., Columbia University (2013)

Submitted to the Department of Physics
in partial fulfillment of the requirements for the degree of

Doctor of Philosophy

at the

MASSACHUSETTS INSTITUTE OF TECHNOLOGY

September 2019

Author .....
Department of Physics
June 28, 2019

Certified by .....
Yen-Jie Lee
Associate Professor
Thesis Supervisor

Accepted by .....
Nergis Mavalvala
Associate Department Head

Mapping the Redistribution of Jet Energy in PbPb Collisions at the LHC with CMS

by

Christopher Francis McGinn

Submitted to the Department of Physics
on June 28, 2019, in partial fulfillment of the
requirements for the degree of
Doctor of Philosophy

Abstract

Quenched jets produced in heavy ion collisions at the LHC and reconstructed with the CMS detector are studied to understand the nature of interactions between hard-scattered partons and the simultaneously produced hot and dense medium, the Quark-Gluon Plasma (QGP). Jets are objects with color charge evolving through many energy scales, so are an excellent tool for scattering experiment in QGP, with potential to resolve quasiparticle structure and induce medium response. Redistribution of jet energy is quantified in two methods: measurement of transverse p_{T} of final state particles projected onto dijet azimuthal axis, and measurement of jet production cross sections in PbPb and pp as function of jet radius. Missing momentum shows recovery of lost energy when moving beyond the jet cone for a fixed collection of jets, approaching full recovery at a $\Delta\mathrm{R}=\sqrt{\Delta\eta^2+\Delta\phi^2}$ of $\sim$2 in $\Delta\eta$-$\Delta\phi$s̃pace. A jet radius scan of jet production cross sections shows consistent observed suppression in PbPb when compared to appropriately scaled pp at all radii. However, less suppression is observed with increasing jet resolution parameter R. In combination the results imply that while jet energy lost to medium interactions can be found when looking beyond the jet cone, the substantial changes to the jet population in pp at each studied R lead to sustained spectral suppression with even the largest cone size.

Thesis Supervisor: Yen-Jie Lee
Title: Associate Professor

Acknowledgments

This thesis, and the work of the last six years, is dedicated to my physics family

- Alex Barbieri
- Anthony Badea
- Austin Baty
- Bolek Wyslouch
- Camelia Mironov
- Christof Roland
- Doga Gulhan
- Dragos Velicanu
- George Stephens
- Gian Michele Innocenti
- Gunther Roland
- Krisztian Krajczar
- Jing Wang
- Kaya Tatar
- Mukund Varma
- Ran Bi
- Ta-Wei Wang
- Wit Busza
- Yen-Jie Lee

and my birth family, Carolyn, Walter, Mary, and John. The difference between the two is in name only.

Contents

Chapter 1

Introduction

The fundamental constituents of matter and their interactions is the longstanding focus of particle physics. Stable matter, as constitutes both reader and author, is largely proton and neutron nuclei encompassed by electron clouds. While the electron is a fundamental particle, the nucleons we know are in fact composites of fundamental particles, quarks and gluons. The interaction of quarks and gluons is described by the theory of Quantum Chromodynamics, or QCD. Under QCD, the gluon acts as boson force mediator for strong interactions, which occurs between all particles with color charge, which comes in three distinct colors red, blue and green. At the current density and temperature of the universe, the quarks and gluons are found in colorless states: color-anticolor in $q\bar{q}$ mesons or red-blue-green qqq baryons. The corresponding potential that must be overcome for them to exist freely exceeds the available thermal energy of the typical particle. This property is called color confinement. A simple potential model between two particles of color charge, say quarks, is

$$U(r) = ar^{-1} + br \tag{1.1}$$

encodes confinement in its linear. As radial distance increases the potential energy increases substantially such that it becomes energetically favorable to pull sea quark from vacuum and form a stable colorless configuration.

Using a phase diagram of QCD in Figure 1-1, this stable matter exists along the

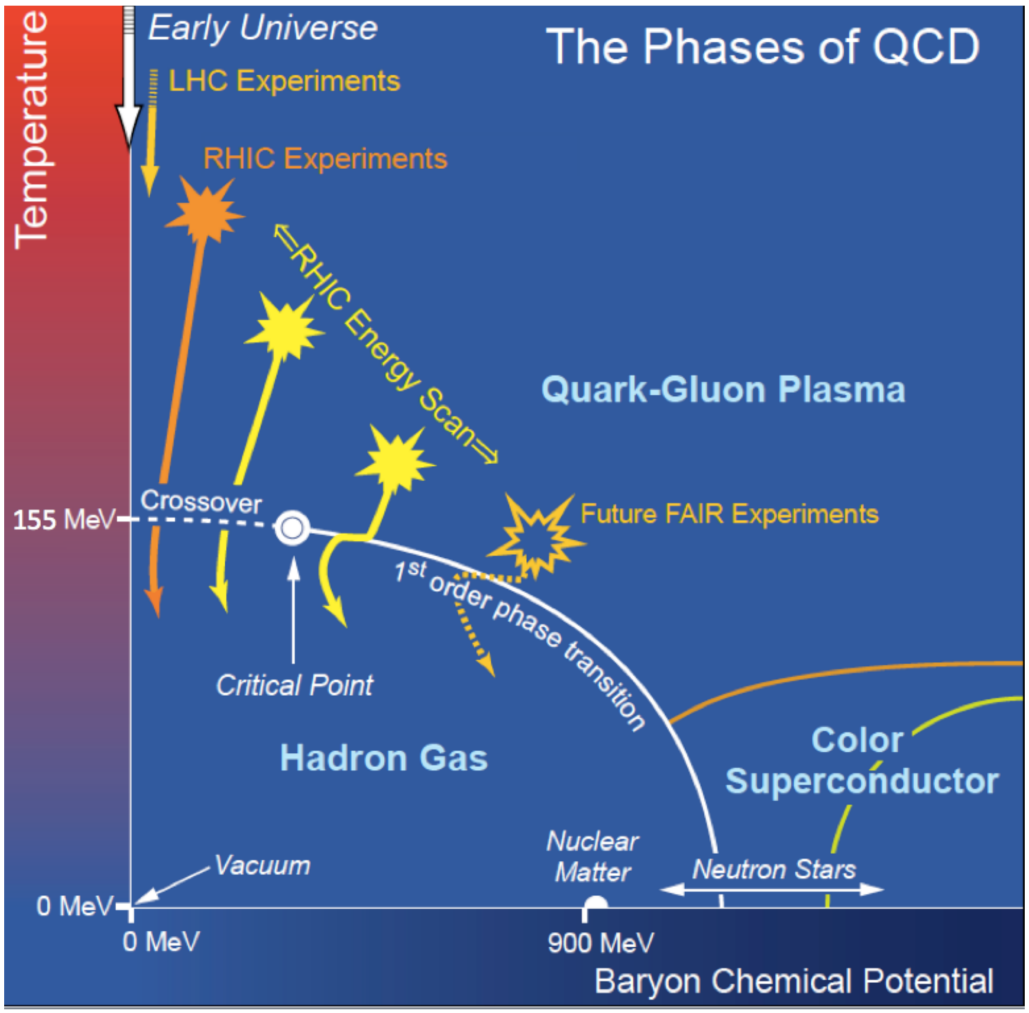

Figure 1-1: Phase diagram of QCD matter as taken from [1]. The phase space is plotted as a function of baryon chemical potential and medium temperature. The current universe exists along x-axis between vacuum point of 0-0 and nuclear matter of baryonic chemical potential equal to around ∼900 MeV. At comparably low temperature but increasing chemical potential, we reach phase of color superconductor probably cound be found at the center of neutron stars. The critical point in the phase diagram is not as yet known or understood and is subject of RHIC beam energy scan program. The QGP as currently explored at collider programs is found at low baryonic chemical potential but temperatures in excess of around 155 MeV.

x-axis, between baryon number density of vacuum to nuclear matter. However, in the early universe, at energy density far exceeding today, quarks and gluons existed deconfined. This state of matter was predicted by lattice QCD, and is known as the Quark-Gluon Plasma, or QGP. With the advent of modern collider physics programs, the QGP can be created and studied in the collisions of ultra-relativistic collisions of heavy ions. At the Large Hadron Collider (LHC) located at CERN, the QGP is produced at low baryonic density and temperature exceeding around 155 MeV, defining the phase crossover. The ongoing program at the Relativistic Heavy IonCollider (RHIC) studies QGP at a range of temperatures and baryonic chemical potentials as part of the beam energy scan search for the yet unknown critical point. In combination, these programs seek clear understanding of this heretofore inaccessible state of matter in hopes it will lead to fundamental insights into the nature of the strong interaction, particularly in the non-perturbative regime.

To understand a bit better what is meant by this new state of matter, consider Figure 1-2, a chronological progression of the collision of nuclei as performed at the LHC or RHIC. In frame 1, or at time=-5 fm/c, the incoming nuclei are highly Lorentz contracted longitudinally. At frame 2, or 0 fm/c, the contracted nuclei collide. At this point, there is no QGP as there is a brief formation time (typically somewhere from 0.2 to 1 fm/c). However, this period is where the production of all hard scattering occurs, jets which will be used to probe the medium **??**. In frame 3, 5 fm/c or a short time after the initial collision, we now have a fully formed and expanding fireball. Note that the longitudinal expansion along the beam direction far exceeds the transverse expansion, so fire-tube is a more appropriate picture. Here quarks and gluons exist outside of the colorless configurations they are restricted to by the linear term in potential 1.1. Deconfined does not mean free. Tather, they behave collectively like a liquid. Finally, at frame 4, or long after the initial collision, the expanding fire-tube has begun to cool, deconfined quarks and gluons fragment and recombine into colorless configurations in a process called hadronization, and these final state particles free stream to detector for analysis.

So far, the existence of the medium in frame 3 is purely stated rather than demon-

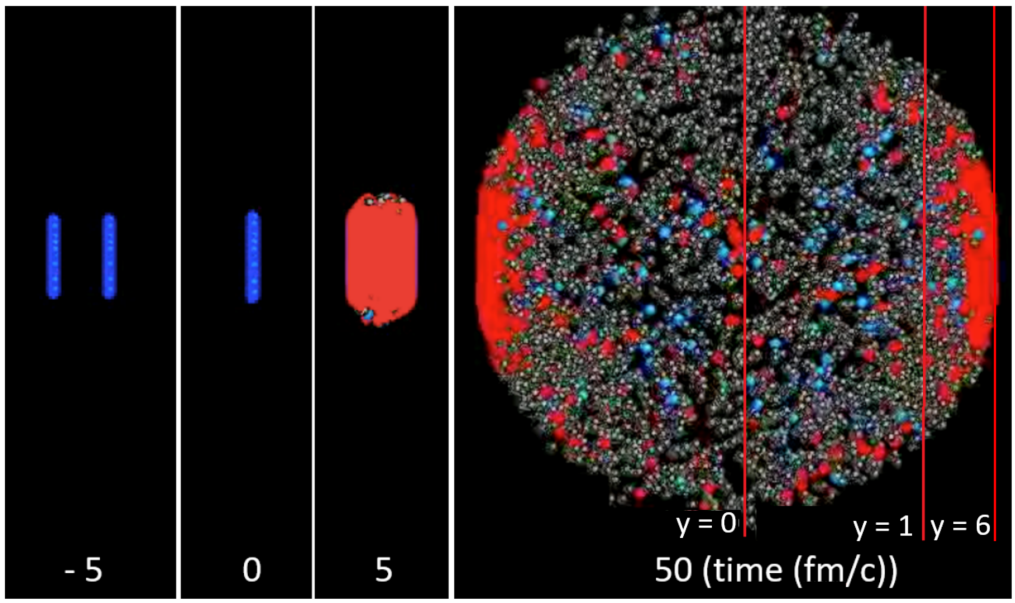

Figure 1-2: A progression of colliding nuclei in four consecutive snapshots. At frame 1, pre-collision, the two nuclei are highly Lorentz contracted in the longitudunal direction to about .001 its transverse width. At frame 2, the collision occurs, although the QGP is not yet formed (there is a typical formation time on the order of 0.2-1.0 fm/c). Frame 3 shows the fully formed medium at 5 fm/c after initial collision. Finally, frame 4 shows the continuous medium formation at the very forward region of the expanding fireball, while mid-rapidity region has begun to freeze out, hadronize, and is following free-streaming trajectory to detector. Figure taken from [2], as adapted from [3].

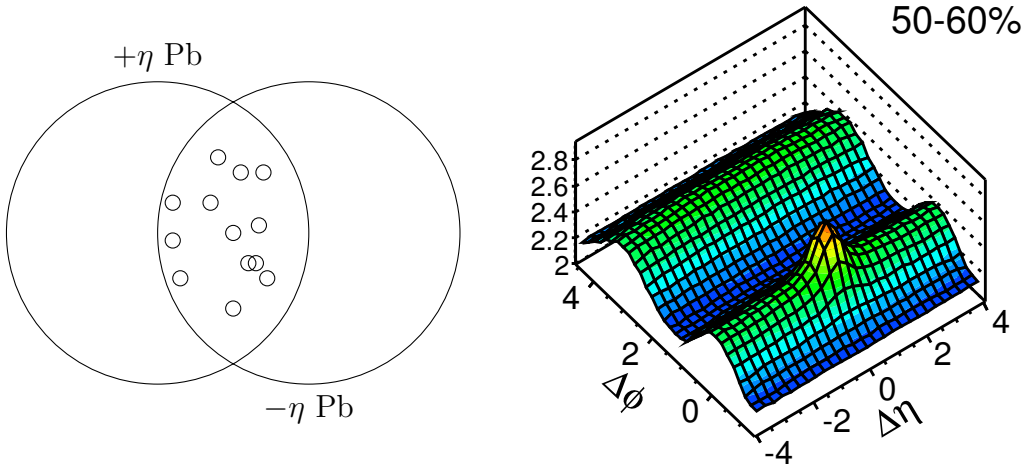

Figure 1-3: Left: Colliding nuclei in the transverse plane. The elliptical overlap region is where the particle production occurs, as result of many nucleon collisions. Right: The two-particle correlations in the final state as observed in [4].

strated. To motivate the existence of the medium, we wiill first consider soft phenomena. Figure 1-3 is a diagram of the colliding nuclei in the transverse plane. The elliptical overlap region contains many colliding nucleon pairs as represented by the smaller open circles in the overlap region. Nucleons of course also exist in the non-overlapping region, but here only interacting nucleons are shown. The final state that this produces is shown on the right hand side: a plot of two particle correlations in $\Delta\eta$-$\Delta\phi$ fully corrected for detector acceptance effects [4]. ϕ is the azimuthal angle defining 2π radians about the beamline. η is a convenient longitudinal coordinate related to relativistic velocity rapidity, y,

$$\begin{gathered} y = 0.5\ln(\frac{E-p_z}{E+p_z}) \rightarrow \text{Massless Limit} \rightarrow \eta = -\ln[\tan(\frac{\theta}{2})] \\ \eta = 0.0 \sim 90 \text{ from beamline},\ \eta = 1.0 \sim 45 \text{ from beamline} \end{gathered} \tag{1.2}$$

There are three distinct features to this correlation diagram: A peak at $\Delta\eta$-$\Delta\phi$ = 0-0, a ridge over all $\Delta\eta$ at π in azimuth, and a ridge over all $\Delta\eta$ at azimuth 0. The first and second of these are things expected from a superimposed set of fully uncorrelated nucleon collisions. They correspond to jet production (highly collumnated spray of particles corresponding to hard scattered parton) and balancing jet which will conserve transverse momentum but be decorrelated longitudinally. The third feature, or near side ridge, is not simply explained by superimposed uncorrelated interaction as each binary collision will produce particle isotropically relative to all others in the transverse plane. However, if you consider the elliptical overlap region, and then consider that rather than free streaming there was a finite interaction length in the final state, then the near side ridge is understood as:

1. Each collision of nucleons produces particles independently and isotropically relative all other collisions.

2. The initial overlap defines an elliptical region.

3. Rather than free streaming, there is a finite length scale defining interaction of quarks and gluons preventing diffusion, and the elliptical structure is preserved

thru to final state.

This is the soft physics evidence for new QCD matter. This phenomena is recently observed also in small systems such as pp and pA as well **??**. Search in e^+e^- and eA did not yield suchs signal **??**. Other evidence comes in the form of the sequential supperssion of charmonia and bottomonia states [5], and most relevant to this thesis, as jet quenching.

1.1 Jets as Parton Proxy

Jets are the final state proxy used in understanding the hard-scattered partons produced in collision events. Specifically, in say e^+e^- collisions, an e^+e^- annihilation to Z boson to final state $q\bar{q}$ pair cannot be measured as $q\bar{q}$, as the stable final state must be colorless and the two partons are recoiling from each other in the transverse plane. Instead, the quarks fragment and hadronize into highly columnated sprays of particles. The reconstructed final state is the jet. The fundamental problem of jet calculations and measurements, perhaps obvious from this definition, is that jets span many different energy scales. The perturbative techniques viable at one scale is not viable over the full evolution of the jet. This is related to the running coupling constant of QCD, α_S, which can be written as

$$\alpha_S(Q^2) = \frac{12\pi}{(11N_c - 2n_f)\log[\frac{Q^2}{\Lambda^2_{QCD}}]}. \tag{1.3}$$

As Q^2 goes to zero, the coupling constant diverges. As a result, a perturbative expansion in α_s will not converge at the low Q^2 termination point of the jets evolution. This behavior is confirmed in data extractions of α_S, as shown in Figure 1-4. The soft physics evidence for new state of matter of QGP resides in the low Q, high α_s regime, where perturbative technique fails because additional diagrams do not converge with higher orders of α_s. The hard-scattering however, exists at high Q, low α_s, has color charge, and is therefore a perturbative probe of QCD matter through most of its evolution.

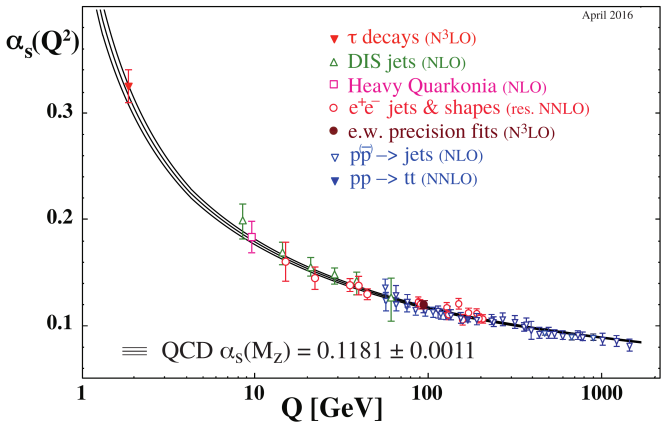

Figure 1-4: The evolution of α_s as a function of Q^2, as extracted from a global fit of many measurements. The divergence of α_s at low Q^2 leads to a breakdown in perturbative calculation, and alternative techniques are necessary. Figure taken from [6].

To extract properties of QCD from the hard-scattered partons, additional non-perturbative technique is needed without sacrificing the applicability of the perturbative technique at scale of initial scattering. The key to jet calculation is factorization, an unproven but well tested assumption, the minimal interference of amplitudes governing hard processes and soft processes should proceed with minimal interference. A jet production cross section in e^+e^- (the simplest possible jet production collision) which is nominally a mix of hard and soft processes can be written as

$$\frac{d\sigma_{jets}}{dz} = \frac{d\sigma_{partons}}{dz} \times D(z) \tag{1.4}$$

or the cross section for production of partons of some momentum times a fully factorized term accounting for the fragmentation and hadronization, D(z) (technically these processes are handled independently but for now we lump fragmentation of partons into more partons, and partons transitioning to colorless states together for simplicity). The term governing hard-scattered parton cross section is fully perturbative while the fragmentation and hadronization term must contain non-perturbative elements, as these processes terminate at low momentum scale. However, the probability distribution for the set of final state hadrons produced by a given hard-scattered

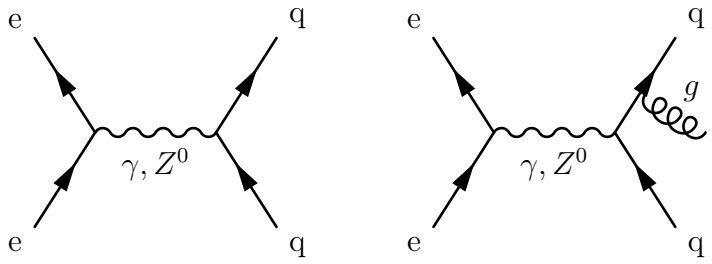

Figure 1-5: Diagrams for jet production in e^+e^- collisions as studied at LEP with detectors such as ALEPH. Three jet configurations were the first direct evidence for the existence of gluons. While an overall enhanced jet cross section or study of fragmentation patterns in proton-proton collisions might also point to the existence of the gluon jet, the absence of alternative sources of radiation in e^+e^- makes discovery here a prime choice.

parton is universal in vacuum, and its extraction in e^+e^- collisions can be applied to calculations in proton-proton collisions. The quenching physics of jets in PbPb therefore starts in the collisions of e^+e^-, where unmodified fragmentation functions are extracted and used to bridge the perturtbative evolution through to non-perturbative regime. While the key to this bridge, factorization, is again unproven assumption, it is both throroughly and constantly tested in pp, pA, and AA in many different center of mass energies and is reliable only on this basis.

1.2 Jets in pp

The QGP was originally proposed by Bjorken as a possible physics effect in the collision of single protons [7], a source of modification relative to e^+e^- to be accounted for in jet measurement. While recent measurements of high-multiplicity proton-proton collisions provide evidence for the collective behavior, signature of the QGP, this represents a small fraction of the total proton collision cross section [8]. Thus far jets produced in proton-proton and proton-Pb collisions are observed with no apparent quenching even within this high multiplicity subset **??**. Review of Bjorken's proposal show a mistaken factor overestimated the effect in proton-proton, so this is expected. However, while we use proton-proton as reference point for all medium effects, there are still significant complications in the collisions of hadrons compared to e^+e^-.

In comparison to the relatively simple set of Quantum Electrodynamic (QED)

processes for the production of jets in e^+e^- collisions as shown in Figure 1-5, the leading order set of QCD processes for inclusive jet production is more complicated. At leading order, final states of both quark and gluon initiated jets. Figure 1-6 provides a sample set of diagrams for these processes. Indeed, while there is some momentum and rapidity dependencies to the production of jets of a specific parton flavor, the rough fraction is 60% gluon, and 40% quark, at LHC $\sqrt{s_{NN}}$=5.02 TeV, for jets of energy ∼100 GeV.

The set of QCD diagrams also points to an additional complication - the diagrams are for quark and gluon scatterings, but the actual colliding particles are protons. While in e^+e^-, the collisions are relatively clean, the proton collisions seek to pick out constituent fundamental partons. Thus the equation governing jet production cross section introduces additional (but still factorizable) terms

$$\frac{d\sigma_{jets}}{dz} = \int dx_1 dx_2 g(x_1) g(x_2) \frac{d\sigma_{x_1,x_2}}{dz} \times D(z) \tag{1.5}$$

where we have introduced parton distribution functions, or PDFs, for each incoming proton, $g(x_1)$, $g(x_2)$, and integrate over all possible parton momentum x_1 and x_2. The cross section of the parton hard-scattering is now a function of the selected parton momentum. PDFs must also introduce non-perturbative components. As in the case of fragmentation functions, the PDF for the proton is universal absent medium effects and extracted from a simpler collision system for application in proton-proton collisions. Specifically, the deep inelastic scatterings of electron-proton collisions probes the parton distribution functions of the proton. Parton distribution functions as extracted at HERA by the ZEUS and H1 experiments is shown in Figure 1.2 [6].

Once parton distribution function is known at a given reference scale at the boundary of perturbative QCD, the evolution structure functions is defined in QCD by Dokshitzer-Gribov-Lipatov-Altarelli-Parisi (DGLAP) equations [9, 10, 11]. Combining measured parton distribution functions with DGLAP evolution defines the hard parton scatterings. When jets are described as a well-calibrated probe for medium effects, it explicitly refers to the extensive testing of PDF factorization, tests of frag-

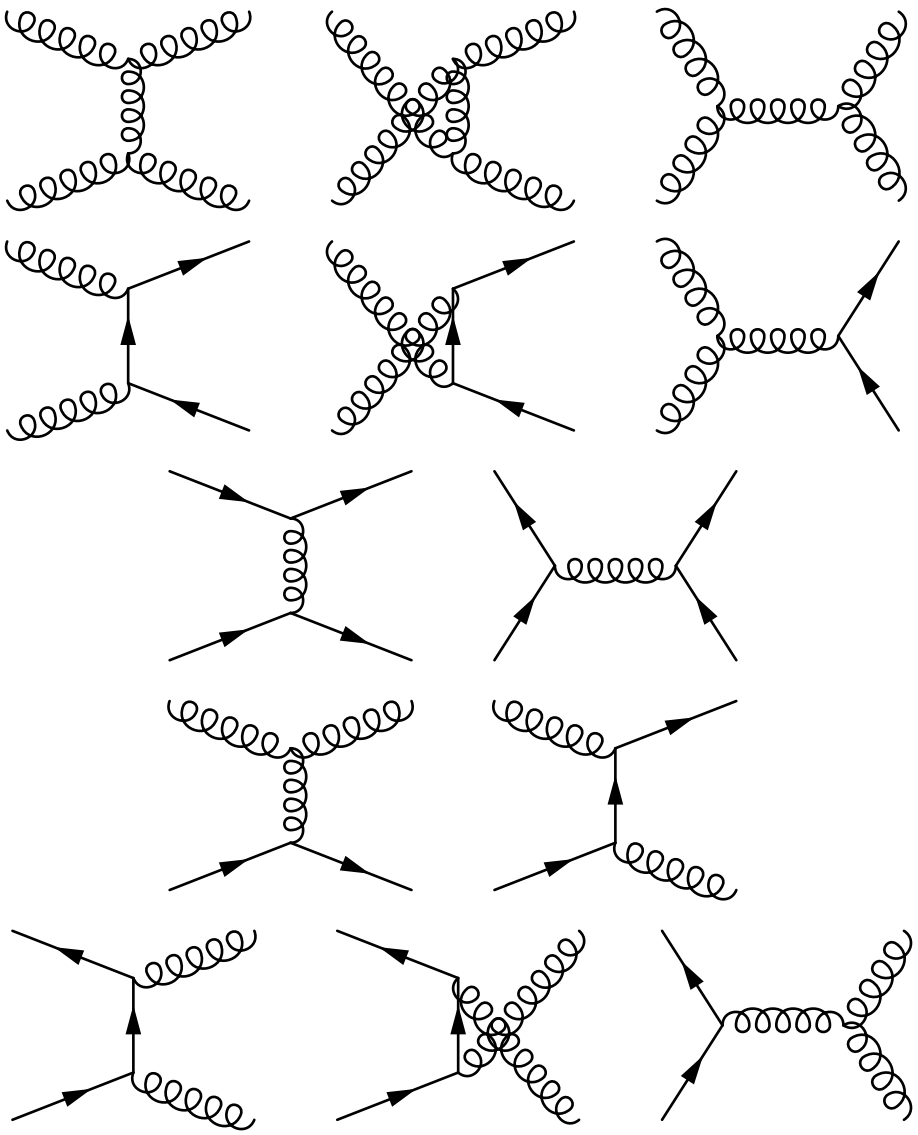

Figure 1-6: Diagrams for jet production in pp collisions as studied at LHC with detectors such as CMS. Unlike in e^+e^-, at LHC energies gluon jets dominate the inclusive jet production for a wide range of momentum.

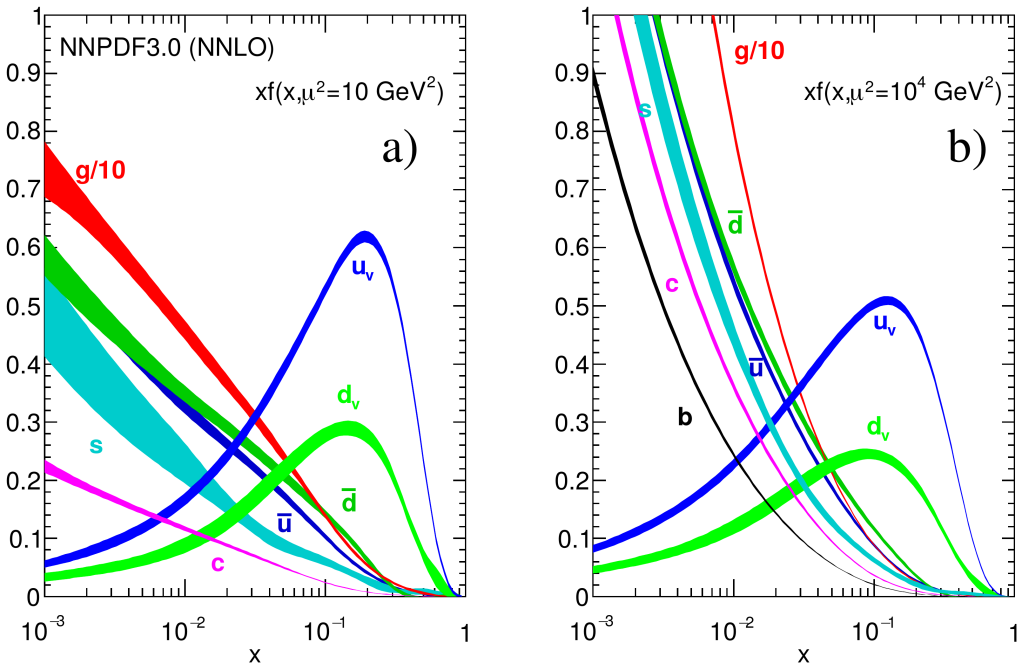

Figure 1-7: Parton distribution functions at two different Q^2 (here labeled μ^2) of 10 GeV^2 and 10^4 GeV^2. Note that with the increase in energy scale, the structure of the proton is more finely resolved and the relative contributions from gluon sea quarks to the momentum increases substantially. Figure via [6].

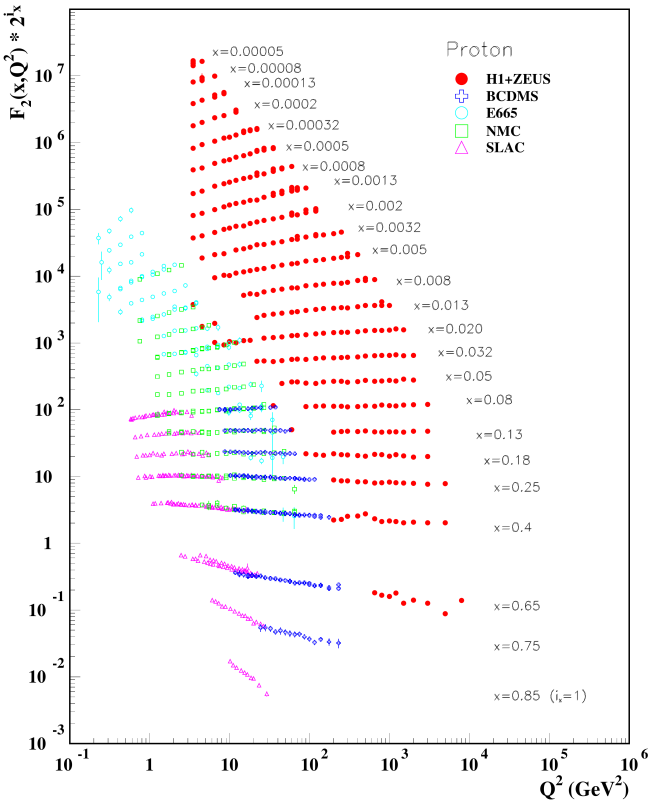

Figure 1-8: A demonstration of Bjorken scaling and the regimes in which it fails. While for many different Q^2, f(x, Q^2)=f(x), i.e. the structure function is flat, there is clear pronounced slop in some regime where higher order corrections break the scaling. Figure via [6]

mentation factorization, and the widely available study of production cross sections in proton-proton collisions at many different $\sqrt{s}$.

1.3 Jets as Probe of QCD Matter

The hard-scattered partons produced in collisions of nuclei are an essential probe of the medium, akin to a bullet through gel. Thorough study of jets in pp and e^+e^- make it a well-calibrated probe of the QGP matter. As a jet is a object with color charge with evolution from perturbative to non-perturbative scale, it is a complete probe of QCD matter interactions. In its simplest form, a jet program for study of QGP would follow the construction of the Bethe-Bloch curve, as shown in Figure 1-9. The

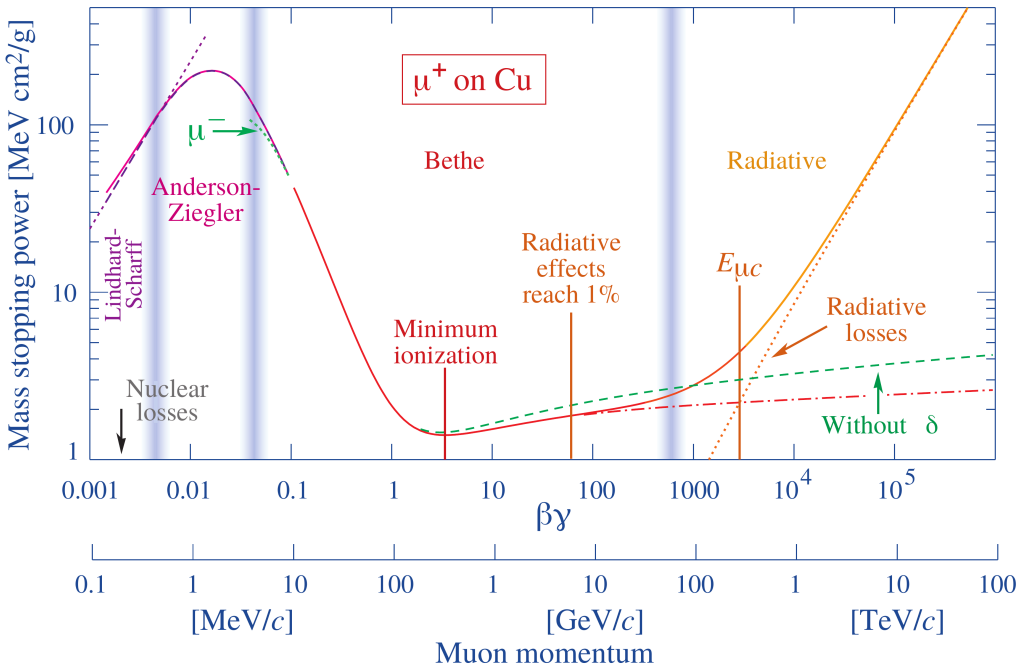

Figure 1-9: Bethe-Bloch curves of energy loss for particles passing through stable matter of the universe today. The goal of a jet physics program in heavy ions is to produce a similar curve for QCD matter. Figure via [6].

construction of a dE/dx energy loss curve for QCD matter analagous to the Bethe-Bloch curve would (on a model dependent basis) constrain parameters defining the interaction strength. Jets are understood as interacting with the medium in two ways: 2-by-2 scatterings off of quasiparticles (well resolved individual quarks and gluons in an otherwise continuous medium), and medium induced radiation of gluons. The two interactions are shown in Figure 1-10. The former can be handled fully perturbatively, and in some sense represents a weakly coupled, Rutherford picture of the medium, and formulated in, as not comprehensive example, BDMPS and AMY [12, 13, 14, 15, 16]. Other formulations can be found in [17]. The latter is typically limit of strong coupling, is not handled naturally perturbatively, and does not treat the medium as containing resolvable quasiparticles. Which mechanism dominates energy loss has distinct implications for the observed final state modification of jets.

These mechanisms are encoded as part of different Monte Carlo jet quenching models, meant to capture different physics. In addition to the implementation of

Figure 1-10: Left: Energy loss by 2-by-2 interactions with resolvable quasiparticles in the medium. Right: Energy loss by medium induced gluon radiation. Interplay of these two possible mechanisms and treatment of the medium define most Monte Carlo quenching implementations.

these processes, quenching models are also defined by their treatment of redistributed energy in the medium: is it a trivial backreaction carried purely by the particles immediately involved in the energy loss, or does it induce more complicated structures, like the wake of a boat in water? As yet, which of these combinations fully defines the behavior of jets in medium is unresolved. However, generators are available to explore the phase space of possibilities. The extreme cases, a fully weak and fully strong coupling, are represented by JEWEL and Hybrid model [18, 19]. The former encodes quenching with perturbative 2-by-2 matrix elements, while the latter allows fragmenation to proceed fully weakly while medium induced gluon radiation is calculated non-perturbatively at strong coupling limit exploiting anti-de Sitter/conformal field theory correspondence (AdS/CFT). Specifically, the parton is a color-string and medium interaction inducing energy loss is a black hole horizon in a higher dimensional space. The gravity of the black hole pulls the string downward as it propagates thru the medium, and the strings final downward angle indicates the magnitude of the lost energy. Equation 1.6 is the extracted dE/dx,

$$\frac{dE}{dx} = -\frac{4}{\pi} E_{in} \frac{x^2}{x_{\text{stop}}^2} \frac{1}{\sqrt{x_{\text{stop}}^2 - x^2}} \tag{1.6}$$

where x_{stop} is the length whereby the black hole would fully consume the color string, x is the distance through which medium induces energy loss, and Ein governs quenching magnitude. The complexity of implementation is not as relevant, however, as the

encoded underlying process. JEWEL and Hybrid model represent the limiting cases of a fully weak and fully strong coupling between jet and medium. By looking for observables with distrinct predictions between the two, we can seek to distinguish the exact mix of contributing mechanism.

1.4 Jet Physics in Medium

1.4.1 Jet Physics in Medium at RHIC

RHIC at Brookhaven National Lab is a long-running program for the collision of heavy nuclei at ultra-relativistic energies and study of the resulting QGP. The initial observation of jet quenching occurred here, although it was done without a full jet reconstruction. Instead, high-p_{T} hadrons were used as proxy for jets [20], [21], [22]. As we will see in the review of the LHC program (specifically comparing Fig. 1-16 with Fig. 1-17), this is not a perfect proxy for all quenching effects, but sufficient for the discovery of suppression. In Figure 1-11, leading hadrons are selected above a cut on transverse momentum, and are correlated in azimuth with non-trigger reconstructed particle. In pp, this distribution has a clear double peak structure back-to-back in azimuth, as to be expected in the typical jet configuration conserving momentum. However, in the studying trigger particle correlations in the corresponding collision of gold nuclei, the balancing peak opposite by π in azimuth has disappeared completely. This is interpreted as the medium interaction suppressing the spectra of balancing particle for the given p_{T} selection.

1.4.2 Jet Physics in Medium at the LHC

With the first data-taking at the LHC in 2010, strong modification of dijets produced in PbPb collisions was observed relative to vacuum and medium embedded Monte Carlo by the ATLAS collaboration [23]. This first quenching observation with fully reconstructed jets was subsequently confirmed by the CMS collaboration with comparable measurement of dijet asymmetry along with studies of the lost energy employing

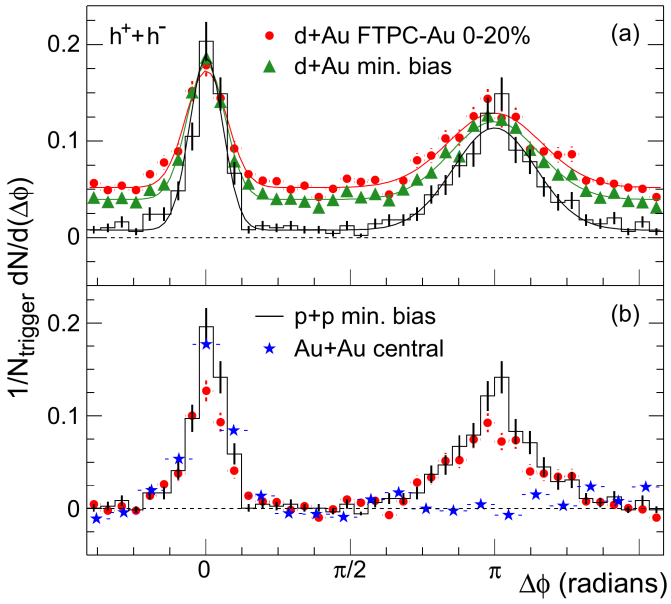

Figure 1-11: Observation of jet quenching through suppression of balancing hadrons in collisions of gold nuclei in the STAR collobration (first observation made by PHENIX, here use STAR for multiple system overlay). Trigger particles in pp have clear balancing distribution of particles back-to-back in azimuth by π. There is a comparable peak in collisions of deuteron with gold. However, in gold-gold collisions, this balancing distribution is absent. The above figure is from [20], which is a clearer re-plotting of the original observation in [21]. First observation was also made in PHENIX data [22].

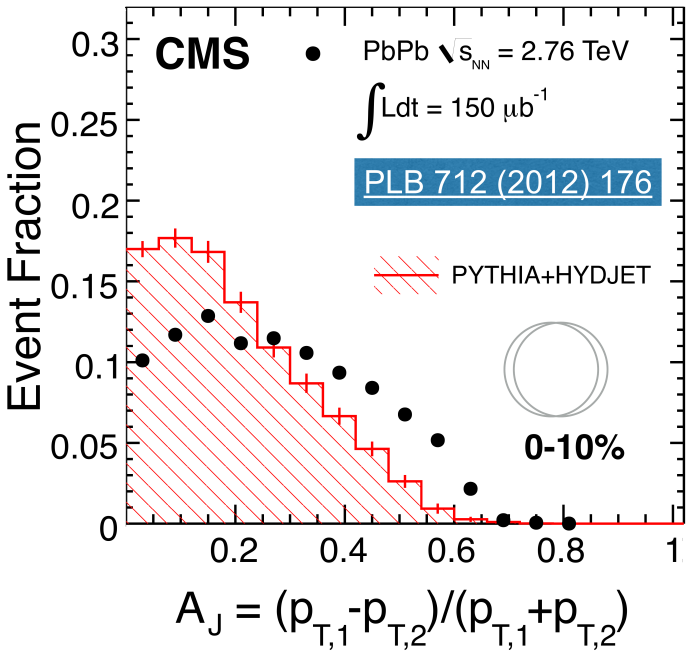

Figure 1-12: Dijet asymmetry as measured in PbPb collisions at $\sqrt{s_{NN}}$=2.76 TeV. Asymmetry is defined as difference of leading jet p_{T} with subleading p_{T}, normalized by the sum, as defined in Eq. 1.7. Strong modification in central PbPb events is observed when compared to appropriate Monte Carlo and resolution smeared proton-proton reference [24].

missing p_{T} techniques [24]. Since these initial observations a wealth of measurements of jet properties by CMS [25, 26, 27, 28, 29, 30, 31], ATLAS [32, 33, 33, 34, 35, 36], and ALICE [37, 38, 39, 40, 41] using inclusive jet production alone that have inspired many theoretical and phenomenological models predicated on understanding the underlying mechanism by which jets interact with the produced medium (QGP) and lose energy [19, 42, 43, 44, 18, 45, 45, 46, 47].

Figure 1-12 is adapted from CMS study of dijet asymmetry [24], defined as

$$A_J = \frac{p_{T,1} - p_{T,2}}{p_{T,1} + p_{T,2}} \tag{1.7}$$

or the difference between leading and subleading jets per event divided by their sum. The observable has a few very nice characteristics for the first observation of this physics, specifically the cancellation of systematics associated with background sub-

traction in the numerator difference, and an additional cancellation of systematics from jet energy scale in the ratio. Compared to Monte Carlo available at the time, and later vacuum reference in pp collisions, it was clear that the per dijet pair asymmetry was dramatically enhanced in PbPb, and that the enhancement increased as events where selected to be more central. Here centrality is a measure of nuclear overlap by which magnitude of quenching effect can be tuned. It is defined in percentiles

$$100\% \rightarrow \text{Greater nuclear overlap; Increase medium strength} \rightarrow 0\% \tag{1.8}$$

Subsequent measurements can be categorized in a few different ways. The redistribution of jet energy both within and beyond the jet cone is typically done with jet+track correlations. Figure 1-13 shows measurements of jet shapes and fragmentation functions by CMS and ATLAS. Jet shapes measure the jet energy by track p_{T} sums in annuli proceeding outward from the jet core, while fragmentation functions count particle multiplicities in fractional bins of the jet p_{T} [48, 49]. In CMS, inclusive jet shape measurements now look far beyond the cone as inspired by study of jet energy loss to large angles with missing p_{T} technique, the results of which form one half of this thesis. Photon-tagged fragmentation functions as seen in the ATLAS study give a clean initial tag of the parton hard-scattering, as opposed to the inclusive case where jet is biased by its own propagation through the medium. A comparison of the γ tagged and inclusive fragmentation functions is plotted.

While dijet asymmetry is an excellent observable for initial discovery of jet quenching, it is a poor one for absolute quantification of energy loss. Since both leading and subleading jet are heavily modified by the medium, there is no unmodified tag of the initial hard-scattering momentum. For this, boson+jet studies are the gold standard, as shown in Figure 1-14. In this figure, the first ever measurement of Z-tagged jet quenching in PbPb is shown, as measured by CMS. In addition, photon-tagged jet quenching from ATLAS is shown, fully unfolded for detector effects. In combination, the two colorless tags offer the first possibility of absolute energy loss quantification.

Substructure measurements as showcased in Figure 1-15 can get at specific in jet

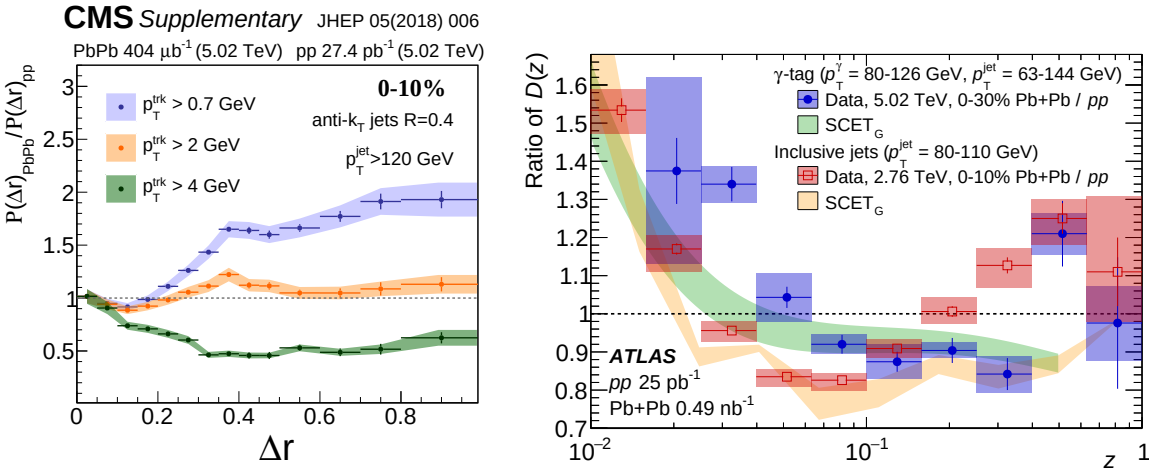

Figure 1-13: Jet shapes and photon tagged fragmentation functions as measured by CMS (Left) and ATLAS (Right) for inclusive jets and photon-tagged jets, respectively. The measurements partially map the redistribution of jet energy, inclusive jets for a roughly equal mixture of quark and gluon jets while photon tagged studies an enhanced quark jet sample. Inclusive jet distribution are taken out to far beyond the limit of the jet cone, showing compensating enhancement of soft particles to make up for high-p_{T} particle depletion [48, 49].

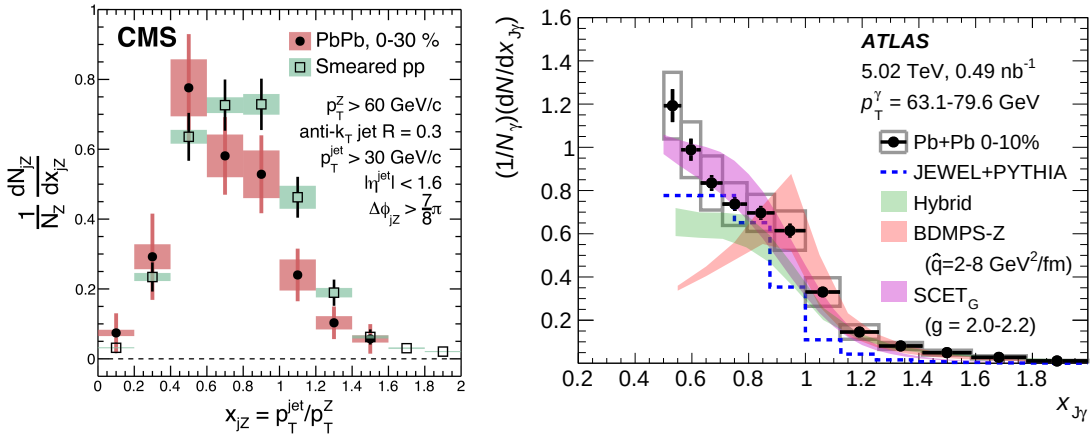

Figure 1-14: Boson-tagged jet p_{T} balance measurements by CMS (Left) and ATLAS (Right) using both the Z boson and photon. While Z boson is the current cleanest tag of the initial parton p_{T}, its production cross section is significantly smaller than that of the photon+jets. Both are free of surface biases that cause issues of interpretation in corresponding dijet p_{T} balance measurements [50, 51].

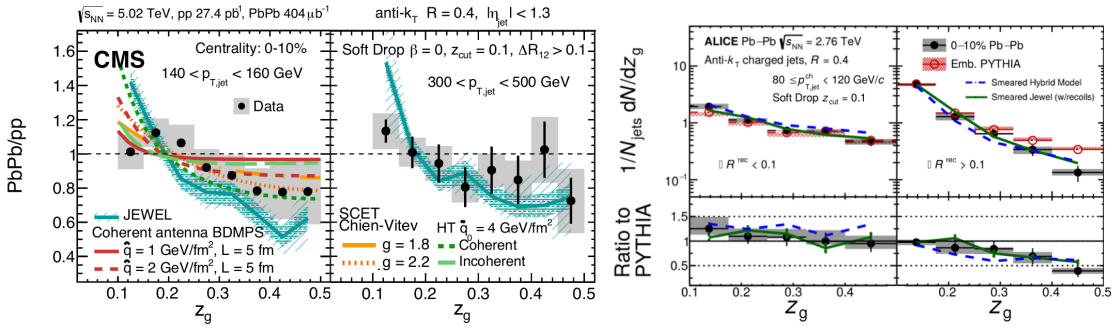

Figure 1-15: Splitting function measurement in PbPb and pp by CMS (Left) and ALICE (Right). z_g is defined as in Eq. 1.9. Both observe significant shape modification indicating that parton evolving in medium is found in a more columnated final state configuration than corresponding vacuum evolution. In addition, ALICE shows there is an overall suppression of jets reconstructed in this regime, suggesting even more jets fall below the z_g cut of 0.1 [52, 53].

modifications not easily understood with jet+track correlations alone. The splitting function, or z_g, is defined here as

$$z_g = \frac{p_{T,\text{Subjet2}}}{p_{T,\text{Subjet1}} + p_{T,\text{Subjet2}}} \tag{1.9}$$

is measured in this figure by both CMS and ALICE. Jet clustering is recursively reversed until a specific condition on subjet pair is satisfied (in this case that the subjet pair have z_g greater than 0.1). This ties directly to the resolution power of the medium. Taking as example a single parton radiating a gluon, or a gluon splitting into $q\bar{q}$, then there can exist an effect where they are so collinear that the medium would not resolve them as distinct, but rather as single color charge. In this case, while the jet itself would be quenched, the splitting function would be unmodified. The observed modification in PbPb splitting function by both ALICE and CMS confirms that there exists scales at which the medium resolves parton fragments as distinct. Follow-up study will likely search for phase space (either in subjet p_T or angle) where quenching is still observed but the splitting function reverts to its vacuum behavior. This will define a scale at which the medium cannot resolve color charges as distinct.

A final set of observables concerns production cross section of jets, or the correlated

production of large p_{T} hadrons. Figure 1-16 shows the nuclear modification factor for charged hadron production cross sections in pp as compared to appropriately scaled PbPb, defined as

$$R_{\mathrm{AA}} = \frac{d^2N^{AA}/dp_T d\eta}{T_{\mathrm{AA}}\ d^2\sigma^{PP}/dp_T d\eta}. \tag{1.10}$$

T_{AA} will be defined exactly in Analysis Chapter 7, but is effectively a factor for scaling from the pp collision to the number of colliding nucleons in a PbPb collision of a given nuclear overlap as defined by centrality. Colorless probes are currently observed to have R_{AA} of one, and thus all deviations come from medium effects. In charged particle R_{AA}, there is strong global suppression in the production of charged particles until the highest particle p_{T}, at which point the central value reaches 0.8 and is consistent with 1 in statistical and systematic error. While highly correlated with jet production, the high-p_{T} hadrons at best represent the hardest fragmenting subset of jets, and direct calculation is complicated by issues of fragmentation and hadronization. Jets are designed to minimize these issues. So how does this measurement compare to a corresponding measurement of jet production?

Figure 1-17 shows jet R_{AA} at the same $\sqrt{s_{_{NN}}}$=5.02 TeV as measured by the ATLAS collaboration. Here there is observed suppression even at the very highest jet p_{T}. In part this represents the many different scales that a fragmenting parton traverses, and while hard jets cores corresponding to highest p_{T} hadrons may undergo little to no change in medium, jet periphery and soft fragments still make up enough of a jets total p_{T} for modification to impact the measured cross section.

Figure 1-18 shows the measured jet spectra directly in pp and PbPb. The spectra is steeply falling which means even modest energy loss can result in substantial observed suppression. Some attempts at modeling (see [56]), show that a relative energy loss at low p_{T} of order 10%, decreasing to percent level at highest p_{T}, either according to logarithm or fractional power, can give reasonable qualitative agreement with the observed slow to flat recovery of jets. This also has implications for other inclusive jet measurements regarding potential biases when comparing vacuum jets and medium modified jets at identical energy cuts. In Figure 1-19, a toy example of

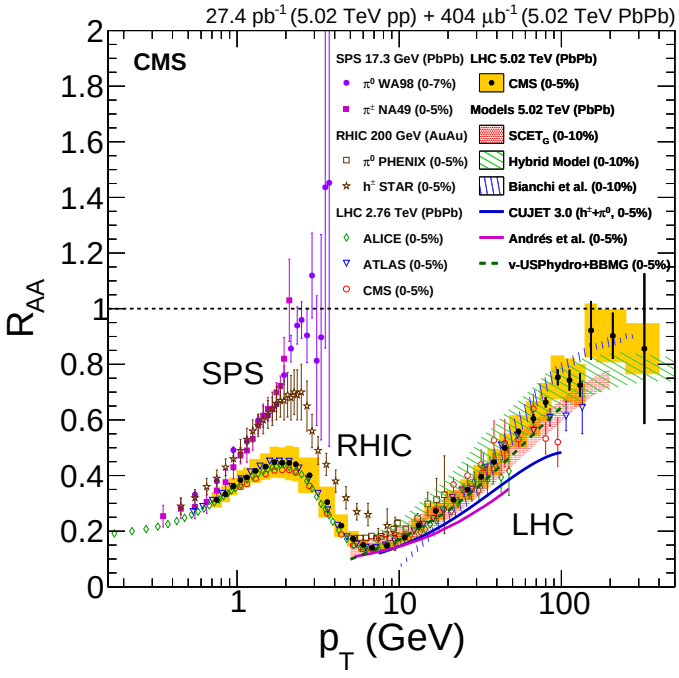

Figure 1-16: Charged particle R_{AA} from CMS for $\sqrt{s_{NN}}$=5.02 TeV in PbPb collisions, with some overlaid theory and comparable measurements from other experiments. Low p_{T} shows significant suppression, with some non-trivial structure. PbPb spectra relative pp starts monotonically increasing starting at roughly 10 GeV, approaching 0.8 and consistent with 1 at the 100-200 GeV range [54].

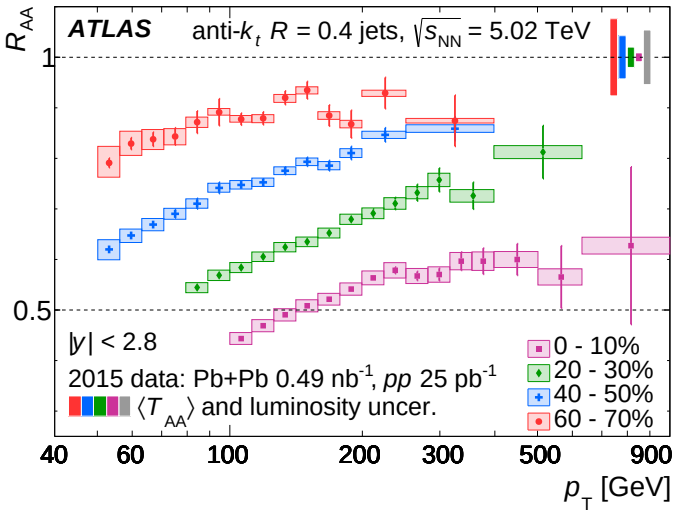

Figure 1-17: ATLAS Jet R_{AA} in PbPb collisions at$\sqrt{s_{NN}}$=5.02 TeV. Strong suppression of roughly factor 2 is observed over all p_{T} up to final bin of 630-1000 GeV [55].

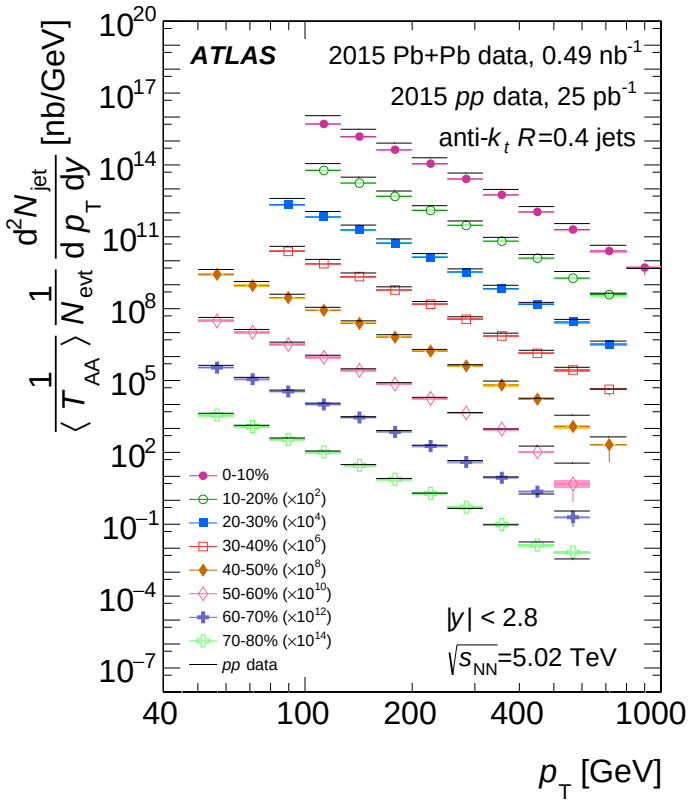

Figure 1-18: Spectra measurements corresponding to R_{AA} shown in Figure 1-17. The suppression of jet spectra observed acts to push the unquenched spectra left. Since these are also probability distributions and measurements of Z and γ R_{AA} suggest that initial hard-scatterings are to leading order unmodified, the lost spectra must be pushed to low p_{T} where we lose experimental control but would expect to observe jet enhancement [55].

jet spectra according to a power law is presented, with a second spectra produced with constant fractional energy loss, exaggerated for clarity.

The quenched spectra has energy loss with no fluctuations, which means every jet for a fixed p_{T} is quenched to identical new p_{T}. As a result, every jet shifts to the left by some value. So if comparing jets in pp at 120 GeV to jets in PbPb at matched transverse p_{T}, they would correspond to unquenched jets of 170 GeV. This mismatch, sometimes referred to surface or quenching bias, is inherent to many inclusive jet measurements. Boson-tagged measurements avoid this with colorless tag of the initial hard-scattering. R_{AA} seeks to directly measure this effect, so it is not

here a bias so much as it is the physics of interest. Dijet asymmetry, inclusive jet shapes, and even the missing p_{T} measurements exist but in context of this effect.

This bias in PbPb selection actually acts opposite the observed physics effect. As hard-scattering increases in energy in vacuum, final state tends to be more columnated. This can be seen by comparing jet shapes at different p_{T} in vacuum or considering the regime where boosted jet analysis of bosons decaying hadronically is viable lies between the boson mass such that decay products are boosted into single jet in lab frame and higher p_{T} where boson becomes so boosted that substructure is no longer resolvable. As such, if quenching is preferentially biasing towards object that are a-priori harder fragmenting and we still observe softer fragmentation patterns in the final state, then we are if anything underestimating the impact of the medium. This is also true in more subtle ways in using jet suppression as proxy for medium modification. If a fragmenting parton interacts with the medium, this energy will only be observed as "lost" if it is transported beyond the jet cone. Medium interactions that remain local will still be reconstructed as part of the jet.

While we observe strong suppression of jet spectra for R=0.4 resolution parameter, there are also hints that the energy can be recovered by looking beyond the jet cone. Does the full jet energy lost from medium interactions sit just beyond the edge of the jet itself, and could suppression be recovered by clustering at a modestly larger R? The answer as measured by all three experiments with heavy ion jet programs at the LHC thus far is no, as shown in Figure 1-20. Whatever R dependencies are observed appear fully self-consistent within systematic and statistical errors. However, these measurements are from the first data-taking, at a lower integrated luminosity and center of mass energy per nucleon. The ATLAS jet R_{AA} in Figure 1-17 has much higher p_{T} reach, where it is also possible to scan larger R. In this thesis, the first such reconstruction is shown in PbPb, to R=1.0, to study the suppression of jet spectra.

1.4.3 Big Jets in Little Plasma

Already there is a wealth of measurements on the quenching of hard-scattered patterns produced in QGP. Despite this abundance of measurements, a clear understanding of

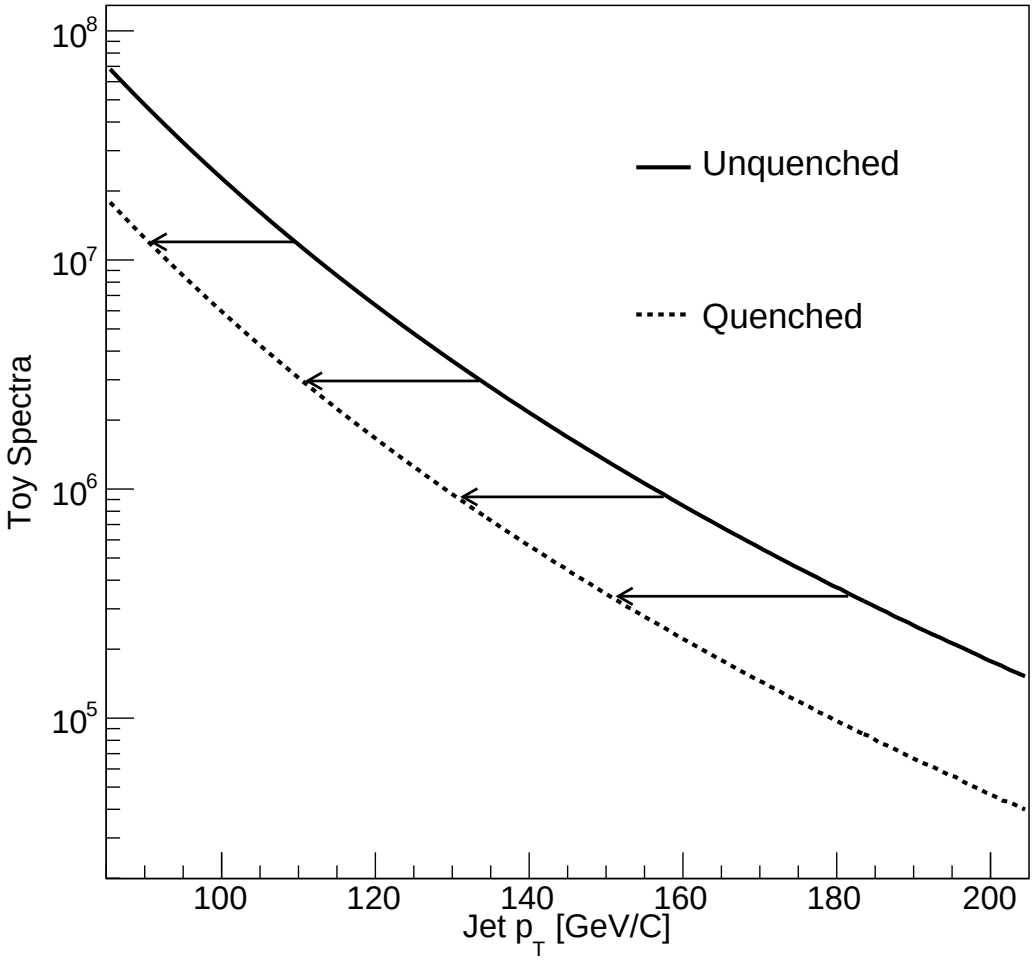

Figure 1-19: Toy depiction of impact of quenching on spectra. Here a power law is plotted with and without a constant fractional energy loss of zero width. The imposed energy loss serves to push the spectra leftward to lower p_{T}. The effect is two fold: first, suppression of high p_{T} jet spectra, and second, induced biases on jet p_{T} based selections. The latter is represented by leftward arrows - a selected vacuum jet at 150 GeV is compared to quenched jet that would correspond to vacuum value 180 GeV when p_{T} cut is held constant.

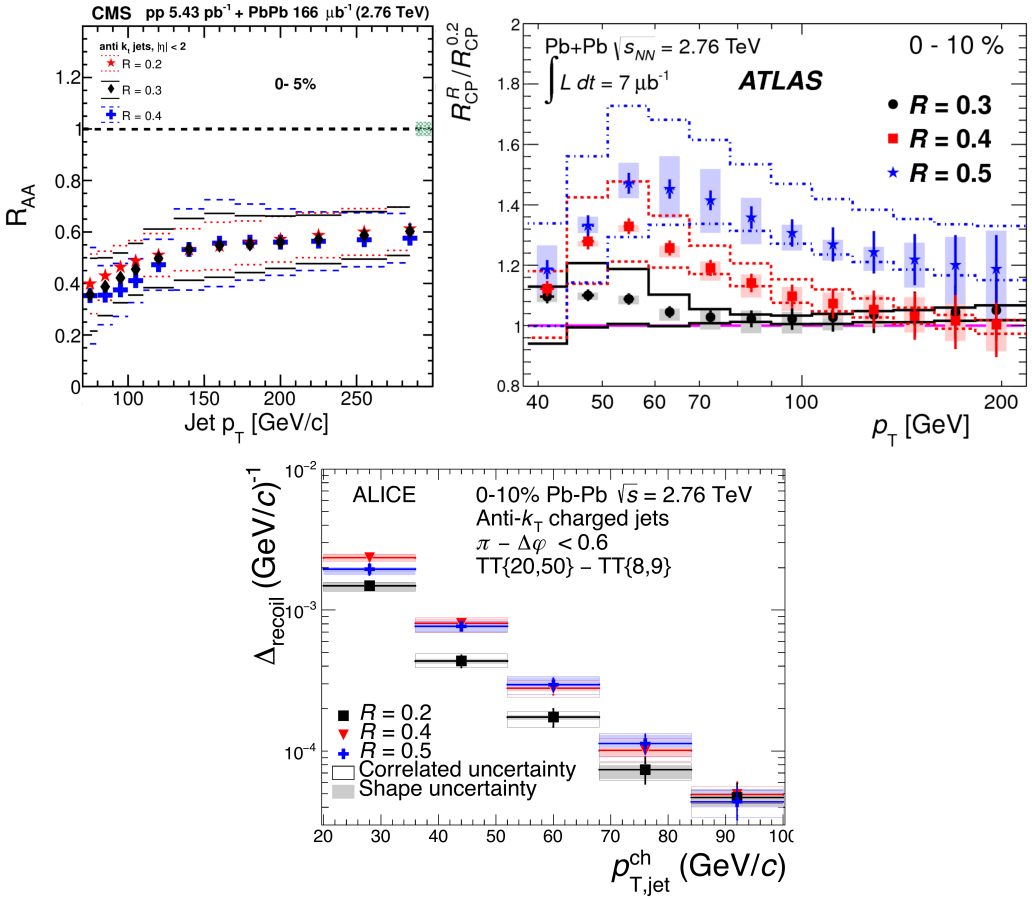

Figure 1-20: Radial scans of jet production in PbPb collisions at $\sqrt{s_{NN}}$=2.76 TeV by, left, CMS, middle, ATLAS, and right, ALICE experiments at the LHC [31, 32, 38]. No significant change in production is observed for the different choice of R as compared to either vacuum or peripheral PbPb reference points.

the nature of the underlying medium-parton interactions eludes the field. It is likely still wholly governed by QCD, so in that sense it is understood. However, taking as example say measurements of jet production cross section and its relative suppression in nuclear collisions, Monte Carlo generators encoding very different underlying aspects of QCD give results indistinguishable at the current experimental errors. This is clear in Figure 1-21. All four plots are distinct theory calculations that arrive at results consistent with currently available data on jet production cross sections (all current available data is limited to R $<=$ 0.5). This is true despite the fact that each calculation encodes very different mechanisms of energy loss. For example, JEWEL (bottom right) and Hybrid (top right) model calculations represent extreme ends of possible mechanisms. JEWEL is fully perturbative model of energy loss, where the quenching is the result of a 2-by-2 matrix scattering. In contrast, while parton shower in the Hybrid model proceeds fully as though it were in vacuum, the energy loss is per shower fragment is a continuous infrared radiation calculated by holography with fifth dimensional black hole pulling string down to event horizon. In other words, fully perturbative and non-perturbative models of energy loss, extreme cases of QCD, return an identical jet suppression [19, 43, 18, 45].

In order for the field to progress, serious consideration of observables with real discriminatory power between quenching mechanisms must be considered, even if they present serious experimental challenged. A wealth of measurements with great experimental control and zero discriminatory power already exists, and while they have value it diminishes absent discrimination. Furthermore, a greater effort must be made at attacking these models predictions rather than measuring first and than taking post-diction where adhoc parametrizations can be introduced to rescue excluded mechanisms. While Figure 1-21 is used to illustrate the discrimination problem for R=0.4, it also shows an observable satisfying the criteria above: a radial scan measuring the jet production cross section in pp and relative suppression in PbPb collisions. In this observable we have a set of clear predictions from all mechanisms, and real discriminatory power, particularly between the extreme cases of weak/strong couplings.

Despite this obvious opportunity, such a measurement has heretofore not been

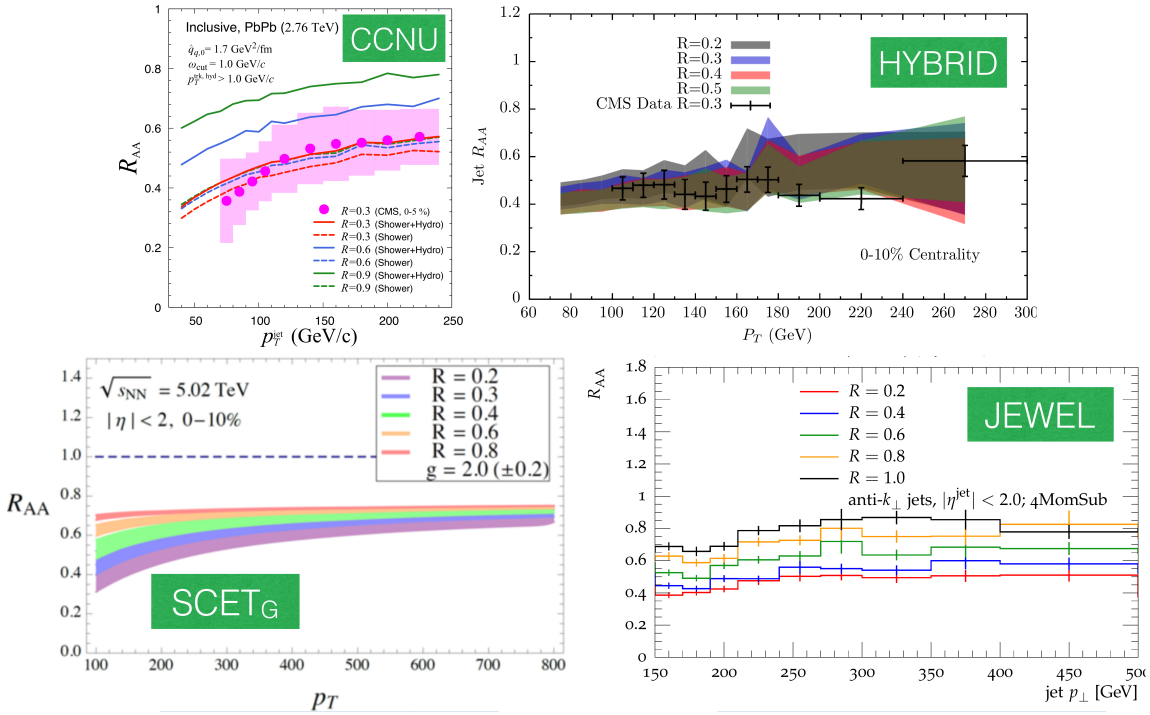

Figure 1-21: Theoretical expectations of a radial scan for different parton-medium interaction as encoded in Monte Carlo generators [43, 45, 46, 47].

attempted as the underlying event fluctuations in PbPb collisions threaten to swamp out signal with increasing R. However, with latest integrated luminosity of the 2015 data, where ATLAS has already observed persistent jet quenching up to 630-1000 GeV, we can avoid this problem by restricting our radial scan to high-p_{T} where the relative contribution of underlying event fluctuations are scaled away by the initial parton p_{T}, similar to the advent of full jet reconstruction when moving from RHIC to the LHC.

1.4.4 Big Questions in Little Plasma

There are in effect four primary questions for a jet program in QGP, one of which, the characteristic of energy loss by QCD Bethe-Bloch is already discussed. For completeness, the full list is

1. What is the characteristic energy loss of parton in medium (QCD Bethe-Bloch)?

2. How does collective behavior emerge from an asymptotically free theory such as QCD?

    - Alternatively, we know QCD is asymtotically free at high Q^2, and therefore we should see quasiparticles and Rutherford-like scatterings. Experimentally there is so far no evidence. Where is Rutherford hiding?

3. How is the energy lost by jets to the medium redistributed? Is it a trivial medium backreaction, or does it induce more complicated structures such as a wake?

In this thesis, using missing-p_{T} and jet radius scan of production cross sections and nuclear modification factors, we provide contributions to all. As we will see, missing-p_{T} has forced a more careful consideration of jet-medium interaction in the theory community, introducing concept of correlated background, or energy lost by jet to background that remains local to the jet itself in $\Delta\eta$-$\Delta\phi$, and is therefore still reconstructed as though unmodified. Likewise, jet radius scan of R_{AA} will provide real discriminating power between encoded medium energy deposition that is backreaction, and that with unduced structural complexity. Furthermore, if we observe a fully JEWEL-like behavior, it might be the first hint of Rutherford like scatterings, as the strong limit alone of Hybrid cannot replicate the behavior. Alternatively, an R_{AA} that is unity at a particular R that also has unmodified internal structure would indicate we've hit the fully quasiparticle regime, and have now completely mapped the strong$\rightarrow$weak coupling transition. Finally, this measurement will constrain the energy loss as a function of the initial parton broadness, as with the successive increase in jet cone, new populations of jets are introduced, each more broad than the last. How the medium interacts with the ever broadening populations of jets will tell us something about the weak-strong transition of the coupling, as the greater length scale displacement of the fragmenting parton will lend itself to an ever more resolvable internal structure by the medium, and likely induce greater energy loss.

Table 1.1: Sampling of jet quenching results at the LHC. Note that this only includes those that have been published. A set of relevant preliminary results (for example, ATLAS jet mass as contribution to substructure category) from all experiments are available but excluded from this table for now. Also excluded are results that are related to jet quenching but are exclusively at the hadron level. For example, at high p_{T}, charged hadron R_{AA} is almost entirely coming from jet production and observed modifications are likely the result of quenching, but as it doesn't involve actual jet reconstruction it is excluded from the table.

Physics Objects	System and Energy	Observables	References
Jet	PbPb 2.76 TeV	R_{AA}	[32], [37], [57], [34], [58], [38]
Jet	PbPb 2.76 TeV	$A_J$or x_J	[24], [25], [23], [58], [33]
Jet	PbPb 2.76 TeV	Jet Ang. Distributions	[33], [35], [39]
Jet	pPb 5.02 TeV	R_{pA}	[59], [60], [61]
Jet	PbPb 5.02 TeV	R_{AA}	[55], [62]
Jet+Track	PbPb 2.76 TeV	Frag. Functions	[63], [26], [36]
Jet+Track	PbPb 2.76 TeV	Particle Correlations	[28], [29]
Jet+Track	PbPb 2.76 TeV	Jet Shapes	[27], [30], [41]
Jet+Track	PbPb 5.02 TeV	Particle Correlations	[48]
Heavy Flavor Jet	PbPb 2.76 TeV	R_{AA}	[64]
Heavy Flavor Jet	PbPb 5.02 TeV	$A_J$or x_J	[65]
Boson+Jet	PbPb 2.76 TeV	$x_{J,\gamma/Z}$	[66]
Boson+Jet	PbPb 5.02 TeV	$x_{J,\gamma/Z}$	[50], [67], [51]
Boson+Jet+Track	PbPb 5.02 TeV	Frag. Functions	[68], [49]
Boson+Jet+Track	PbPb 5.02 TeV	Jet shapes	[69]
Jet Substructure	PbPb 5.02 TeV	Mass, z_g, etc.	[70], [52], [40], [53]

Chapter 2

The CMS Detector

2.1 Overview

The Compact Muon Solenoid, or CMS detector, is one of the four primary detectors currently operating at the Large Hadron Collider (LHC) along with ATLAS, ALICE and LHCb. The collider delivers collisions of protons with protons, protons with lead ions, lead with lead at many different center of mass energies. Recently in 2017, a previously unplanned set of collisions using Xenon nuclei were added. While the nominal program focused on discovery of the Higgs Boson and new physics beyond the standard model, this set of collision systems also provide a wealth of data for studying the QGP and the properties of QCD matter. The CMS detector is an ideal tool for studying the collisions delivered, with its fine granularity silicon pixel and strip tracking detector, strong magnetic field for good resolution up to the highest particle momentum, state of the art lead-tungstate electromagnetic calorimeter, hadron calorimeter, muon chambers, and forward calorimetry for pseudorapidity coverage of $\pm$ 5, in additional to fully symmetric azimuthal coverage. Figure 2-1 shows the detector with highlighted subdetector systems as originally conceived in the technical design report [71].

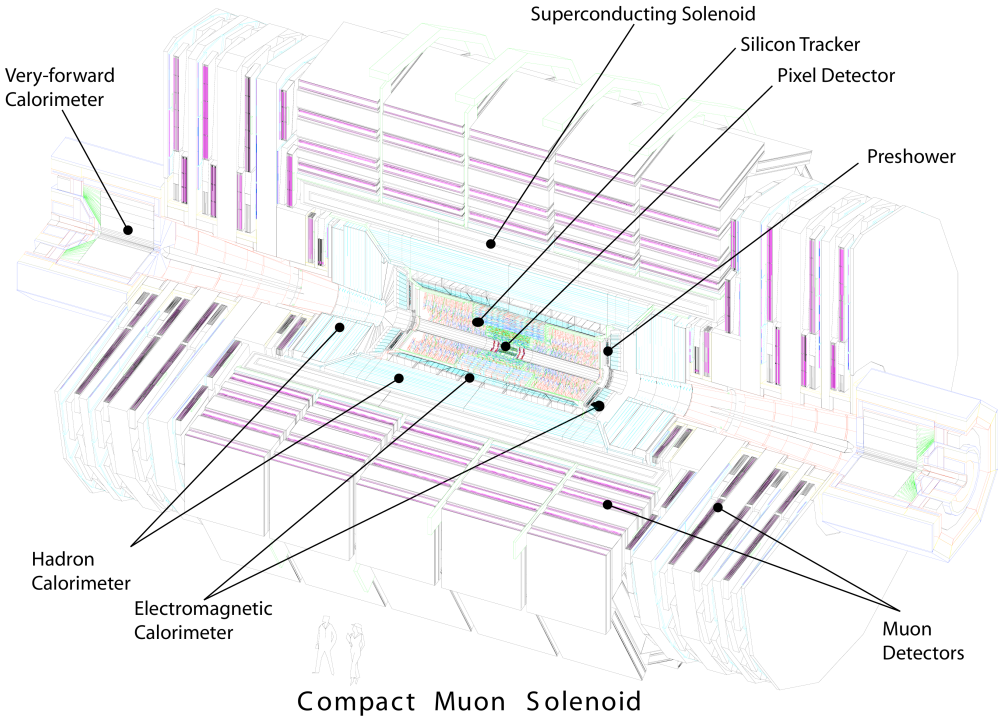

Figure 2-1: The CMS detector with select highlighted subsystems, as conceived in [71]. For jet physics, the most relevant subsystems are the silicon pixel tracker, lead-tungstate electromagnetic calorimeter, and hadronic calorimeter. The forward calorimetry is useful in heavy ion collisions in determining the impact parameter, using forward event activity as proxy.

2.2 Tracking

The CMS tracking subdetector is the interior-most, as the tracking measurements are non-destructive. The subdetector is divided into silicon pixel and strip detectors, with the former being interior where the particle fluxes per unit detector area is highest. Within the pixel and strip tracking subdetector division, a further division can be made between barrel and endcap tracking detectors. The exact geometry is as follows

1. Three discrete sets of silicon pixel detectors in a cylindrical configuration, spaced roughly 4, 7, and 11 centimeters from beamline

2. Two silicon pixel endcap rings, subtending annulus of 6 to 15 centimeter are placed 35 and 46 centimeters along beamline from interaction point

3. Tracker Inner Barrel (TIB): 4 layers of silicon strips in cylindrical annulus subtending 20 to 55 centimeters

4. Tracker Inner Disk (TID): Three silicon strip disks enclosing the TIB on either side, at longitudinal displacement from the interaction point of 60 to 120 centimeter

5. Tracker Outer Barrel (TOB): 6 layers of silicon strips in cylindrical annulus subtending 55 to 110 centimeters

6. Tracker Endcap (TEC): Nine silicon strip disks enclosing the TIB and TOB barrel strip detectors, enclosing 120 to 280 centimeters.

Note that the pixel detector maximum occupancy is on the percent level, even for heavy-ion collisions. It is the spatial resolution of the hadronic calorimeter that presents the most limitations on particle-level jet reconstruction. Furthermore, this subdetector provides charged particle vertex resolution of $\sim$20 micrometers. Given pileup collisions in pp are displaced longitudinally on the order of centimeters, this resolution is more than sufficient for the removal of underlying event in jets produced

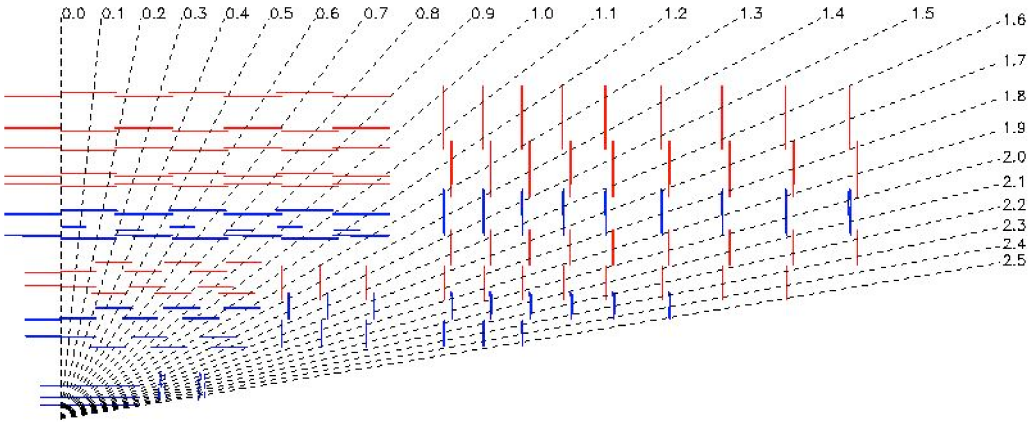

Figure 2-2: Cutaway schematic of tracker pseudorapidity coverage. Note that various tracking subdetectors (inner and outer barrel,) do not cover well defined pseudorapidity but rather have overlapping coverage (in contrast to the design of the barrel and endcap calorimetry). Tracker coverage extends out to pseudorapidity $\pm$ 2.5. While upgrade in 2017 extended silicon pixel detectors out to absolute pseudorapidity of 3, full tracking as used in jet reconstruction remains in this original forward range [71].

in pp collisions. However, the entire underlying event in a PbPb collisions is produced in a longitudinal region of about ten femtometer, and this subtraction is not viable.

As will be discussed further in Chapter 5, the tracking detector at CMS is an essential component in jet reconstruction. The substitution of tracks for calorimeter energy depositions in the jet reconstruction substitutes the superior detector for roughly sixty percent of the typical jets energy, with another 30% recovered in the CMS electromagnetic calorimeter. The remaining ten percent is remains in the HCal.

2.3 Calorimetry

Calorimetry is an essential component of most collider physics jet programs, as the highest momentum particles produced in the hard-scatterings of partons are best measured in a calorimeter. CMS follows the typical design of an onion detector, and thus its destructive, calorimeter detectors begin outside the tracking detectors, first electromagnetic followed by hadronic. Both measure significant fractions of the average jets energy.

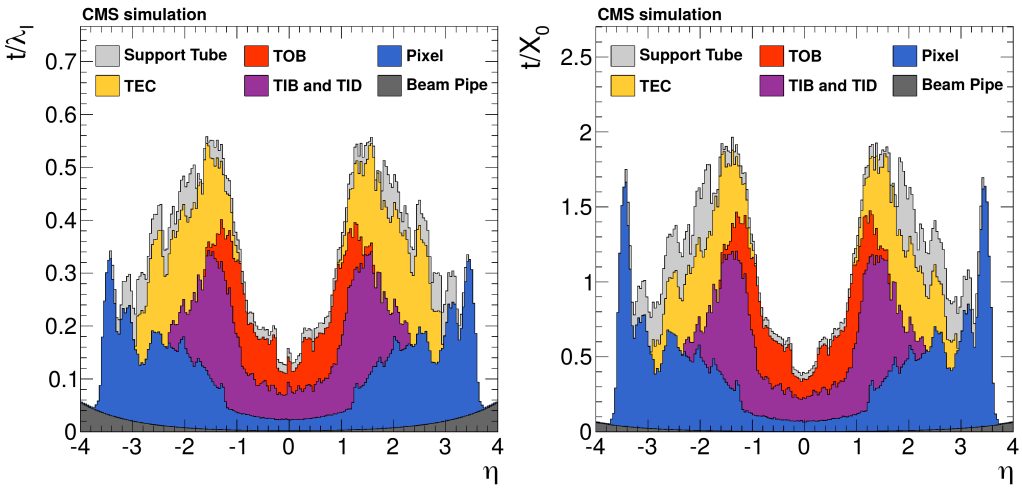

Figure 2-3: Material budget of the CMS detector before particles reach the calorimeters. This is partially responsible for the non-linearities in calorimeter response to jets, in addition to bending of softer particles in the magnetic field [72].

2.3.1 Electromagnetic Calorimetry

The CMS electromagnetic calorimeter (ECal) is both high in spatial granularity and has excellent energy resolution for particles interacting electromagnetically. The detector can be divided into two subdetector systems: the ECal Barrel (EB) and ECal Endcap (EE). The barrel extends thru pseudorapidity of $\pm$ 1.479, while the endcap continues coverage out to a pseudorapidity of $\pm$ 3, at which point the Hadron Forward calorimeter begins. The detector is comprised of lead-tungstate crystals, which at mid-rapidity gives a $\Delta\eta$-$\Delta\phi$ granularity of 0.0174 x 0.0174, corresponding to one-fifth of the spatial resolution of the hadronic calorimeter. This excellent spatial resolution is essential in implementing particle-flow algorithms for jet reconstruction, as clusters are used under hypothesis that they are product of single particles.

2.3.2 Hadronic Calorimeter

The CMS hadronic calorimeter (HCal) can be separated like the ECal into a barrel and forward region. The barrel extends thru pseudorapidity of $\pm$ 1.3, while the endcap continues coverage out to $\pm$ 3. The mid-rapidity spatial resolution $\Delta\eta$-$\Delta\phi$ of

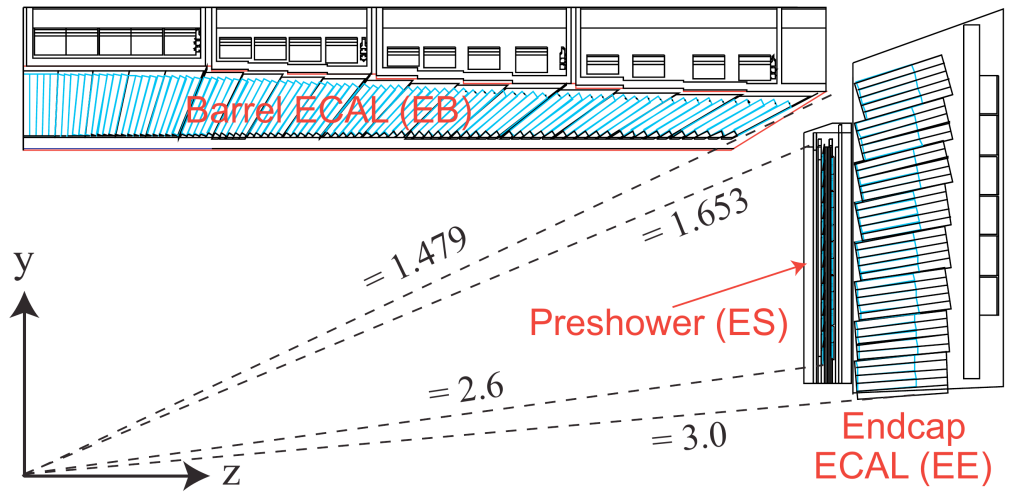

Figure 2-4: Cross section of the CMS electromagnetic calorimeter, subdivided into barrel and endcap components [71].

the HCal is 0.087 x 0.087, giving 72 towers in ϕ. This is the spatial resolution that drives most jet measurements, as towers and pseudo-towers are reduced to this scale. In the HCal endcap, the $\Delta\eta$ width begins to increase modestly, and at η of $\pm$ 1.9 the number of towers in ϕ shrinks from 72 to 36. This granularity continues beyond the HCal into the Hadron Forward calorimetry, until in the final two eta rings the number of towers in ϕ shrinks again to 18.

2.3.3 Hadron Forward

The Hadron Forward, or HF is an essential subdetector in heavy ion jet physics despite no jet measurements as yet existing in heavy ions at this rapidity. This is because the event activity in this subdetector is a reliable proxy for collision impact parameter, and the magnitude of quenching effects scales with increasing nuclear overlap. Fig. 2-5 shows a distribution of transverse energy deposited in the HF for MinimiumBias triggered events taken in 2010 during the very first PbPb runs at the LHC [24].

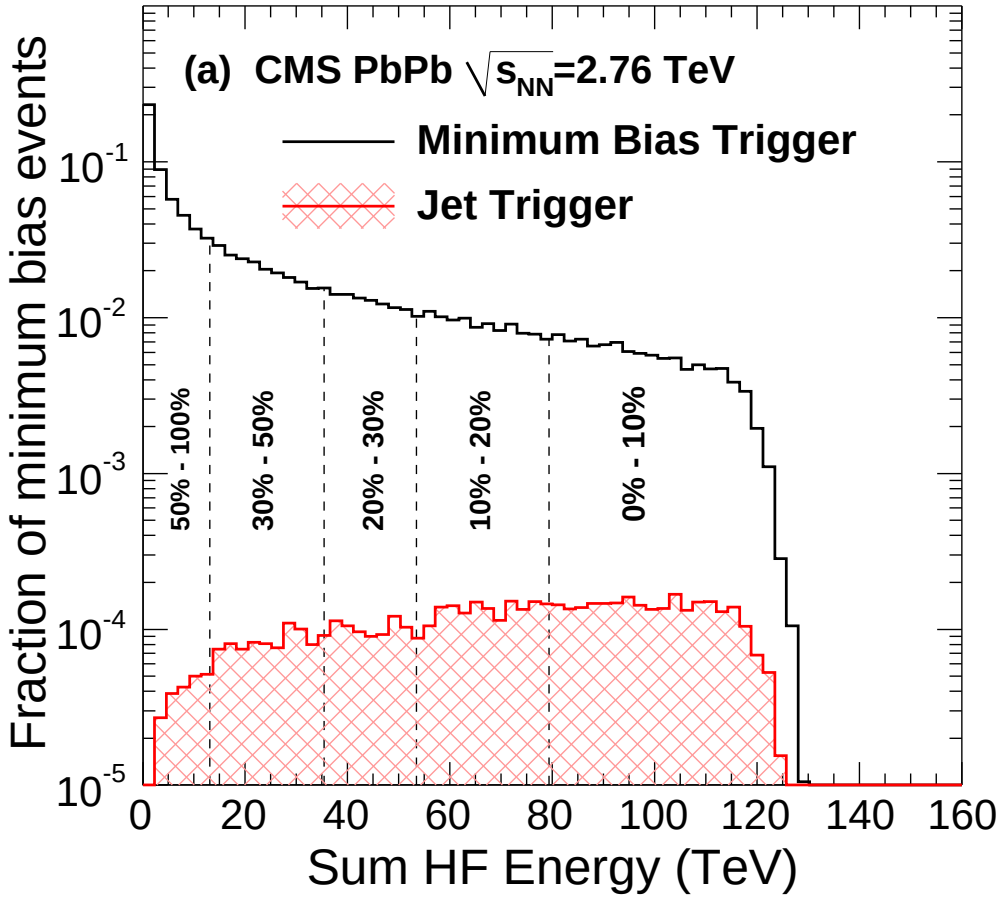

Figure 2-5: Distribution of transverse energy in the HF from MinimumBias triggered events during the 2010 PbPb collisions at $\sqrt{s_{NN}}$=2.76 TeV. This distribution is partitioned into percentiles of centrality as proxy for impact parameter, with the highest deposition of transverse energy corresponding to smallest impact parameter, greatest nuclear overlap, and centrality of 0%. Results will typically be binned in centrality, with medium effects gaining strength as centrality goes to zero [24].

2.4 Muon Chambers

The muon chamber subdetectors are external all calorimetry, and used in combination with tracking for the identification of muons and precise determination of momentum. The destructive calorimetry subdetectors have little impact on muons alone, and act as a shield for particle identification purposes. Muon chambers are essential for Z boson-tagged jet measurements, the current cleanest possible tag of the initial parton transverse momentum. They also contribute in the identification of heavy flavor jets. However, muons constitute a very small fraction of inclusive jet energy as reconstructed with the particle flow algorithm (see Figure 5-8), and are used primarily for fake jet identification in inclusive jet measurements [72]. The muon system is defined by three distinct subdetector systems:

1. Resistive plate chambers covering pseudorapidity $\pm$ 2.1
2. Drift tubes covering pseudorapidity $\pm$ 1.2
3. Cathode strip chambers covering pseudorapidity from 1 to 2.4

Overlapping structure in pseudorapidity gives multiple complimentary measurements for identification.

Chapter 3

Monte Carlo and Simulated Reconstruction

3.1 Overview

A complete understanding of the CMS detector response and induced effects of reconstruction on a given observable requires careful modeling of all subdetector systems with the aid of Monte Carlo. A typical physics objects performance will be first evaluated in Monte Carlo, with data-driven corrections derived and applied atop this initial set of calibrations. This is particularly important in the case of jet reconstruction, an object of many different fragmenting final states spread over a large detector area as compared to photons or charged hadrons. The jets reconstruction requires information from practically ever CMS subdetector, and therefore good simulation.

3.2 Jets in Monte Carlo

A few different generators are used for leading order jet Monte Carlo, the most popular being PYTHIA (both 6 and 8 still in wide use).

3.2.1 Vacuum Jet Monte Carlo

PYTHIA6 and 8 are FORTRAN and C++ implementations of the same basic underlying physics model [73], [74]. PYTHIA calculates leading order diagram, handles initial and final state radiation, multi-parton interactions, and hadronization. In the simulation of hard processes for inclusive jet measurements, the default parton distribution functions are taken from CTEQ, although LHAPDF is easy to incorporate. Hard process production is governed by a starting transverse momentum of the hard-scattering, referred to within the generator as $\hat{p}_{\mathrm{T}}$. For study of of jet production, $\hat{p}_{\mathrm{T}}$ should be chosen such that good statistics are produced for threshold of interest without introducing bias. For example studying jets of p_{T} 15 GeV with a $\hat{p}_{\mathrm{T}}$ 100 GeV sample is highly biased. A typical choice at CMS would be to say study 30 GeV jets starting at $\hat{p}_{\mathrm{T}}$ of 15. Hadronization of final fragments follows Lund string model [75].

PYTHIA6 events are created with TuneZ2 for CMS, and the set of processes used in inclusive jet analysis are set by option HardQCD:all, for a starting hard-scattering transvserse momentum, or $\hat{p}_{\mathrm{T}}$ value of 15 GeV/c (represented by the sample set of diagrams in Figure 1-6).

3.2.2 Medium Jet Monte Carlo

The simulation of jets in medium (i.e. the addition of quenching effects) is as yet not well understood, but there is an available set of Monte Carlo generators that can be used to understand how specific quenching mechanisms might alter jet final states and therefore modify the detectors response. JEWEL is a quenching Monte Carlo that encodes a fully perturbative quenching interaction between the jet and medium, and is particularly of use to the experimentalist as it is built on top of PYTHIA6 [44]. Alternative options include Q-PYTHIA, PYQUEN, the latter being used in the production of PbPb backgrounds as encoded in HYDJET event generator. JEWEL and Q-PYTHIA is never used as part of the analysis chain at CMS. PYQUEN is occasionally used to test different jet fragmentation pattern responses under different quenching scenarios, to test induced average response changes from

medium interactions (while physics causes this, the detector effect is not physics of interest and should be removed).

3.3 PbPb Backgrounds in Monte Carlo

Full CMS detector simulation of PbPb events typically takes a signal Monte Carlo (say PYTHIA8) and embeds that signal in a generated background Monte Carlo. The Monte Carlo typically employed in PbPb jet measurements is HYDJET [76]. HYDJET reproduces a PbPb-like environment in terms of pure particle multiplicity, but additionally incorporates long-range particle correlations and flow (which would not be encoded in simple superposition of minimum bias PYTHIA events). There is additionally quenched minijet production. HYDJET is tuned to match observed particle production in CMS for PbPb, and additional data MC differences are typically accounted for in re-weighting procedures. One example of necessary re-weighting procedure is in the centrality of HYDJET Monte Carlo. HYDJET is typically produced flat in centrality and a single PYTHIA event is embedded in each HYDJET event. In data, however, jet production is heavily biased towards central events, as the total number of colliding nucleons that can produce a hard-scattering is dramatically higher than in peripheral collisions. So flat HYDJET centrality is often re-weighted by number of colliding nucleons per centrality bin, or N_{Coll}.

3.4 Detector Simulation

With a suite of options for jet signal generation and the background modeling by HYDJET, all that remains is the simulation of the produced particle level event's induced signals in an actual detector. This is done with the GEANT4 package [77].

Table 3.1: Summary for PYTHIA6 Monte Carlo samples.

System/Tune	$\hat{p}_{\mathrm{T}}$	Events per $\hat{p}_{\mathrm{T}}$
pp/PYTHIA6	30, 50, 80, 100, 120, 170	500k
pp/PYTHIA6	220, 280	200k
pp/PYTHIA6	370, 460	100k
pp/PYTHIA6	460	100k
pp/PYTHIA6	540	50k

Table 3.2: Summary for Samples for minimum bias Monte Carlo.

System	Generator / Tune	Events
PbPb	HYDJET (DRUM)	477528
PbPb	HYDJET (CYMBAL)	998194
pp	PYTHIA8 (No PU)	4.97M

Table 3.3: Summary for PYTHIA6+HYDJET Monte Carlo samples. All HYDJET is Cymbal tune

System/Tune	$\hat{p}_{\mathrm{T}}$	Events per $\hat{p}_{\mathrm{T}}$
PbPb/PYTHIA6+HYDJET	15, 30, 50	2M
PbPb/PYTHIA6+HYDJET	80, 100, 120, 170, 220, 280	3M
PbPb/PYTHIA6+HYDJET	370	2M
PbPb/PYTHIA6+HYDJET	460, 540	1M

Chapter 4

Triggering

The LHC delivers data in proton-proton collisions at typical bunch intervals of 25 nanoseconds, and PbPb collisions at intervals of 100 nanoseconds. Per bunch crossing pileups in proton-proton range from mean of 1 to 60, meaning that taking all delivered data would realistically mean recording every bunch crossing. While PbPb pileup is sub-percent level, the overall size of each individual event is much greater than proton-proton collisions. Even at low PbPb pileup, in 2018 PbPb data-taking collisions were delivered at a peak rate of 40 kHz. Since at these event sizes we cannot take the full forty thousand events delivered every second, triggering strategies are employed to record the detector only when certain interesting physics conditions are met. Triggering must be quick given the tight time intervals of bunch crossings and must not induce unexpected biases in physics of interest. At CMS, two levels of trigger are employed: a hardware level trigger, known generally as L1 trigger, and a software trigger, known as HLT. For the triggering of jets, the typical strategy is to build up a spectra from a heavily prescaled Minimum Bias triggering scheme, where prescaling discards a fraction of triggers according to a factor defined by physics need. From heavily prescaled minimum bias, a low threshold jet trigger with smaller prescale is added, extending the statistical reach of the constructed spectra. From here higher thresholds of decreasing prescales are added until prescale is off and full integrated luminosity of this subset of events is recorded. Figure 4-1 illustrates this procedure as employed in charged particle R_{AA} [54]. The turn-on curves as shown in the left

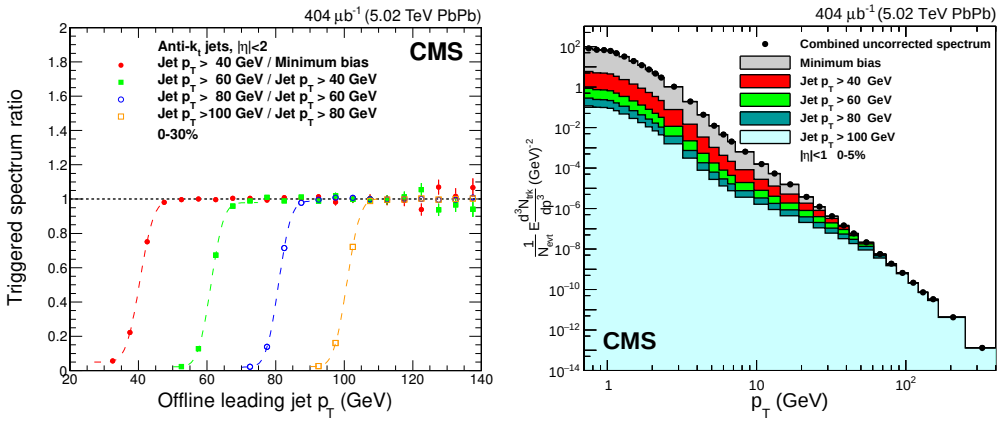

Figure 4-1: Combination of triggered spectra as employed in charged particle R_{AA} measurement. Left: Turn-on curves for jet triggers used in constructing high-p_{T} particle spectra. Right: Corresponding spectra matching procedure and point at which triggered spectra merge (point of 100% trigger efficiency) [54].

of Figure 4-1 are non-zero width error functions because there are limitations in the online reconstruction and offline physics reconstruction that result in differences of energy calculation, position, etc. In the case of charged particle R_{AA} the difference is obvious - jet objects are being used to trigger on hadrons. While at high-p_{T} in PbPb the two are highly correlated the limit of a jet as cone size goes to zero is not hadrons, so there will always be differences in reconstruction. However, even when physics objects are matched online and offline, there are still differences in corrections for response and changes to reconstruction to match timing limitations that can induce turn-on width. As a result the turn-on must always be evaluated in data, and in the case of jets triggered data is typically only used at 100% efficiency (or as close to 100% efficiency such that the full efficiency could be taken as a negligible systematic).

4.1 Hardware Triggering

The L1 trigger effectively has to operate on time scale of 50 nanoseconds (global trigger rules prevent triggering on consecutive bunch crossings, so two 25 nanosecond intervals define the timing limitations). This already excludes time-consuming subdetector systems such as the tracker. So L1 triggering is the domain of calorime-

try (ECal, HCal and HF) and muon chambers. For inclusive jet physics in heavy ions, only calorimetry is required at this level (heavy flavor jet physics may use muon triggering).

For the 2015 data-taking period, timing requirements and available hardware limited the level of calorimeter granularity that could be used in jet triggering. Full details on the Stage-1 L1 trigger hardware can be found in [78]. Here we will only discuss detector object and algorithm defining the two triggers of interest: Minimum Bias and jet triggers.

The Minimum Bias trigger is designed to capture all nuclear interactions (and exclude noise or ultraperipheral electromagnetic interaction). Minimum bias data is used in the validation of all triggered data and in analysis for all objects that cannot be triggered on without inducing insurmountable biases or event rates (say for example, jets of energy comparable to the magnitude of fluctuations in the underlying event). In PbPb collisions at CMS, the Minimum Bias trigger is based on towers in the Hadron Forward calorimeter. All towers in either HF are processed, for 396 per side or a total of 792 towers. One tower is required to record energy above a chosen threshold in both HF directions and in time interval consistent with a valid bunch crossing. The chosen threshold is tuned to maximize the efficiency while mitigating noise to an acceptable rate. In 2015 data-taking the threshold was chosen such that triggering was fully efficient for centrality of 0-90% [54], and 99% efficient in 0-100% range. As this analysis only considers jets out to centrality of 90%, this inefficiency can be safely ignored.

Jet triggering requires the processing of all towers in the HF, ECal, and HCal. Since this analysis is restricted to rapidity $\pm$ 2, only ECal and HCal processing will be discussed. 5-by-5 ECal crystals are combined into single ECal towers matching the HCal geometry in $\eta - \phi$, reducing the ECal-HCal jet detection to the processing of 3456 towers. For clarity, there is an artificial increase in the number of towers that can be imposed such that the number in ϕ is constant at 72, even though at pseudorapidity of $\sim$1.93 the number of towers in ϕ drops to 36. This increases number of towers to process from 3456 to 4032, although the unique information remains the

same.

The set of ECal and HCal towers are further consolidated into regions 4x4 in $\eta-\phi$. This defines fourteen positions in η and eighteen positions in ϕ. In PbPb (and not in pp), each set of regions defined by shared η position is background subtracted, as

$$E_{\text{Bkgd}}(\eta) = \sum_{\phi} E_{\text{Region}}(\eta) \tag{4.1}$$

where E_{Bkgd} is the estimated quantity to subtract and E_{Region} is the energy in each defined 4x4 of towers, summed over the ring in ϕ. Towers that would drop below zero once average is subtracted are set to zero. Furthermore, in PbPb, the 4x4 region encompassing the absolute rapidity 2.172-2.853, or the edge of the endcaps before HF, is zeroed. This is because low momentum particles that do not reach calorimeters known as "loopers" follow helix trajectory down the beam line and pileup in the edge of the endcap. This results in large energy deposition mimicking jet signal at L1 to very high-p_{T} and cannot be disentangled with tracking info due to timing constraints.

With region consolidation (plus additional background subtraction and region zeroing in case of PbPb), jets can be reconstructed. A seed threshold is set and the full event is scanned for regions exceeding seed threshold. Jets are constructed out of jet seeds as follows:

- PbPb:
  - The four possible 2x2 regions containing the seed region are constructed
  - The highest of these four possibilities is reconstructed as jet
  - This set of regions roughly corresponds to a jet of R=0.35
- pp:
  - The full 3x3 set of regions centered on seed is reconstructed as jet
  - This set of regions roughly corresponds to a jet of R=0.5

The four most energetic jets reconstructed in this manner are kept for trigger decision. An event passes jet trigger if it exceeds chosen trigger threshold. For example, L1

jet trigger threshold 56 GeV in raw subtracted response (or 2x2 subtracted region energy sum) was chosen as first unprescaled at L1 in PbPb, which was fully efficient for offline calorimeter jets of 120 GeV. Whether or not an event is kept requires both trigger to fire and not be rejected according to analyzer set prescales.

4.2 Software Triggering

The software level trigger, or HLT, is performed after initial filtering of physics events at L1. Reduced number of input events means additional time is available at this step for deciding whether to trigger or reject. As result more intensive reconstruction can be employed, including some reduced global or full local track reconstruction, more sophisticated calorimeter reconstruction, etc. However, a global track reconstruction as is done in offline reconstruction was still not viable in 2015 (though full track reconstruction was used in 2018 data-taking with only modest modification). Instead, HLT jet triggering employed calorimeter jet reconstruction. The other necessary trigger for jet physics, Minimum Bias trigger, was a pure pass-through of the L1 Minimum Bias decision, but with some additional prescaling.

HLT jets in 2015 is quite similar to L1 triggering insomuch as only calorimeter info is used. However, jets can be reconstructed at the tower level granularity, rather than in combination as 4x4 regions. Furthermore, the subtraction employed is the modestly more sophisticated iterative pedestal subtraction which will be detailed in Section 6.2.2. HLT jet trigger first unprescaled threshold was set at 100 GeV, which is fully efficient for offline reconstructed calorimeter jets by 120 GeV resulting from differences in jet energy corrections. Furthermore, constituent subtracted particle flow jets are fully efficient for this choice of trigger threshold by 160 GeV, as a result of differences arising from particle flow and calorimeter response and subtraction biases between iterative pedestal and constituent subtraction [52, 70]. The effect of the former will be the topic of Chapter 5, while the latter will be topic of Chapter 6.

Chapter 5

Particle Flow Reconstruction

Particle-flow reconstruction seeks to exploit the fully available subdetector information in the reconstruction of individual particles. A technique first commissioned by the ALEPH collaboration at LEP [79], CMS was the first collaboration to use this reconstruction in QCD jet physics, as opposed to pure calorimeter jet reconstruction. Fully commissioned particle flow reconstructions are now available at CMS and ATLAS, although only the former has been as yet used in physics analysis [79], [72], [80]. The primary advantage offered by particle flow is in multiple subdetector measurements compensating in cases where a single subdetector is unsuited to the task. A simple example involves non-linearities of hadronic calorimeter response. A parton that fragments into a few higher momentum hadrons will have a higher calorimeter response than a parton of identical energy that fragments into many softer particles (see Figure 5-19). The incorporation of tracking information, which is superior in measurement of softer particles, will compensate for the calorimeter non-linearities and tighten the width of the overall jet response. The reality of implementation is much more complicated with this, and the advantages over calorimeter jets depends strongly on implementation. However, the general outcome is improved energy resolution, reduced energy scale biases from fragmentation, improved angular resolution, and improved resolution of substructure observables.

Iteration	Name	Seeding	Targeted Tracks
1	InitialStep	pixel triplets	prompt, high p_{T}
2	DetachedTriplet	pixel triplets	from b hadron decays, $R \lesssim 5\,\mathrm{cm}$
3	LowPtTriplet	pixel triplets	prompt, low p_{T}
4	PixelPair	pixel pairs	recover high p_{T}
5	MixedTriplet	pixel+strip triplets	displaced, $R \lesssim 7\,\mathrm{cm}$
6	PixelLess	strip triplets/pairs	very displaced, $R \lesssim 25\,\mathrm{cm}$
7	TobTec	strip triplets/pairs	very displaced, $R \lesssim 60\,\mathrm{cm}$
8	JetCoreRegional	pixel+strip pairs	inside high p_{T} jets
9	MuonSeededInOut	muon-tagged tracks	muons
10	MuonSeededOutIn	muon detectors	muons

Figure 5-1: Iterations employed in tracking reconstruction as input for particle flow in pp. Specific purpose of each iteration is specified. Table taken directly from [72].

5.1 Tracking for Particle Flow

Tracking in CMS is performed iteratively to maximize efficiency while minimizing the reconstruction of fake tracks. While this method achieves 90% efficiency over a broad range of transverse momentum in proton-proton collisions as seen in Figure 5-2, and 70% efficiency in central PbPb collisions, the exact method of track reconstruction is not necessarily important to the successful implementation of particle flow reconstruction. In part this is clear in its implementation at both ALEPH, which employed a Time Projection Chamber for tracking and at CMS, with silicon pixel and strip tracking detector. The reconstruction methods are very different, but both were able to employ particle flow reconstruction once a final collection of tracks was produced and used as input to algorithm along with calorimeter information. Insomuch as details are needed in reconstruction, it is in applying additional cleanings to tracks that are not necessarily compatible with associated calorimeter energies.

The following is a brief description of CMS tracking reconstruction, in order to make clear later cleanings applied in particle flow. After each iteration, hits employed in previous iterations that are definitively part of reconstructed tracks are removed as the have been unambiguously associated with a reconstructed track. The cleaning of these assigned hits, and loosening of criteria as hit density falls, is where most of the recovered efficiency of the iterative technique comes from.

1. Primary vertex is reconstructed from a fit of pixel track trajectories as extrap-

olated to beamspot. Vertex is assigned position in x,y, and z with associated errors.

2. Tracks seeded by three hits in pixel barrel or endcap detectors with trajectory consistent with primary vertex to within 2mm are reconstructed.

    - Tracks failing χ^2 goodness of trajectory fit or primary vertex compatibility are rejected
    - Tracks passing are reconstructed out through the strip detectors

3. Similar iteration seeded by pixel triplet with looser requirements after first set of hits is cleaned.

4. Similar iteration seeded by pixel pairs with looser requirements after first and second set of hits is cleaned.

5. Iteration for recovery of high-p_{T} tracks in jet cores is run

Note that tracks reconstructed at each iteration can share hits, as only those hits that pass an additionally stringent compatibility are cleaned. Tracks sharing many hits are checked if duplicate, and if so are merged. Tracks reconstructed at all iterations, after duplicate removal, are eventually combined into a single collection.

Note that the collection of tracks as directly reconstructed above undergo additional, high purity selection, with specific efficiency and fake rate targets. While the final cuts are determined by multi-variate analysis, or MVA tools as encoded in TMVA ROOT package [81], the set of inputs can be relevant to later cleanings. The information used as input in high purity derivation in PbPb are

- Trajectory χ^2 / ((Number of Layers with Hit) $\times$ (Number of Degrees of Freedom))
- Number of Hits
- Number of Layers with Hits
- Pseudorapidity (Relevant for detector material budget and geometry)

- Delta of x-y position of origin with vertex / Error on x-y position of origin
- Delta of z position of origin with vertex / Error on z position of origin
- In some cases, relative error on transverse momentum

Table 5.1: Iterations employed in tracking reconstruction as input for particle flow in PbPb. Reduced number of iterations is primarily to reduce computational resources necessary, at cost of efficiency. Adapted from [54] to mirror pp Table 5-1.

Iteration	Name	Seeding	Target Tracks
1	Initial Step	Pixel track	High p_{T} prompt
2	Detached Step	Pixel triplets	Displaced prompt
3	Low p_{T} Step	Pixel triplets	Low p_{T} prompt
4	Pixel Pair Step	Pixel pairs	Recover High p_{T} prompt
5	Jet core Step	Pixel triplets	Tracks with high local density

As example of where the tracking details become important, Figure 5-1 is a table taken directly from particle flow paper detailing which iteration is intended for which reconstruction purpose. In particle flow, when the combined set of tracks associated to an HCal cluster or incompatible within the errors of the two detector measurements, then tracks are removed iteratively according to quality cuts, with most extreme case requiring full removal of all tracks from iterations 4 and 5. This is because these are the iterations with highest likelihood to introduce fake tracks. In particular, the high-p_{T} track recovery iteration 4 is likely to have introduced fakes if there is no compatible energetic calorimeter energy cluster, given that in high momentum the calorimeter response is effectively flat (see Figure 5-19).

5.2 Particle Flow Constituents

Particle flow combines all subdetector information into a single set of effectively particle level constituents without double counting signals through a subdetector linking procedure. The inputs to the algorithm are reconstructed objects from each subdetector system. These are: tracks, ECal energy clusters, HCal towers, and muon chamber hits (although this information is typically incorporated into the tracking information

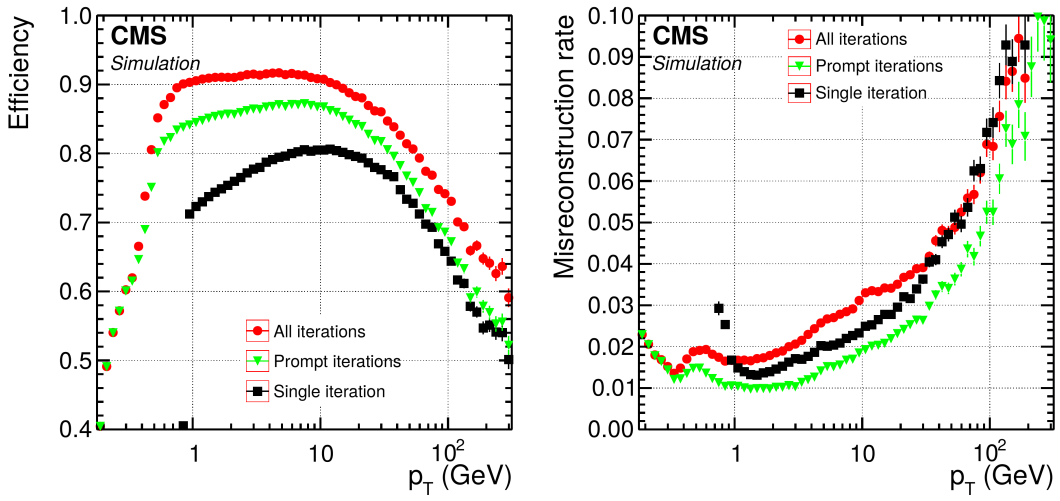

Figure 5-2: Performance of the iterative tracking reconstruction as employed at CMS in proton-proton collisions. [72].

as muon particle identification). This set of subdetector inputs constitute a potential set of particle flow elements to each particle flow candidate. To go from element set to candidates, elements are linked according to a set of geometric matching criteria, and then iteratively combined according to kinematic compatability.

5.2.1 Technical Description of Particle Flow at CMS

The following is based on 2015 reconstruction based in CMS software release CMSSW_7_5_8_patch3.

Subdetector objects are combined into sets of topologically connected elements called PFBlock. A PFBlock is defined by its elements and the links between those elements. The link is defined by the pair of elements it connects (nodes) and the distance between nodes (here a simple $\Delta\eta$-$\Delta\phi$ calculation). The distance parameter defining links will later be used in decisions about which linked elements ought be combined as single particle. Figure 5-3 shows a toy representation of a simple PFBlock likely representing a charged pion. There are three elements connected by two links, each of a calorimeter cluster with a track. If the links are not superseded by a more compatible track matching, these three subdetector objects will be combined into a

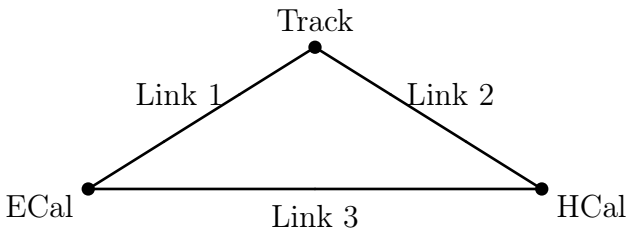

Figure 5-3: Diagramatic representation of a PFBlock of linked subdetector objects that are the initial input to particle flow algorithm. In this case, we have a link of an ECal cluster to a track by Link 1, a link of an HCal cluster to the same track by Link 2, and a linking of ECal and HCal cluster by Link 3. In this case, the PFBlock likely represents a charged pion.

single object.

PFBlocks once constructed are sorted into four collections: a collection of single element ECal clusters, a collection of single element HCal clusters from the Hadron Outer Calorimeter, a collection of all other single element HCal cluster, and a collection of remaining PFBlocks. The collection of single element Hadron Outer Calorimeter PFBlocks is discarded, as these are very likely noise. With the three remaining collections, the algorithm for determining which linked elements are most compatible proceeds in several iterations. The first iteration is for fully composite PFBlocks, typically tracks with one or both of an ECal or HCal cluster. The second iteration is PFBlocks of pure HCal clusters, and aims at recovering track matches. The third iteration is a mirror of the second iteration but for ECal clusters. Table 5.2 summarizes this first sorting.

Table 5.2: Iterations processing PFBlocks into identified particles. This processing prevents the double counting of energy in the final set of constituents.

PFBlock Collection	Iteration
Single Element from Hadron Outer Calorimeter	Discarded
Single Element from ECal	3rd Iteration
Single Element from HCal, Not HO	2nd Iteration
All Other PFBlocks	1st Iteration

First iteration takes as input the collection of composite or single-track element PFBlocks. Details regarding the treatment of muons and electrons will be skipped here for clarity, as they comprise a very small fraction of the typical jet energy com-

pared to charged hadrons, neutral hadrons, and photons. The processing of a collection of PFBlocks can be broken into a few loops. In the first loop,

1. All linked ECal clusters are identified and sorted in a unique vector.

2. All linked HCal clusters are identified and sorted in a unique vector.

3. PFBlocks coming purely from the Hadron Forward calorimeter are identified.

4. Tracks that are not linked with an HCal or ECal cluster are identified.

5. Tracks linked to multiple HCal clusters are reduced to a link with the single closest cluster.

The identification and sorting of calorimeter info is a trivial component of this first loop, while the processing of each track element of a PFBlock is more involved. As first step, primary tracks, or the inbound tracks that initiate nuclear interactions with detector material resulting in a set of secondary particles, are identified by trajectory consistent with primary vertex and vertex of nuclear interaction. These are immediately made into a pure track particle flow candidate. This is because it by definition cannot be associated with calorimeter clusters (it is the secondaries that are associated with calorimeter clusters). Secondaries particles are treated as any other particle from primary interactions would be during particle flow algorithm, just from its nuclear interaction vertex. At the end of particle flow reconstruction, the set of particles from each nuclear interaction vertex is combined into a single candidate representing best measurement of primary track. There are three cases for this recombination:

1. In the case where no primary track is measured, the composite is a pure four vector sum of all secondaries

2. In the case where primary is measured but energy resolution is poor, the trajectory is taken from primary particle measurement but energy is taken from four momentum secondary sum

3. Finally, in case where primary is measured and error on energy measurement is sufficiently small, trajectory is taken from primary and it is incorporated in energy calculation as

$$E = E_{sec} + f(\eta, p_{prim})p_{prim} \tag{5.1}$$

where f is the fraction of the primary particle momentum not reconstructed on average from secondaries, as a function of primary η and momentum. This is determined in Monte Carlo [72].

If a track is not primary, and also not already used in reconstruction of an electron, or muon, then the full set of associated calorimeter elements is processed. ECal and HCal clusters are stored in vectors sorted by link distance from track. Nearest linked HCal cluster is checked if the tower was flagged as dead during data-taking. If tower is flagged as dead, the tower is unlinked and the track is subject to a set of more stringent quality cuts to reduce fakes linked to bad towers. The set of cuts are on

1. Relative p_{T} error
2. Trajectory normalized χ^2
3. Number of track layers with measurement
4. Error on x-y position of associated primary vertex
5. Valid Fraction of hits

Note that an additional set of more stringent cuts is applied to pixel tracks at η beyond the typical full track acceptance of pseudorapidity $\pm$ 2.4, while also adding a cut on longitudinal vertex position error and a cap on track momentum.

After handling tracks linked to dead HCal towers, a recovery step is implemented for tracks associated with no HCal tower (but excluding the previously handled dead tower tracks now unlinked). This recovery step takes the set of tracks with no HCal link but with an ECal link. Then, per ECal link, loop over all other tracks also linked to same ECal cluster. If these jointly linked tracks also happen to be linked to HCal

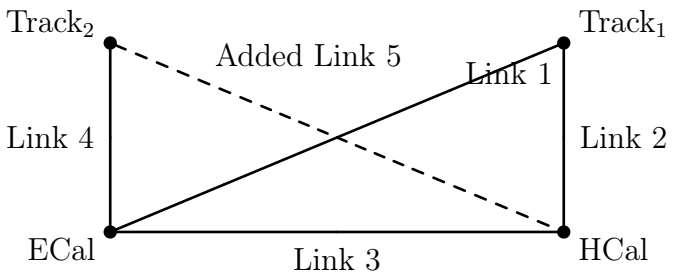

Figure 5-4: Diagramatic representation of a more complicated PFBlock of linked subdetector objects. In this case, we have the same initial structure as Figure 5-3 but an additionally linked track to the same ECal cluster. After an initial step of processing, the algorithm recognizes that two tracks share an ECal cluster link but one track is missing the HCal cluster, so a link is added for later analysis (dashed link line).

towers, link the original track with HCal tower. A representation of PFBlock that has undergone recovery procedure for HCal links is shown in Figure 5-4.

After recovery step, process all tracks that lack a linked HCal tower. The lack of linked HCal requires additional fake rejection. Additional fake rejection is applied to all tracks that are not associated with a muon, are not primary tracks associated with nuclear interaction, and were not previously associated with dead HCal tower. If a track's p_{T} error exceeds a chosen threshold, and its momentum minus the energy of the closest linked ECal cluster exceeds Nσ of the HCal resolution for the tracks momentum and pseudorapidity, then the track is rejected as fake and no particle-flow candidate is created.

Additional cleaning is applied to secondary tracks produced from nuclear interactions after this step, as a particle produced from secondary interaction without associated HCal tower is almost certainly fake. These high-p_{T} secondaries without linked HCal tower are removed, and then a particle flow candidate is created from the remaining set of tracks.

Processing tracks with no associated HCal, if it also has no associated ECal clusters, then the algorithm terminates for this element, after setting candidate ECal and HCal energies to zero. This set of candidates represent the primary recovered soft component of the jet energy in particle flow algorithm.

In the event that there are associated ECal clusters, the closest ECal cluster is

taken as start point for combination. All tracks also associated with this ECal cluster are processed, with fake tracks, already used tracks, and tracks with another ECal cluster as closest cluster rejected. The remaining set of tracks form the set over which this ECal energy will be partitioned to prevent double counting. With the set of tracks identified, we proceed to process all associated ECal elements of the initial track ordered by increasing link distance (i.e. those that were not identified as closest but are still linked). If an ECal element is already taken by a previous candidate or if it is closest to another track not in the set of tracks closest to the primary ECal cluster, then it is rejected.

If it passes this criteria, but the addition of its energy to the track/ECal cluster is in excess of hadron hypothesis as determined by total ECal energy time Nσ of response width and total track momentum, then loop is terminated (remaining clusters will become photons). The fraction of associated ECal cluster energy in excess of hadron hypothesis becomes a single photon candidate. The remaining ECal cluster energy is partitioned among the set of associated tracks to prevent double counting. Every ECal and track element of PFBlocks now collapsed into PFCandidates is set to inactive to prevent double counting.

Track elements that have multiple associated HCal elements are then reduced to a single associated HCal element. This is done simply by unlinking all associated towers except that which is closest linked. However, HCal elements can still be multiply linked to tracks. The HCal tower energy is then iteratively partitioned among all associated tracks. There are several partition cases.

1. Associated single track is well-identified isolated muon

    - If energy exceeds HCal PFBlock element, muon candidate absorbs HCal energy completely.
    - If not in excess, remainder to neutral hadron.

2. Total charged momentum (one non-muon or many tracks) exceeds calorimeter by N$\sigma\times$Calorimeter Resolution

- Remove energy from loose non-isolated muons
- Apply additional rejection on tracks
- Apply rejection to all tracks from specific iterations

3. Total charged momentum (one non-muon or many tracks) is fully compatible with calorimeter by N$\sigma\times$Calorimeter Resolution
    - Associated tracks are collapsed with HCal tower to form charged particle flow candidates.
    - Each track comprises unique candidate, but final four momentum is assigned according to weighted average of track set and calorimeter energy to minimize final error.
4. Total charged momentum (one non-muon or many tracks) is below compatibility threshold with calorimeter by N$\sigma\times$Calorimeter Resolution
    - In this case, proceed as previous case but remaining HCal energy is turned into a neutral hadron particle flow object.

Having worked through all PFBlocks of tracks, the only remaining PFBlocks are those comprised of ECal and HCal clusters lacking links to tracks. These are turned into photon and neutral hadron candidates respectively. Since the calorimeter is destructive, double counting energy is less of a concern here, and most associations of clusters with neutral hadrons, charged hadrons that left no reconstructable tracks, and photons are hypothesized to maximize the modeling precision of the detector response. Particle flow objects in the Hadron Forward calorimeter where there is no tracker coverage are similarly handled, where short and long fibers for channeling light allow for limited photon identification (a photon will deposit almost all its energy in short fibers that terminate early in the calorimeter, whereas neutral hadrons will have significant energy fraction in long fibers).

Note that this the description of the particle flow algorithm above is only a snapshot of reconstruction during one point over the lifetime of the CMS detector, coinciding with the 2015 PbPb data-taking period. While the basic implementation ideas

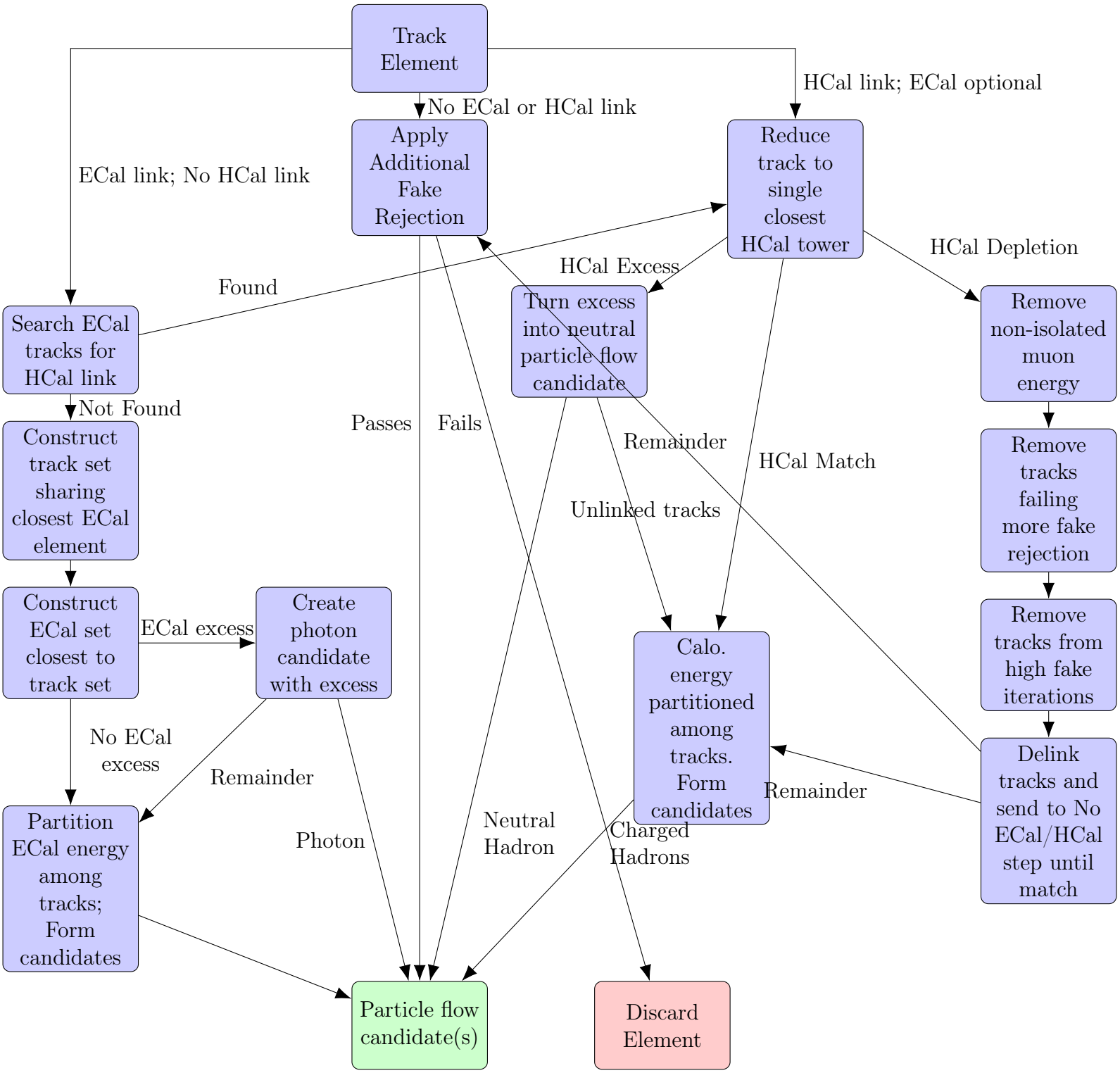

Figure 5-5: A simplified flow chart for particle flow processing for track elements. This is the essential structure of the CMS particle flow implementation for the prevention of double counting particles when combining subdetectors that are non-destructive with destructive calorimetry.

(association of elements, iterative linking, reduction to single particles minimizing double counting error) order of association, criteria for matching, etc. are choices that are made with specific performance targets in mind. As a result, while the above could be adapted as an implementation, specifics must be set with physics in mind.

5.2.2 Examples of Particle Flow Reconstruction

Two examples are provided as follows:

- A muon from Z boson decay

    1. A track's trajectory is extrapolated through the ECal and HCal from its last known hit in the silicon strips
    2. No ECal or HCal clusters are reconstructed within the extrapolated trajectory and associated errors
    3. The extrapolated trajectory is consistent with hits in the muon chambers
    4. The track and muon chambers are linked, linked elements are combined into single candidate of kinematics according to an error weighted combination of elements (in this case likely dominated by track measurements).

- A single high-p_{T} charged pion from a hard-scattered parton

    1. As with the muon, a track's trajectory is extrapolated through the ECal and HCal from its last known hit in the silicon strips
    2. No ECal clusters are reconstructed within the extrapolated trajectory and associated errors
    3. A single HCal cluster is reconstructed within the extrapolated trajectory and its associated errors
    4. The HCal cluster is linked to track, the linked elements are removed and a candidate is created with kinematics defined by error-weighted combination of HCal and tracker measurements

– Depending on how high-p_{T} the charged pion, the calorimeter resolution contribution to kinematics increases, as relative calorimeter resolution scales as $1/\sqrt{E}$ while track resolution scales as p_{T}.

This linking procedure is continued until all collections are exhausted. There are five different associated identities for particle flow candidates within pseudorapidity $\pm$ 3 (with an additional two for Hadron Forward candidates, but not used here). They are

1. Charged hadrons: tracks, with potential links to ECal and HCal energy deposition, with ECal not representing full energy.

2. Muons: tracks linked to hits in muon chambers

3. Electrons: tracks linked to ECal energy depositions, ECal consistent with full track energy.

4. Photons: ECal energy depositions with no viable track links

5. Neutral hadrons: HCal energy depositions with no viable track links

This set of candidate identities is illustrated in Figure 5-6.

Note that of this set of candidates, there is opportunity for mis-identification. For example, a muon can leave a track but fail linking criteria to muon chamber hits. While this would induce a reconstruction-based inefficiency in say, measurements of Z bosons decaying leptonically, it is actually of reduced impact in case of jets as the candidate is retained as a mis-identified charged hadron. Likewise, a scenario where a charged hadron's associated track is rejected as fake would be retained as part of the neutral hadrons with its HCal deposition. The impact of this type of mis-identification is greater than in the muon case, as can be seen from considering the limit in which all tracks are rejected: performance would converge on that of calorimeter jets. Figure 5-7 shows the improvements as implemented in standard proton-proton collisions. Deterioration in track reconstruction would serve to move

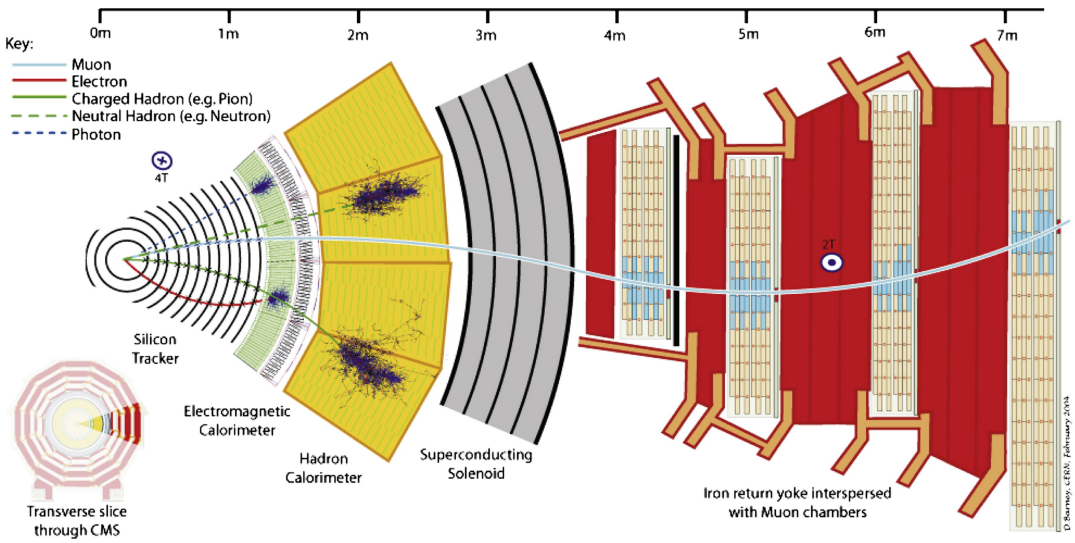

Figure 5-6: Progression of several particle types through a view of the CMS detector down the beamline, highlighting the different possibilities for particle flow processing. Photon trajectory is straight and leaves no tracker hits, depositing all energy in ECal. ECal deposition matched to track trajectory is identified as electron. Track matched to ECal and HCal deposition corresponds to charged pion, while HCal deposition without track match corresponds to neutral hadron (here neutron). Finally, track without significant ECal or HCal associated depositions matched to hits in muon chambers is reconstructed as muon [72].

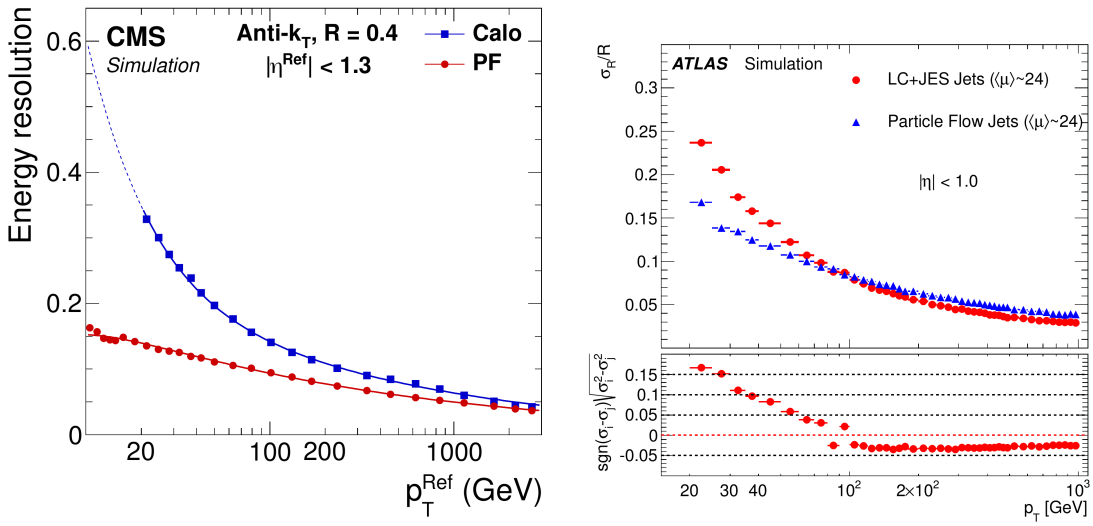

Figure 5-7: A comparison of jet energy resolution for particle flow and calorimeter jets as reconstructed with full CMS and full ATLAS simulation. The strong improvement in energy resolution can largely be attributed to the incorporation of tracking information. Note that in ATLAS implementation there is actually degradation of performance at high-p_{T}. [72, 80]

the particle flow resolution curve to some intermediary position towards the calorimeter jet resolution curve. Similar results can be observed in the corresponding plot as produced with ATLAS implementation of particle flow, with only difference being at highest jet p_{T} where calorimeter jets outperform particle flow (although it is unclear whether this is a limitation of detector or implementation).

5.3 Particle Flow Jets

5.3.1 Toy Performance

To illustrate the gains to be had from the incorporation of tracking information into the reconstruction of jets, consider the following toy:

1. Jets are generated using PYTHIA8 pp collisions at $\sqrt{s_{NN}}$=5.02 TeV

2. Truth jets are reconstructed using all final state, non-neutrino particles

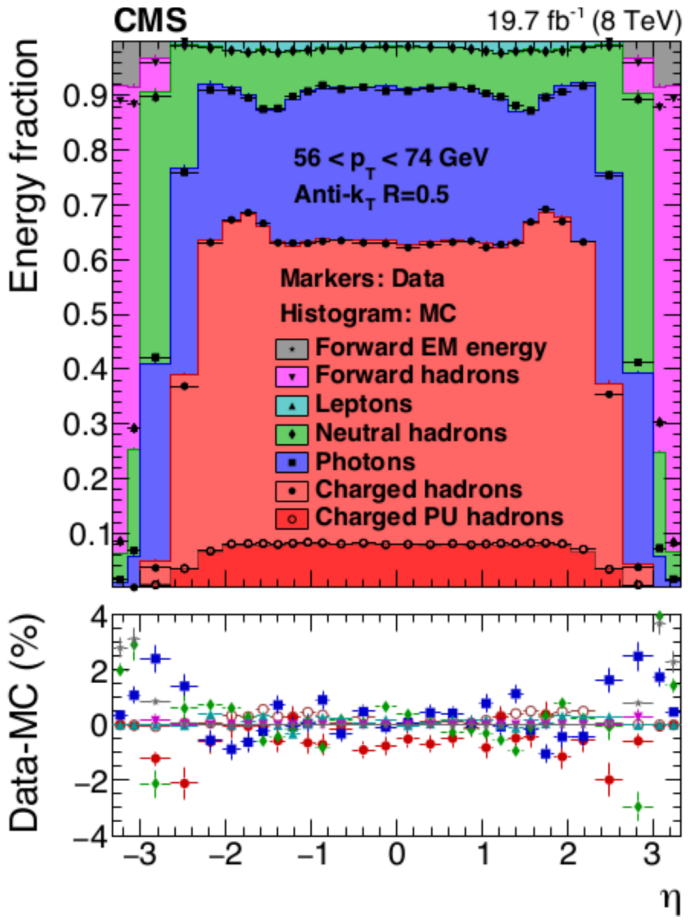

Figure 5-8: A breakdown of average jet energy as it is sourced to various subdetectors. Roughly 60% comes from charged particles reconstructed with the tracker, another 30% is neutral electromagnetic objects as reconstructed in the ECal, and the remaining 10% comes from neutral hadrons detected with the HCal. The remaining contributions are relatively negligible, and are identified as muons (tracks with linked hits in the muon chambers) and electrons (tracks associated with an energy cluster from the ECal) [72].

3. A calorimeter η-ϕ grid is constructed using the CMS HCal $\Delta\eta$ x $\Delta\phi$ geometry of 0.087 x 0.087 out to $\pm$ forty times this width, or η=3.48. Geometry will be shared by ECal and HCal for simplicity.

4. ECal resolution is imposed on particles with pdgid 22, or photon. Resolution is taken from CMS particle flow paper and is parametrized

$$\frac{\sigma}{E} = \frac{.028}{\sqrt{E}} \bigoplus \frac{.12}{E} \bigoplus 0.003. \tag{5.2}$$

5. HCal resolution is imposed on non-photon neutral particles, or charged particles randomly assigned as not reconstructed according to choice of inefficiency. Resolution is taken from CMS particle flow paper and is parametrized

$$\frac{\sigma}{E} = \frac{1.1}{\sqrt{E}} \bigoplus 0.09. \tag{5.3}$$

6. Non-linearity of calorimeter response is imposed with an error function of form

$$\text{Response} = 0.5(1 + \text{erf}\,[0] \times (E - [1])) \tag{5.4}$$

   where [0] and [1] are parameters chosen to minimize or exagerate non-linearities while turning off response completely roughly at E = 0.7. We've substituted E for p_{T} to keep things simple if wrong.

The toy and the set of parameters chosen are meant to reflect known behavior of subdetector systems that dominate the reconstruction effect in a simplified manner. While illustrative, it is not a full validation of any algorithmic implementation (for validation at CMS see Section 5.3.2).

Figure 5-12 shows the impact on the reconstruction performance for a few bins of truth jet transverse momentum of particle flow toy implementations defined by choices of tracking efficiency, as compared to pure calorimeter reconstruction. No calorimeter resolution is introduced yet, and the only change between different points is combination of particles into towers, and imposition of sharp error function at

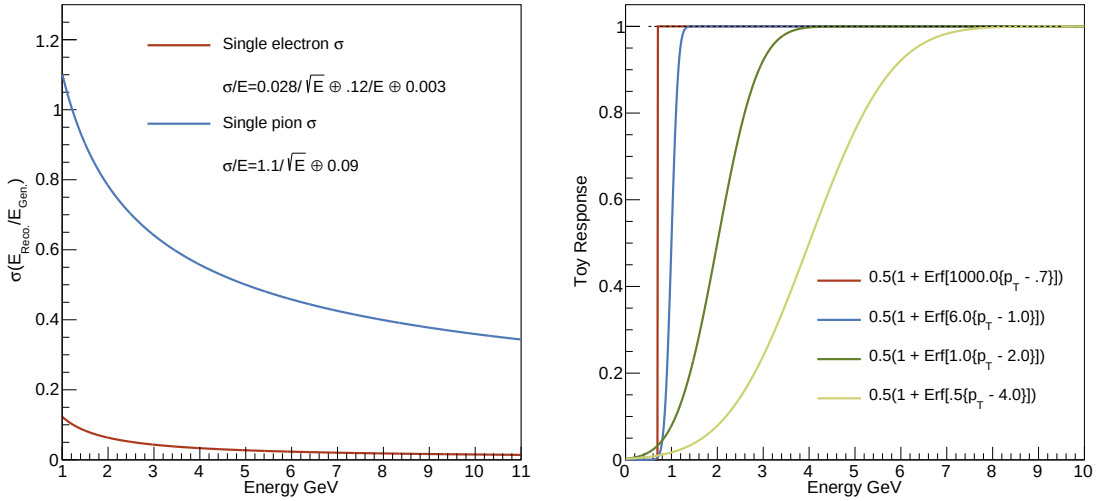

Figure 5-9: Left: Response of CMS ECal and HCal with respect to single photon/pion, respectively. These curves are used in toy simulation of particle flow. HCal is a clear limit on reconstruction performance. Right: Imposed response non-linearity scenarios. While these are generally unrealistic, the illustrate specific impact of magnetic field, nuclear interaction, response degradation with radiation damage, etc.

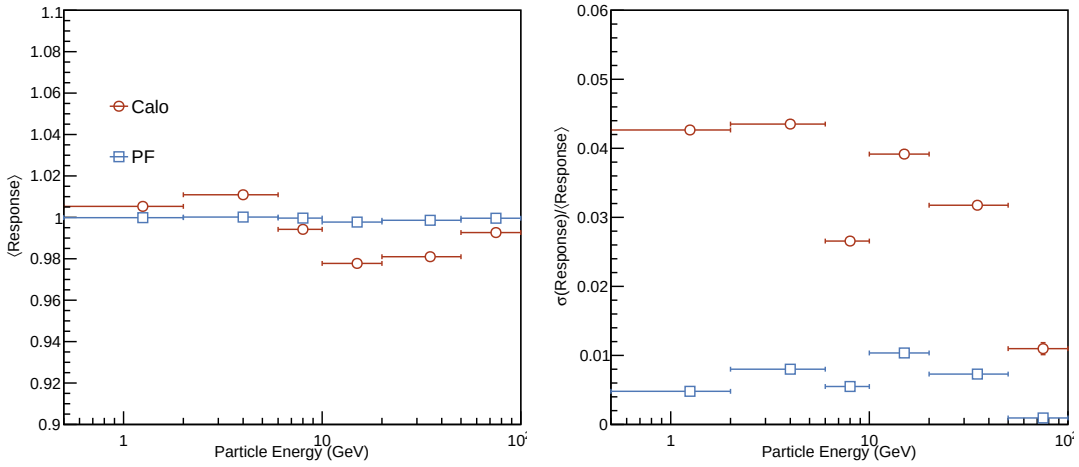

Figure 5-10: Comparison of particle flow and calorimeter jet response after adding correction for calorimeter response with hypothesis that each tower corresponds to one tower. The calorimeter non-closures are result of towers with energy deposition from multiple particles. The number of particles per tower within jets can be seen in Figure 5-11.

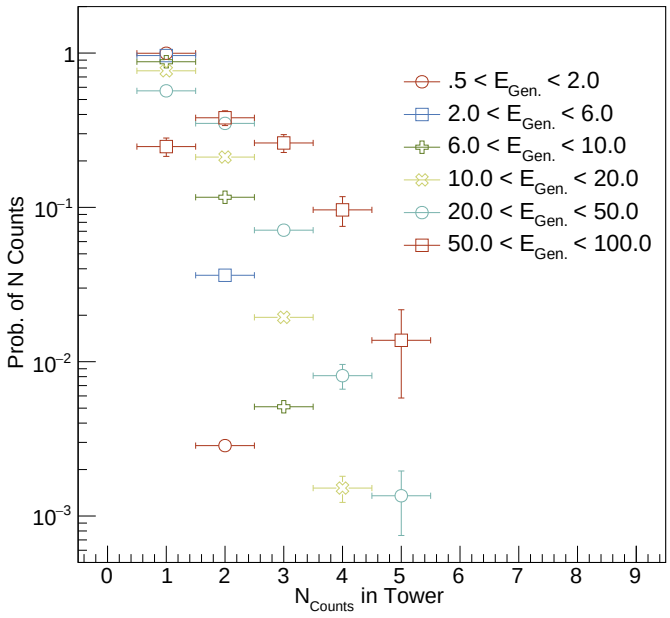

Figure 5-11: Number of particles per calorimeter tower in a jet at zero pileup, in bins of tower energy. While the general most probable number of particles per tower is one, there is significant towers with more than one particle. Here the correction under single particle hypothesis is explicitly wrong.

0.7 GeV to simulate the magnetic field on low momentum particles. The changes in performance is quite subtle in this case, although Figure 5-13 shows that already there is a 25% resolution difference between pure calorimeter jets and particle flow jets, representing the recovery of particles below the 0.7 GeV cutoff.

In Figure 5-14, the toy still lacks the introduction of calorimeter resolution, but the error function is substantially broadened to introduce a more realistic calorimeter non-linearity in response. This is partially capturing the additional 25 centimeter getting from start of ECal to start of HCal, nuclear interactions in material budget of detector pre-calorimeter, and natural non-linearities in HCal itself. One can see that the performance degradation of calorimeter jets compared to toy particle flow is enhanced. In addition to the resolution degradation, it should now be clear that there is a significant difference in response for different jet flavors, as shown in Fig. 5-15. This is because the non-linearity impacts the softer fragmenting gluon jets more than the harder fragmenting quark jets. Particle flow serves to collapse the widening difference between the two jets populations, which is invaluable in measurements with significant jet flavor uncertainty.

Finally, we introduced the calorimeter resolution on top of the previous toys enhanced non-linearity. This is the most dramatic degradation of performance, as HCal resolution on top of non-linearity introduces significant fragmentation dependent scale bias and on overall increase in Gaussian width. Figure 5-16 summarizes this conclusion. Note that in these studies we did not consider the complications of fake tracks, double counting energy, and other issues of algorithm implementation. This is an incredibly tricky subject, as evidenced by the high-p_{T} performance of the ATLAS particle flow implementation. However, it is also a detail irrelevant to understanding the general potential gains to jet resolution and response offered with particle flow.

5.3.2 Jets in pp

The toy in the previous section serves to explain why significant performance gains are reasonable to expect, but are insufficient for a full validation. Potential double counting of energy when combining non-destructive subdetector information must be

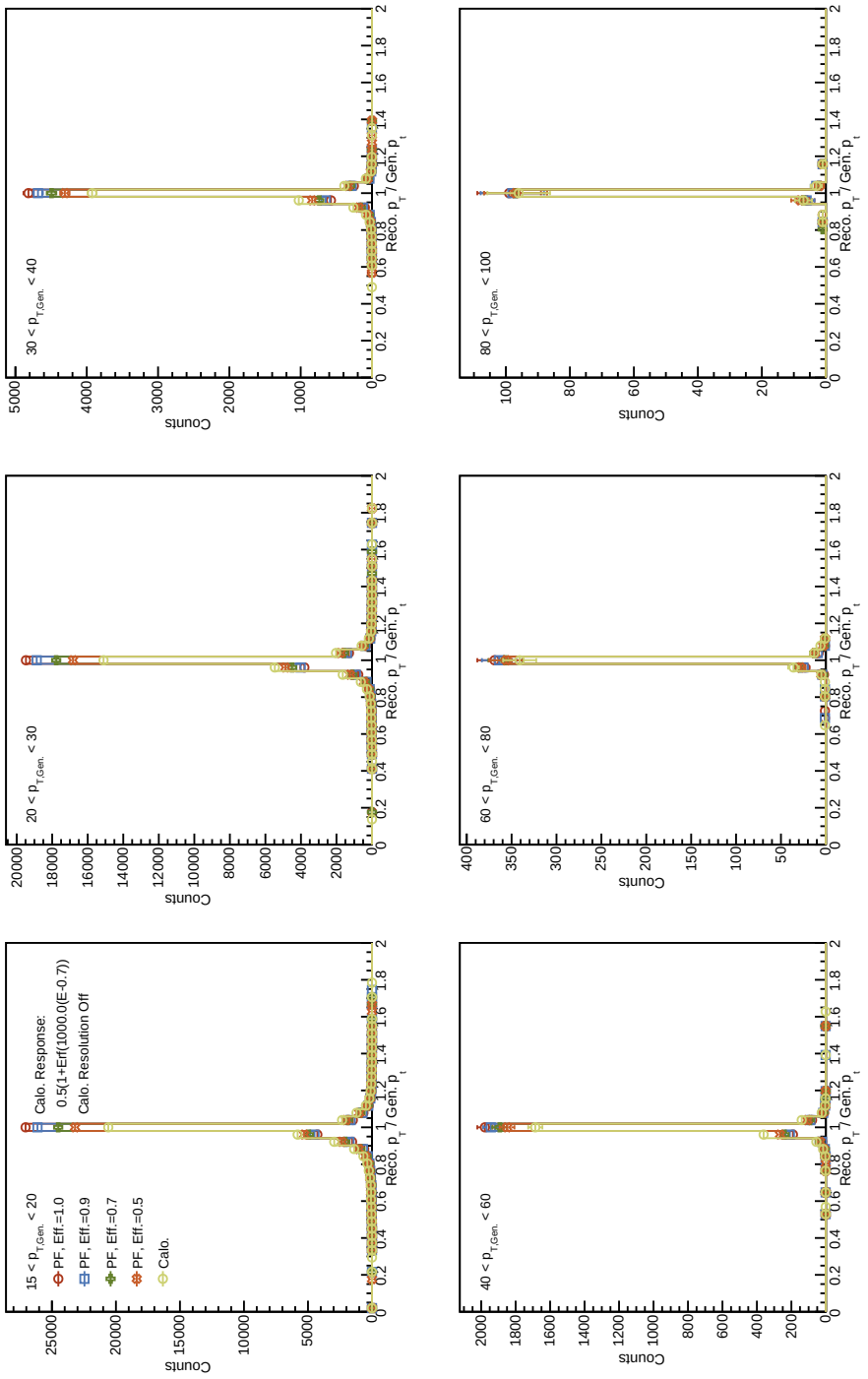

Figure 5-12: Jet energy response comparing toy particle flow implementation for a few different imposed tracking efficiencies to calorimeter jets. There is no added energy resolution in the calorimeters, and non-linearity is imposed using an error function that effectively turns off exactly at 700 MeV, the magnetic field cutoff for charged particles. From left to right, top to bottom in panels, the response is binned as a function of particle level jet transverse momentum, from $15 < p_{\mathrm{T}} < 100$. Even with this single degradation to the performance of the calorimeter, all particle flow implementations offer improvements to performance over pure calorimeter, especially at low-p_{T}.

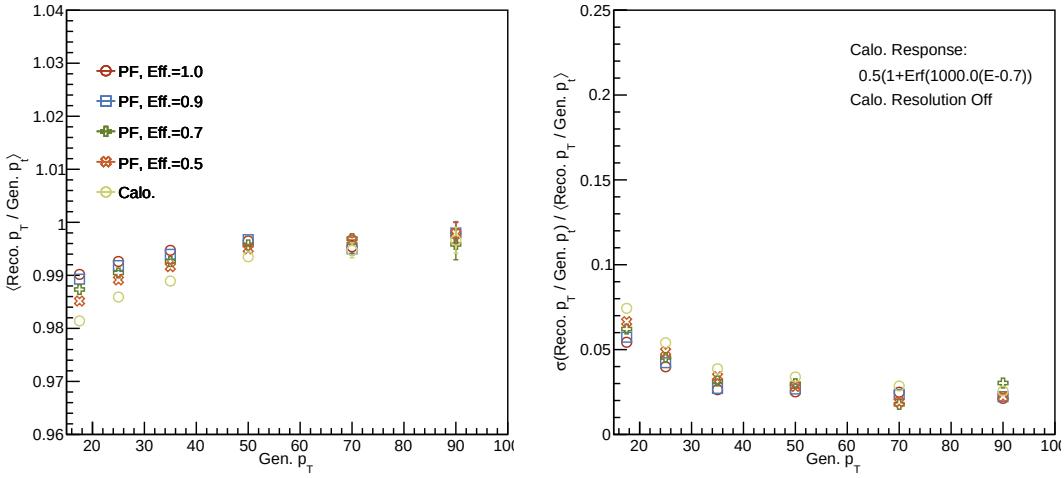

Figure 5-13: Mean and width of response plots as shown in Figure 5-12, comparing toy implementation of particle flow to calorimeter reconstruction for a few imposed tracking efficiencies and minimally degraded calorimeter performance. While the gains are modest, its clear that there is about a 20% improvement in resolution at low jet p_{T} when switching from calorimeter to particle flow jets.

handled carefully, and only an algorithm commissioned in fully simulated reconstruction with Monte Carlo can be a trusted representation of performance. Figures 5-19 through 5-22 show that the behaviors we sought to replicate in the toy example are also found in the fully simulated particle flow reconstruction at CMS [72]. The specifcs of the algorithm used to combine particle flow candidates into jets is described in detail in Chapter 6.

5.3.3 Jets in Heavy Ions

The following set of requirements is considered essential for the successful implementation of particle flow reconstruction

1. Maximized tracking efficiency down to the very lowest particle momentum

    - Every loss of tracking efficiency from 100% reverts particle flow performance gains to that of calorimeter jets
    - The non-linearities of the calorimeter are worst at lowest p_{T}, with 0.7 GeV tracks never even reaching ECal in the 4 Tesla field

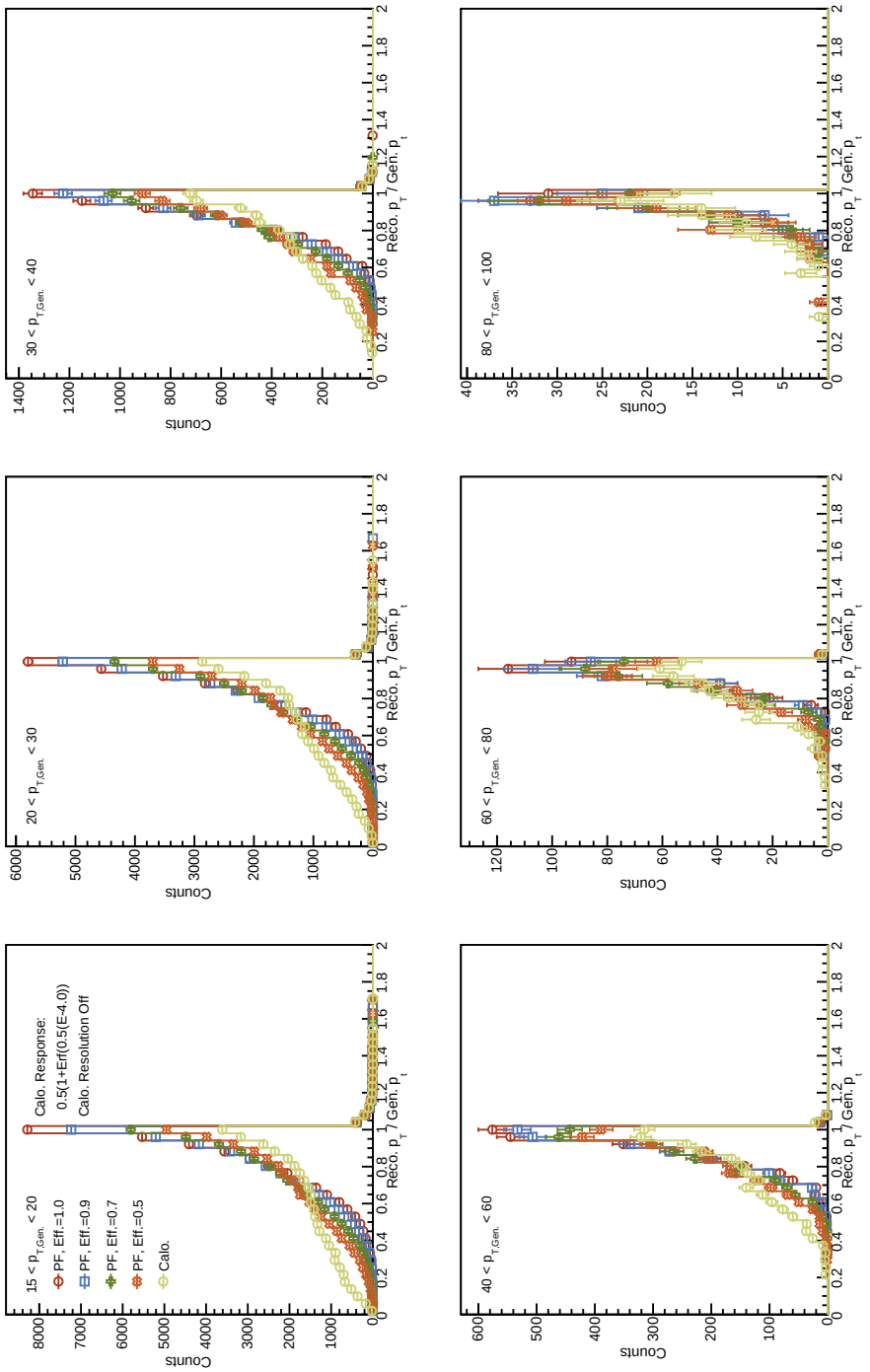

Figure 5-14: Similar to Figures 5-12, jet energy response comparing toy particle flow implementation for a few different imposed tracking efficiencies to calorimeter jets. There is no added energy resolution in the calorimeters but now strong non-linearity is imposed using a wide error function centered on 4 GeV. From left to right, top to bottom in panels, the response is binned as a function of particle level jet transverse momentum, from $15 < p_{\mathrm{T}} < 100$. With strong calorimeter non-linearity, the advantages of particle flow implementations are significant in response and resolution.

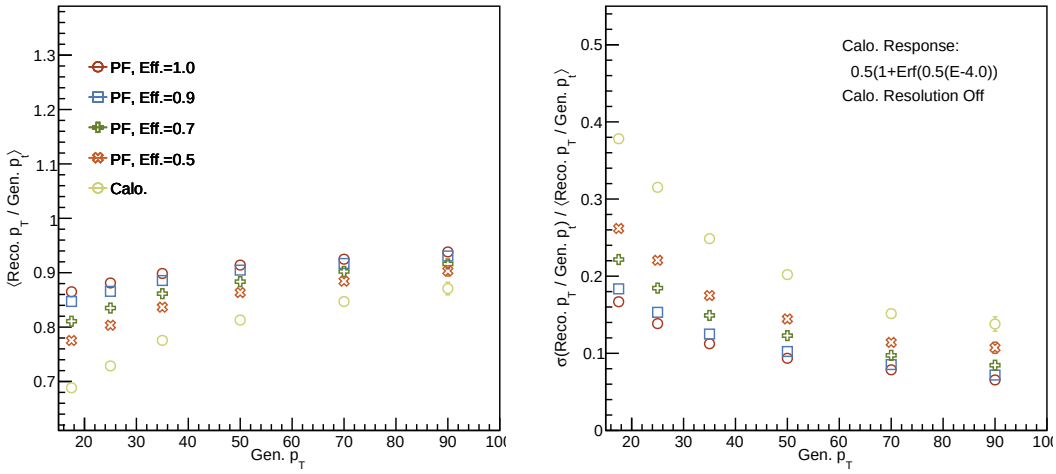

Figure 5-15: Mean and width of response plots as shown in Figure 5-14, comparing toy implementation of particle flow to calorimeter reconstruction for a few imposed tracking efficiencies and significant calorimeter non-linearity, but no additional single hadron resolution. Considerable improvement to resolution is observed in particle flow implementations, as well as higher response. The latter necessitates fewer corrections of smaller magnitude to bring jet response to unity, another advantage of particle flow algorithm.

2. Fake track rate effectively zero

    - If this is not satisfied reconstruction performance can actually become worse than calorimeter jets, particularly at high-p_{T} where fake track spectra will likely outstrip real production

3. Effective for tracks with few hits for electrons and nuclear interactions from CMS high material budget

4. Effective vertexing capability for handling both displaced vertices and pileup

5. High granularity ECal in η-ϕ space

    - Maximize unique ECal cluster association

6. Excellent ECal energy resolution

    - As 30% of jet energy remains in ECal with particle flow, the mitigation of typical HCal non-linearities will be ineffective if the ECal is poor

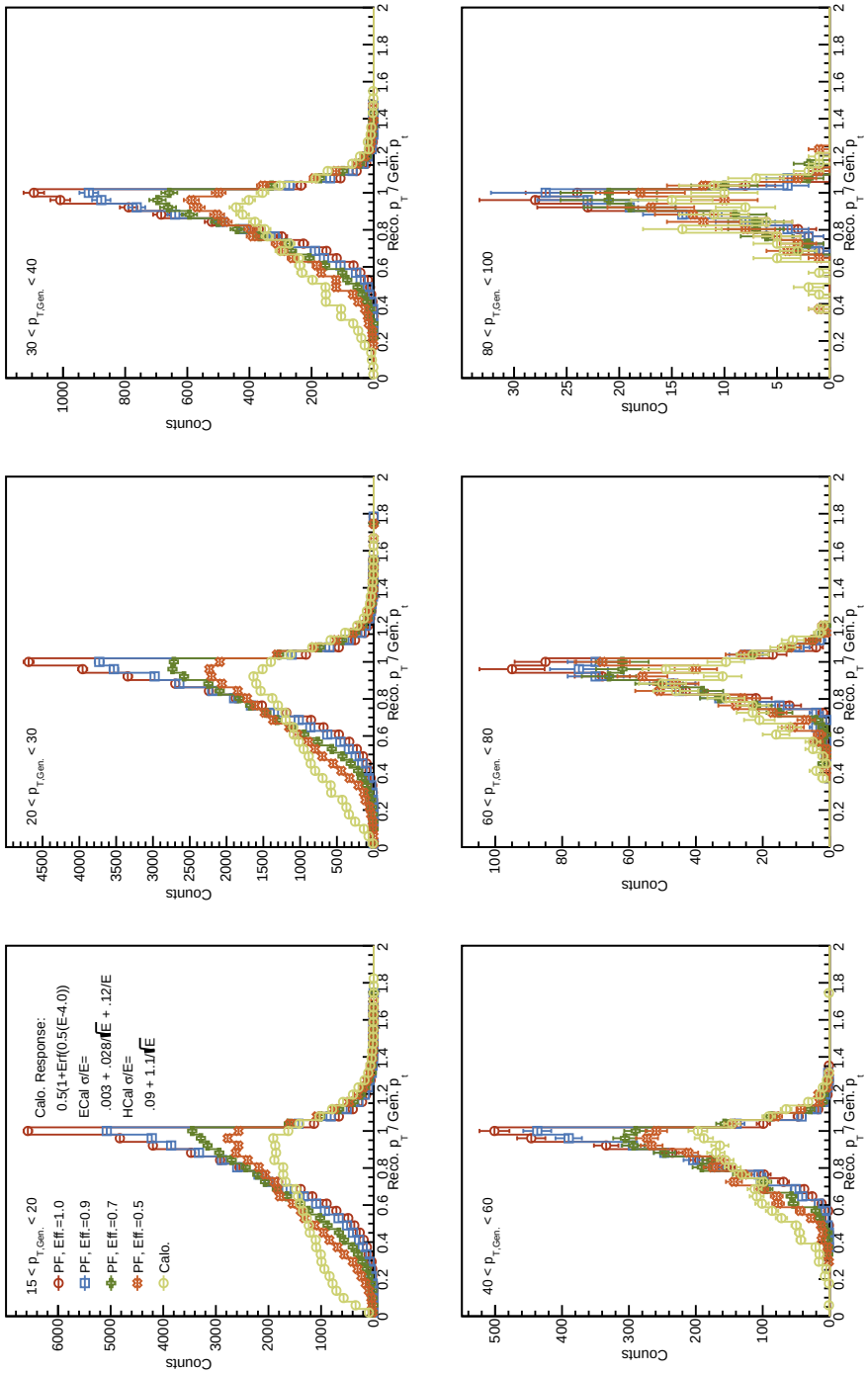

Figure 5-16: Jet energy response comparing toy particle flow implementation for a few different imposed tracking efficiencies to calorimeter jets. Single hadron calorimeter energy resolution is now added to the strong non-linearity as imposed in Figure 5-14. From left to right, top to bottom in panels, the response is binned as a function of particle level jet transverse momentum, from $15 < p_{\mathrm{T}} < 100$. Particle flow improvements globally significant for both mean response and resolution

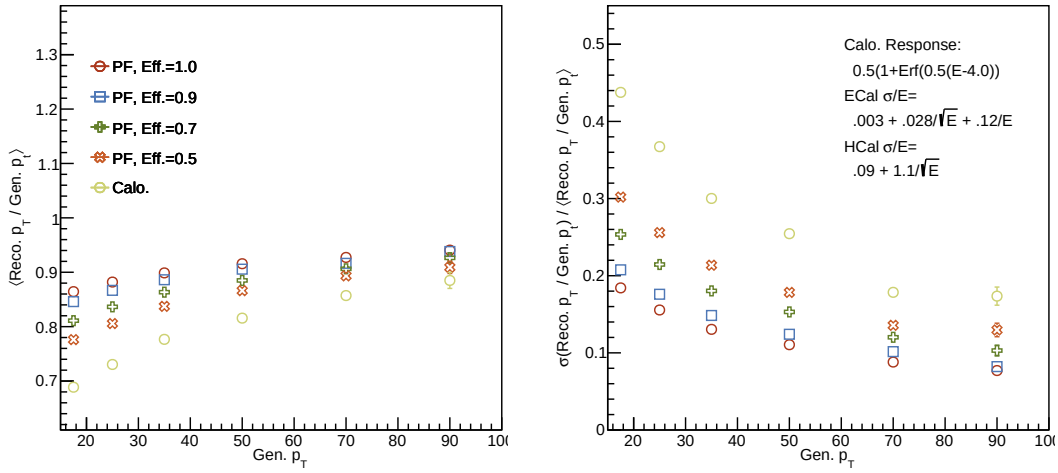

Figure 5-17: Mean and width of response plots as shown in Figure 5-16, comparing toy implementation of particle flow to calorimeter reconstruction for a few imposed tracking efficiencies and significant calorimeter non-linearity with realistic single hadron resolution. Considerable improvement to resolution is observed in particle flow implementations, as well as higher response.

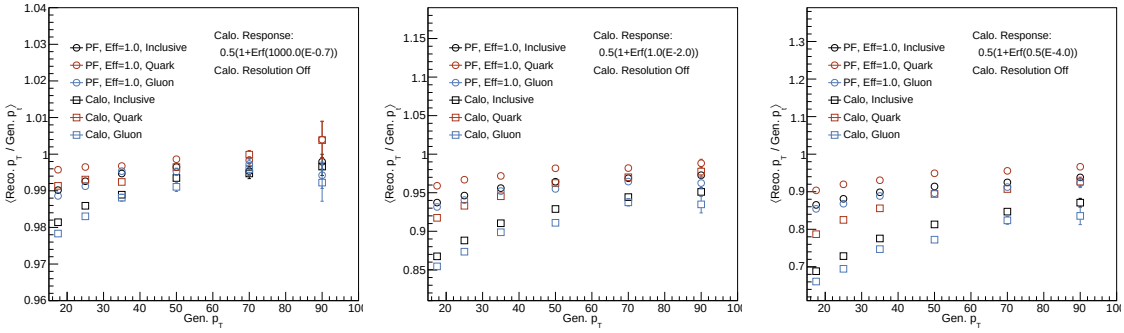

Figure 5-18: Difference in mean jet energy response for quark and gluon jets run through toy particle flow and calorimeter jet reconstructions. From left to right, non-linearity progresses from sharp error function terminating at 700 MeV to strongest non-linearity as imposed first in Figure 5-14. The width of the quark-gluon jet difference is always greater in calorimeter reconstruction than it is for toy particle flow. This width increases with non-linearities. In situations where the jets initiating parton flavor is not well known, the increasing spread in response necessitates increased systematic error.

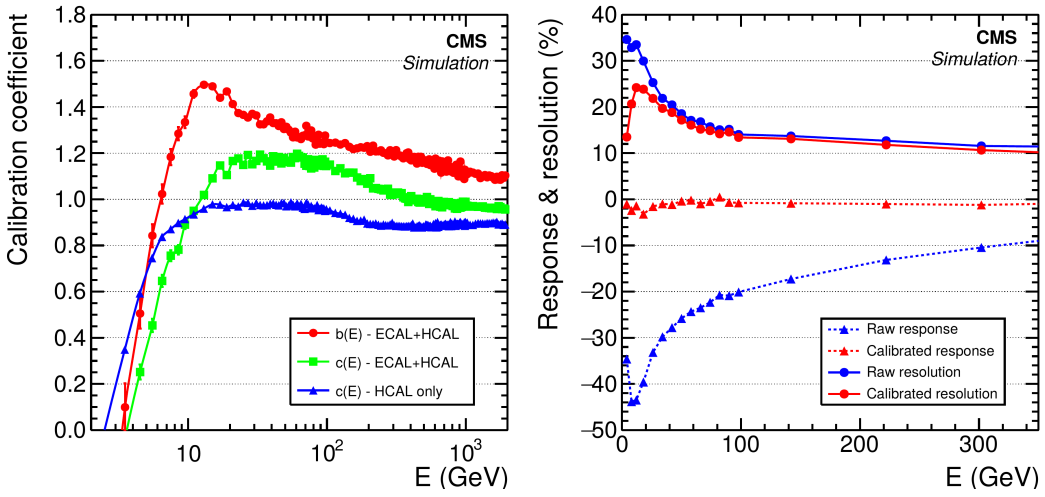

Figure 5-19: Calorimeter response and corresponding calibration coefficients under single hadron/photon deposition hypothesis. The choices of error function in toy particle flow implementation are clearly a reasonable facsimile of the true, uncorrected of the HCal performance. For remaining resolution after correction under single hadron hypothesis, see Fig. 5-10. Figure via [72].

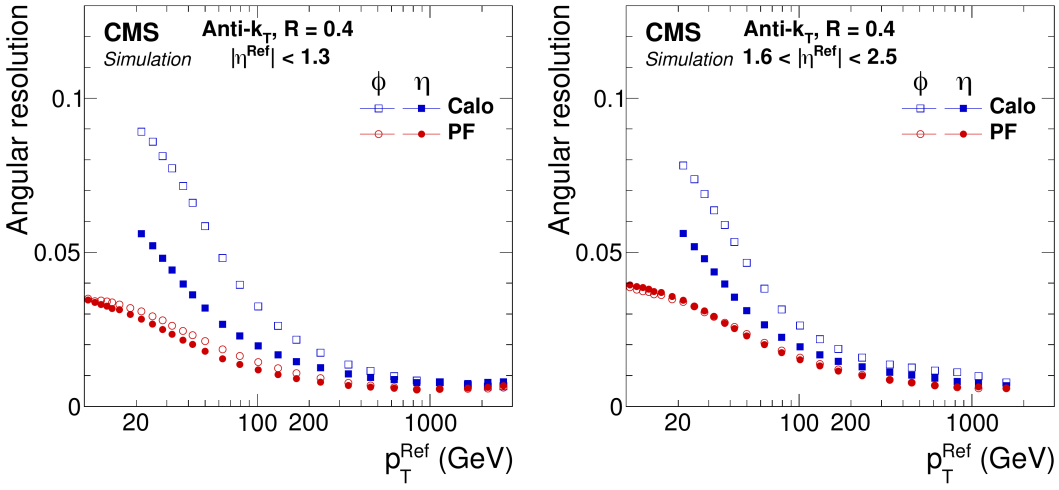

Figure 5-20: Angular resolution of the particle flow and calorimeter jet reconstruction in $\eta - \phi$ space as a function of jet transverse momentum. Figure via [72].

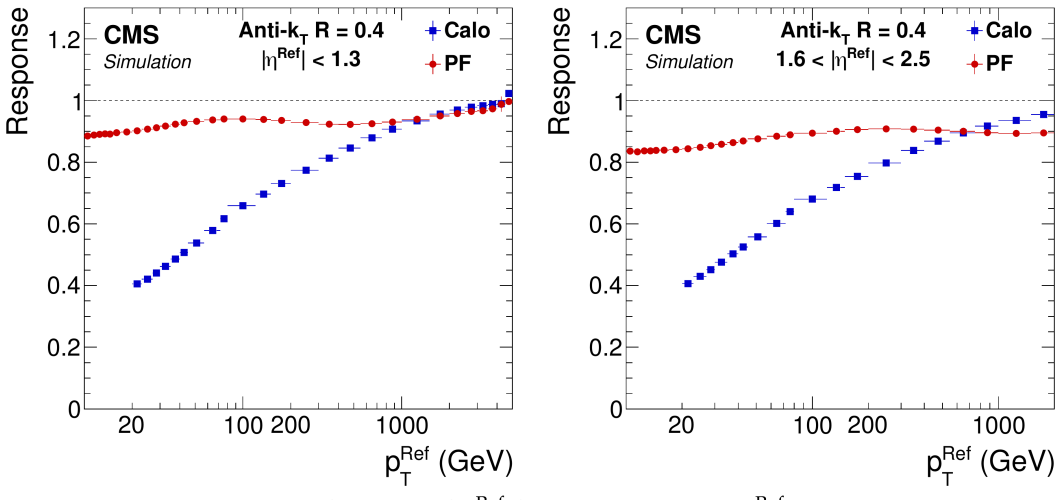

Figure 5-21: Raw response for particle flow and calorimeter jets. Raw response is flatter as a function p_{T} and requires less correction overall to achieve unity when compared to calorimeter jets. Figure via [72].

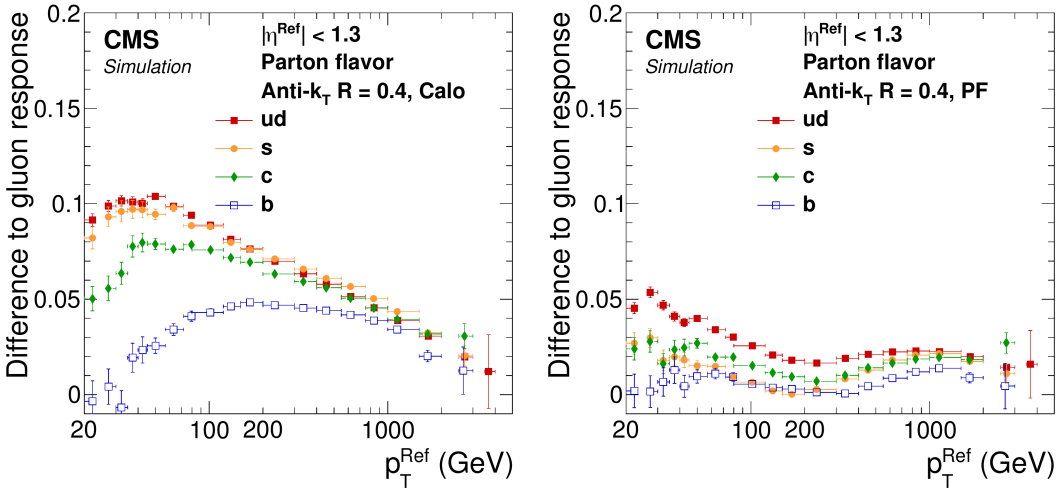

Figure 5-22: Difference in raw response between gluon jets and various flavors of quark jet for calorimeter (left) and particle flow (right) jets. Particle flow jets substantially reduce the difference between the two populations, which is essential in reducing systematic error when flavor is uncertain. Figure via [72].

All of these requirements make implementation in pp an already daunting task (the original implementation at ALEPH being in the much cleaner collisions of electrons and positrons). Every problem of implementing the above criteria for proton-proton collisions is made worse by the particle multiplicities in central PbPb collisions, where a 0-5% event produces particle multiplicities as measured by CMS of roughly 2000, as shown in Figure 5-23 in the mid-rapidity $\pm$ 1 region [82]. The problem is twofold - is particle flow reconstruction possible, and if so is there still any benefit in heavy ions? The answer to the former is yes, as will be discussed. As to the benefits in jet reconstruction, in heavy ion it remains true although in subtler ways.

As far as implementation, even in central-most PbPb events, the tracking subdetector operates at sub-percent levels of occupancy. The primary limitation in PbPb tracking reconstruction is not hardware level, but in terms of the computational time of running iterative tracking algorithms at heavy ion densities. As a result, a modified tracking algorithm is employed in heavy ions compared to pp. While this keeps computation time manageable, it comes at the cost of some efficiency. As a result, heavy ion particle flow jet reconstruction, even in the absence of background, has a slightly worse energy resolution than that found in pp reconstruction (this is the effect of performance reverting to that of calorimeter jets, or an increased S term in relative resolution parametrization).

Calorimeters, in particular at HCal granularity of $\Delta\eta$ x $\Delta\phi$ 0.087 x 0.087, are approaching full saturation in central PbPb events, and thus some of the hypotheses about unique particle associations are lost. A quick calculation using CMS $\mathrm{dN/d}\eta$ multiplicities as reference point leads to roughly 75% tower occupancy in 0-5% (1.5 particles per tower, assuming a Poisson distribution). While there is a host of reasons why this calculation is too simple ($\mathrm{dN/d}\eta$ extends to zero while only particles greater than 700 MeV make it to the ECal, pixel tracks are comprised of charged particles while the HCal also measures neutrals), a quick plot from the central PbPb data of particle flow candidates paints a picture similar to this naive expectation, in Figure 5-24.

There are two reasons why even in the high-density PbPb collisions that particle

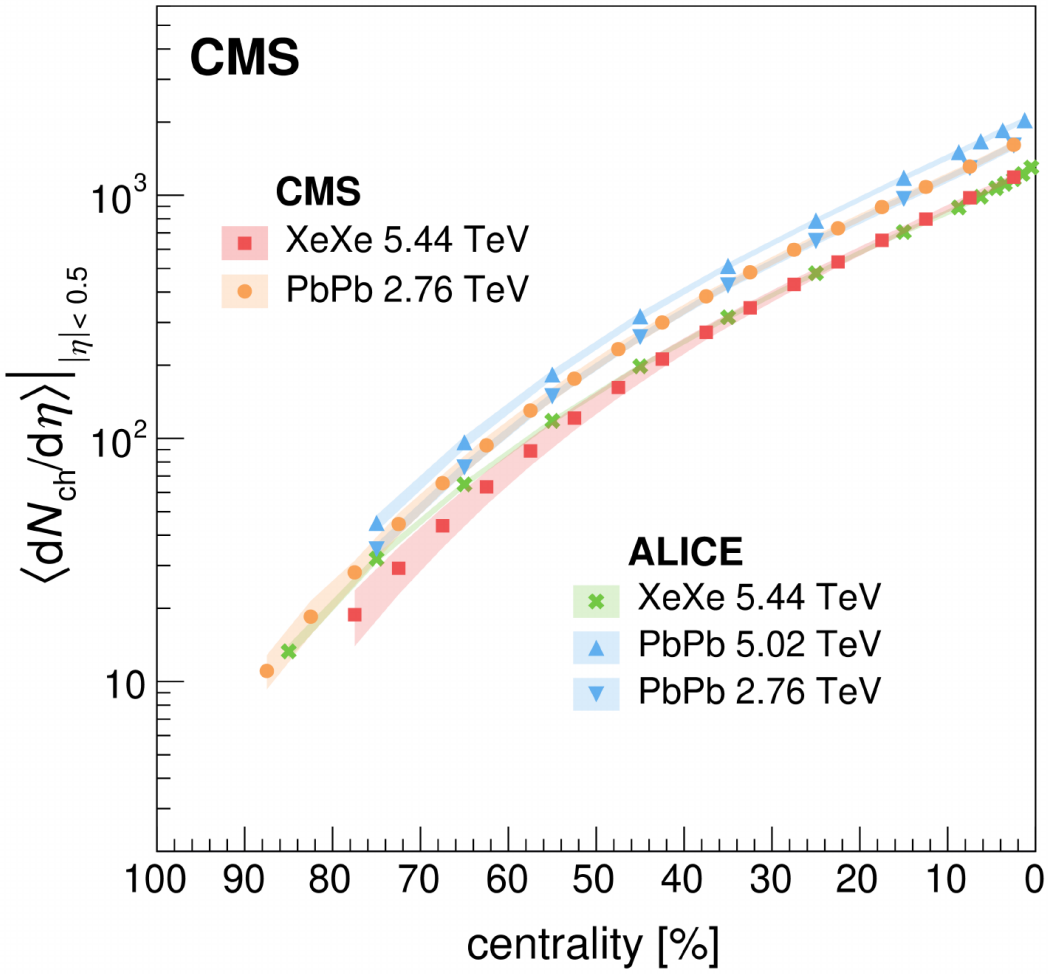

Figure 5-23: Charged particle multiplicities in PbPb and XeXe collisions from CMS and ALICE, overlaid. Used for rough calorimeter saturation calculations indicates a sizable fraction of total HCal towers at mid-rapidity remain empty. Figure via [82].

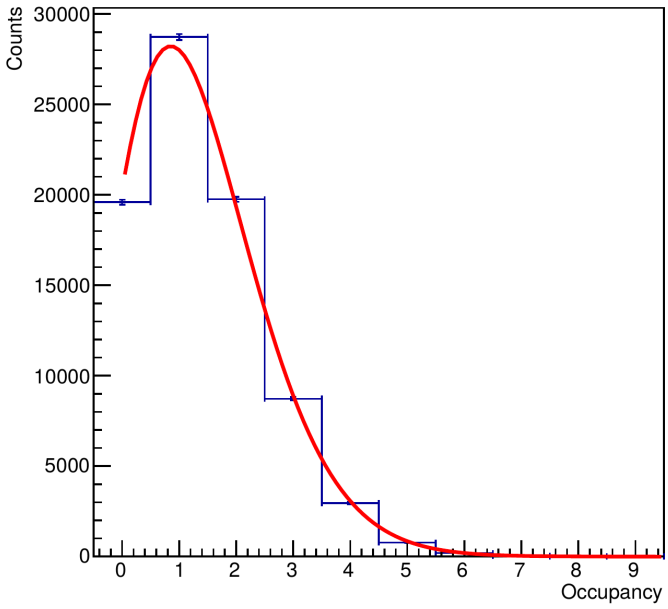

Figure 5-24: HCal occupancy for central PbPb events taken directly from data. 25% of towers are empty for a central-most PbPb event. Poisson fit fails χ^2 compatibility, but serves as a reasonable adhoc description of the overall behavior.

flow remains superior to calorimeter jets. They are

1. Reduced bias in jet response due to fragmentation (illustrated in pp by comparing differing response by jet parton flavor in Figure 5-22).

2. Greater constituent granularity for substructure study.

Notably not on this list is improved jet energy resolution. This is because in PbPb, the N term of our CSN resolution parametrization dominates and particle flow does little to drive this term down in PbPb events (the proton-proton method for controlling this term involved vertexing technique not viable in PbPb). While PbPb does retain the reduction in S term, the increased N term washes out the gain.

However, the S term is meant to characterize calorimeter sampling and is also related to the response split between jet parton flavors. Despite the overall resolution being dominated by noise, you retain the reduced split in average response (squeezing the bimodal distribution light quark and gluon initiated jets). This is invaluable in PbPb where there is a great deal more uncertainty on the flavor of a final-state

collection of jets. The reduced split in flavor response translates directly to reduced error in jet energy scale.

The second reason is specific to substructure measurements dealing directly with the jet constituents. Here, having constituents as close as possible to particle level is essential to the measurement. For example, for splitting function measurement, the declustering procedure usually is done with Cambridge/Aachen algorithm, which as will be discussed in the next chapter, uses constituent angular information without momentum weighting. In calorimeter jets defined on a fixed tower grid, the choice of what is clustered first is arbitrary absent an energy weighting. Furthermore, combination of many particles into single towers reduces subjet resolution, as the point at which you might have terminated declustering might have happened mid-tower energy if you could resolve the individual particles. The error on the measurement is reduced significantly when performed with a particle flow reconstruction.

Chapter 6

Jet Reconstruction

Jets are, at core, an agreed upon set of algorithms that are reconstructable experimentally with good control and calculable theoretically. The experimental requirements impose

- Regular geometry for consistent, correctable detector response
- Resilient $\eta - \phi$ centroid and energy after subtraction when in presence of background

Satisfying these requirements during the first data-taking periods at the LHC meant employment of algorithms such as iterative cone [24]. These were effectively energy sums around a seed with some limited iteration looking for alternative local maximum. The regular cone satisfied regularization necessary for correction and subtraction, and application to calorimeter towers of regular spacing and finite width gives computation times favorable when compared to alternative offerings. However, iterative cone fails infrared-collinear safety requirements in jet physics that make results theoretically calculable. Specifically, to give sensible answers jets (and related observables) must be

1. Invariant under the radiation of an arbitrary number of infinitesimally soft particles
2. Invariant under collinear splittings into hard fragments

Take for example the calculation of jet spectra. If the number of jets you count depends on whether a hard fragment is split into one or two particles (as is the case for iterative cone jet reconstruction as employed at CMS for first jet results), then divergences are introduced in theoretical calculations (see appendix of [83] for example of this failure).

The class of algorithms typically employed in jet physics at hadron colliders that solve this issue while retaining the desired experimental behavior are known as sequential recombination algorithms, and are the topic of the next section.

6.1 Algorithms for Jet Physics

Given a set of input constituents, which can be particles in case of Monte Carlo generator, calorimeter towers for calorimeter jet, and particle flow candidates for particle flow jet, the family of algorithms employed in typical jet measurements at hadronic colliders are known as sequential recombination algorithms. The basic principle behind these algorithms is iterative combination of pairs of particles that minimize a chosen distance metric, until the set of available constituents is exhausted or terminating condition is satisfied. The distance metric is defined here (for inclusive clustering) as

$$d_{i,j} = \text{Minimum}(k_{t,i}^{2p}, k_{t,j}^{2p}) \frac{\Delta_{i,j}^2}{R^2} \tag{6.1}$$

for all possible particle / intermediate jet (hereon-out referred to as pseudojet) pairs i,j. The quantity k_{T} is the particle transverse momentum, substituted for p_{T} here for consistency with implementation papers [84, 83, 85]. R is the jet resolution parameter chosen for specific physics purpose, with typical values of 0.4 in $\eta - \phi$ for light quark or gluon jets, and 0.8 for boosted heavy boson or top quarks. Δ is the angular distance between pseudojets, defined

$$\Delta = \sqrt{(\Delta\phi)^2 + (\Delta y)^2}. \tag{6.2}$$

There is an additional calculated quantity per pseudojet that defines condition to remove pseudojet from pairing list as fully reconstructed jet

$$d_{i,B} = k_{t,i}^{2p}. \tag{6.3}$$

A naive implementation of the algorithm, which gives identical results to more sophisticated implementation in FASTJET [85] package for timing purposes, proceeds as follows

1. Full pseudojet list identifies particle pairing that minimizes Equation 6.1 or single pseudojet minimizing Equation 6.3.

2. If it is a pseudojet pair that minimizes distance metric, pseudojet pair is combined into single pseudojet

    - Typically this is done via four-momentum sum, although alternative combinations are possible

3. If it is single pseudojet that minimizes distance metric, pseudojet is removed from particle list as a final jet

4. Iterations continue until pseudojet list is exhausted

The above procedure is fully infrared and collinear safe. However, there is still a parameter to be specified, p. There are clearly only three truly independent choices to be made for p: p = 1, 0, -1. All other positive choices of p will return identical minimum to p = 1, while all other negative choices of p will return identical minimum for p = -1.

Choosing p = 1 is known as k_{T}-algorithm, and is the original sequential combination algorithm. The algorithm replicates the momentum ordering of fragmentation from harder to softer fragments, by preferentially combining the softest, local fragments first building backwards to parton. Choice of p = 0 is known as Cambridge/Aachen algorithm, and is a pure consideration of angular distribution of constituents. In this sense, it replicates angular ordering of fragmentation, clustering

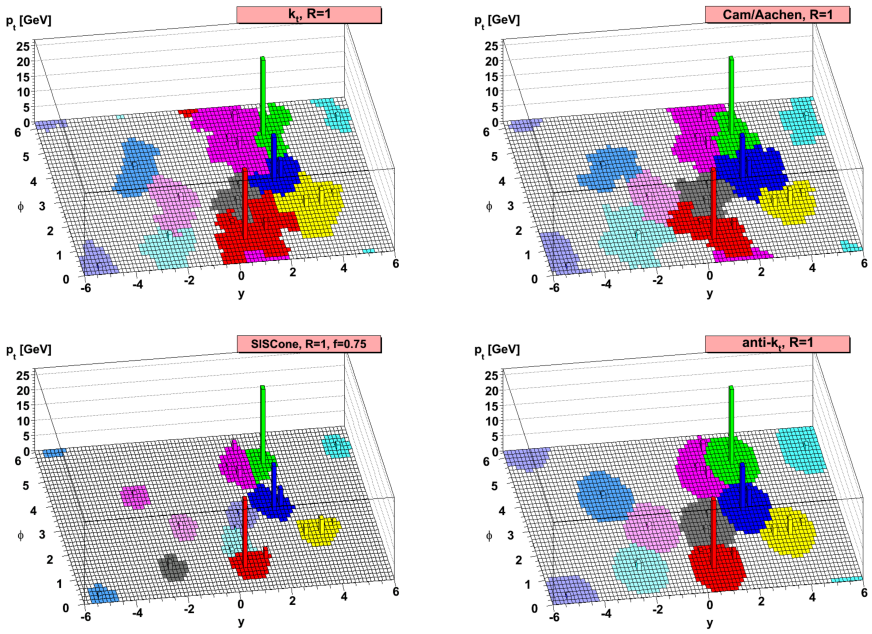

Figure 6-1: An event display comparison of different jet clustering algorithms. Top two displays, k_{T} and Cambridge/Aachen give jets with irregular shapes that pose a problem for response correction and subtraction. In bottom right, anti-k_{T} gives regular cone-like jets ideal for experimental purposes.

closest particles first. The final choice, p = -1, is known as anti-k_{T} algorithm, and while it retains infrared and collinear safety there is no clear underlying physics to motivate its choice. Nevertheless it is the most common algorithm choice experimentally, as it replicates the regular geometry of iterative cone algorithms, as shown in Figure 6-1, taken from [83].

6.2 Jet Reconstruction in Heavy Ion Collisions

The primary goal of jet reconstruction, insomuch as it can be defined purely from the perspective of detector/algorithm performance, is to minimize angular and energy resolution without introducing biases to response for different fragmentation patterns (with additional, related goals of minimizing fake jet reconstruction while maximizing efficiency). Of this criteria, the most effort is spent minimizing jet energy resolution without introducing significant response biases. Relative jet energy resolution is typ-

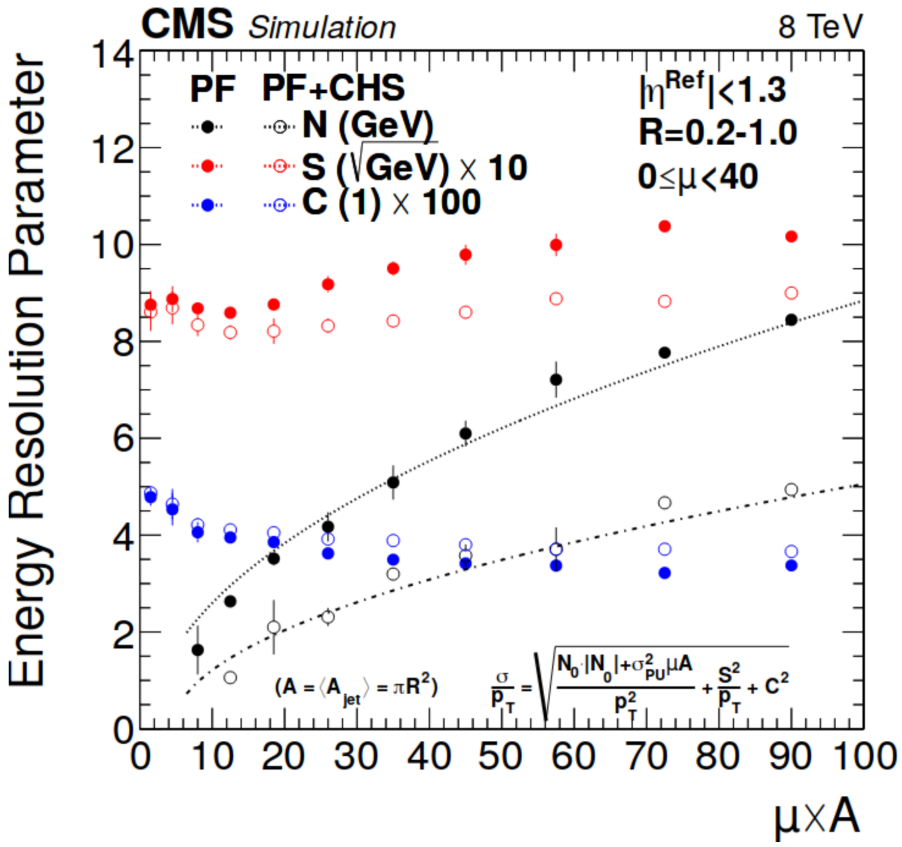

Figure 6-2: Relative resolution parametrization in CMS jet reconstruction for proton-proton collisions [72]. While constant and stochastic parameters (C and S) are stable over a wide range of jet areas and average pileups, the N parameter scales quadratically (as anticipated). The contribution of noise to relative resolution is reduced with the addition of charged hadron subtraction, a technique the exploits vertex information in underlying event that comes from pileup. This technique is not applicable in collisions of heavy ions.

ically parametrized as

$$\frac{\sigma(p_T)}{p_T} = C^2 \bigoplus \frac{S^2}{p_T} \bigoplus \frac{N^2}{p_T^2} \tag{6.4}$$

where the C, or constant term, induces width always proportional to jet energy, S, or stochastic term, scales as the square root of the momentum and is an effective Poisson sampling contribution, and the N, or noise term, is what accounts for the contributions of underlying event. Reduction of this last term is the primary focus of jet reconstruction effort in heavy ions, as will be discussed in Section 6.2.1.

The parametrization of relative jet energy resolution and its dependence on under-

lying event contributions in proton-proton collisions is shown in Figure 6-2. Notably, as cone size and number of pileup vertices is increased (left to right along x-axis), the C and S terms remain relatively stable while N increases quadratically, as would be expected from a naive area intuition stemming from iterative cone style jets. While it is not actually the case that the S and C parameters should be unchanging with cone size, it is clear that the dominant effect is on noise contributions to resolution.

6.2.1 Magnitude and Characteristics of Heavy-Ion Backgrounds

The production of uncorrelated particles contaminating signal of interest is characteristic of hadronic and nuclear collisions, in contrast to the much cleaner collisions with a leptonic component. The uncorrelated particles can and should be corrected for in most measurement. This component of the raw data to be removed in measurements of hard-scattered partons is called underlying event, or UE. Techniques developed for their removal in jet measurements are referred to as background subtraction. Subtraction techniques typically exploit the different characteristics of particles produced in hard-scattering in contrast with those from uncorrelated softer scatterings. As example, the particle production from softer scatterings will typically be much lower in momentum than those from hard-scattered partons reconstructed as jets. The Soft-Killer subtraction method exploits this difference by extracting a minimum transverse momentum event-by-event, only clustering those particle above the cut [86]. While this method can induce strong biases in detector response based on whether a jet fragments into a harder or softer set of particles, and is therefore not typically employed experimentally, similar momentum considerations are incorporated in many other more sophisticated methods.

Fig. 6-3 is a Monte Carlo illustration of underlying event as it is produced in proton-proton collisions.

Going from proton-proton collisions to PbPb collisions, there are three primary differences in the production of underlying event. The first is in the magnitude of the fluctuations. In proton-proton collisions, the pileup up to the current date has ranged from 0 to 60 simultaneous collisions, with the typical pileup being around 40 in

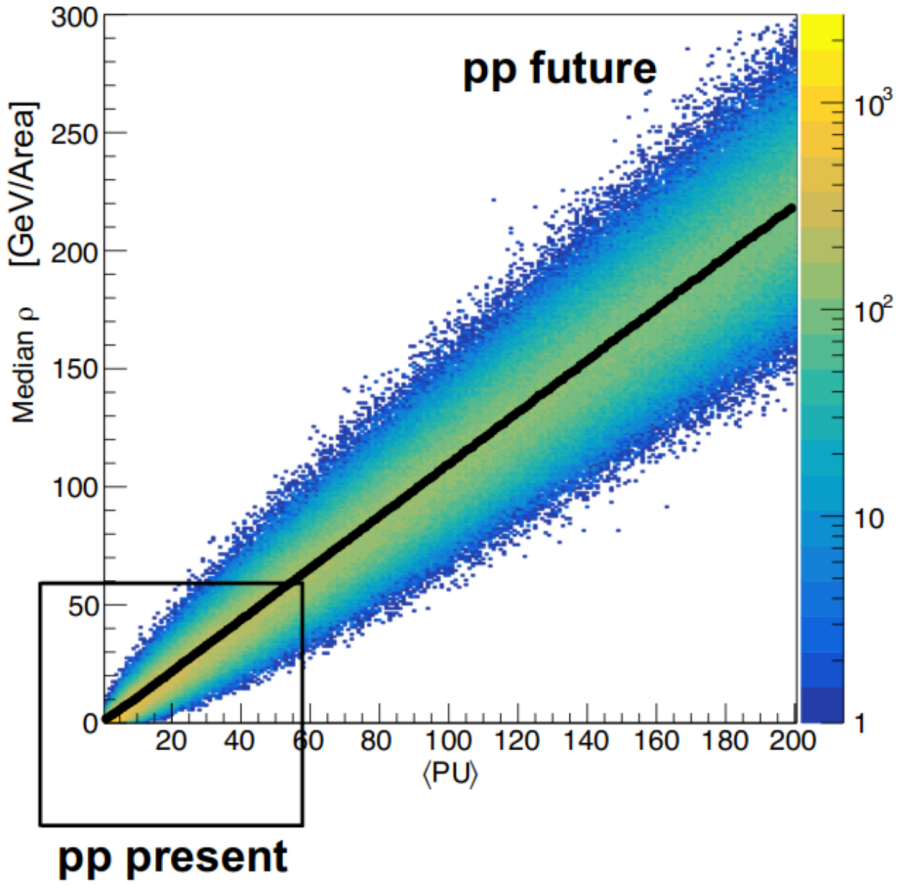

Figure 6-3: A Monte Carlo demonstration of underlying event from pileup, the primary source of background in proton-proton collisions at the LHC. Independent minimum bias PYTHIA8 events are combined, with the number of events picked from a Poisson distribution of mean value corresponding to $< PU >$ on the x-axis. The ρ is extracted by summing the particle transverse momentum in a random cone, normalized by the cone area. The fluctuations in UE about the clear linear trend of the mean come from both fluctuations in the number of pileup events and from the fluctuations in per event soft particle production. As an approximation, the mean ρ scales as roughly 1 GeV/area per mean pileup.

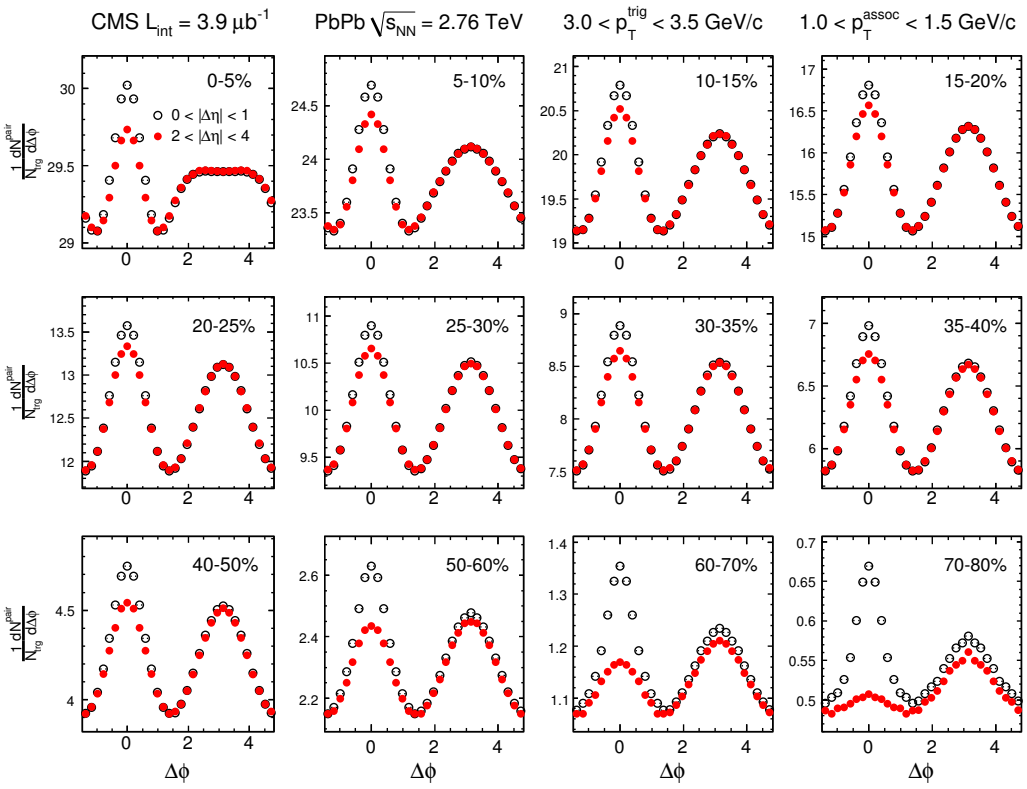

Figure 6-4: Long range azimuthal correlations of soft particles as measured by the CMS experiment [4].

recent years. This corresponds to an approximate ρ of 40 GeV/area. In central PbPb events, which dominates both the jet production cross section and also the magnitude of quenching effects, the typical ρ is five times this value, as seen in Fig.6-5. Second, the soft particle production comes from many vertices of displacements along the beamline of order centimeters, something easy to resolve with CMS vertexing [87]. Thus individual particles can be labeled as coming from the vertex of hard-scattering, or from uncorrelated softer scattering vertices. In contrast, all particles produced in lead ion collisions come from longitudinal region of ten femtometer, and vertexing techniques are not viable with currently available detectors and techniques.

Finally, the typical underlying event produced from pileup collisions has no azimuthal structures event-by-event. Particles produced at each vertex are emitted in effectively isotropic configurations relative to each other. In PbPb collisions, long

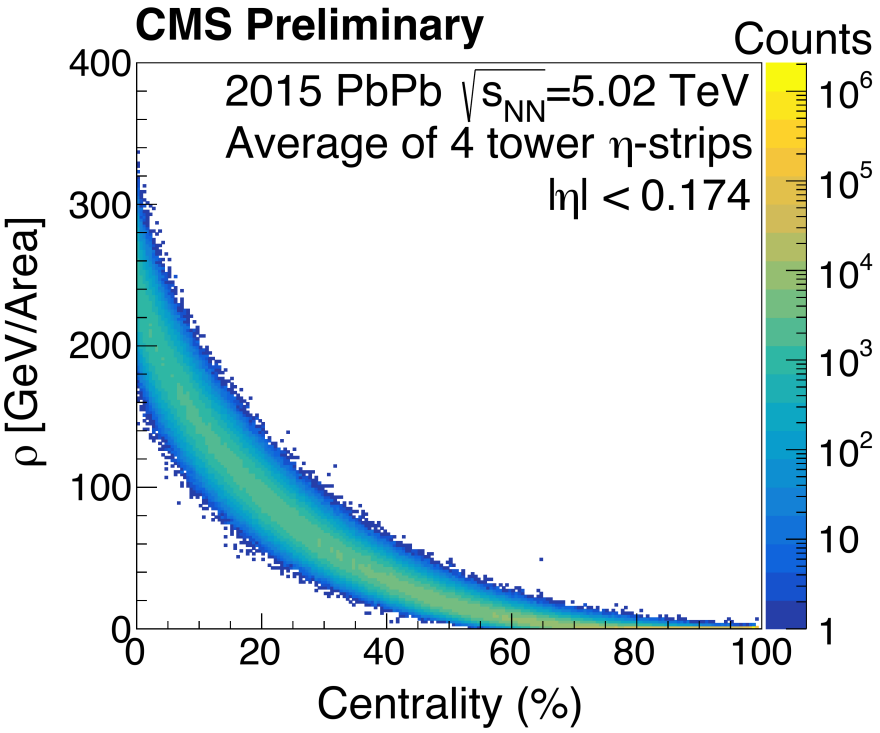

Figure 6-5: Average underlying event density as a function of centrality, extracted from the average of the middle 4 HCal tower strips in η in minimum bias PbPb data taken in 2015 with the CMS detector. The underlying event magnitude spans an enormous range, all of which must be well-controlled to realize the full CMS heavy ions jet program [88].

range azimuthal correlations in softer particle production is a well documented phenomena of the medium, typically lumped together under the label of flow effects [4]. An example of the induced structure in soft particle production can be seen in Figure 6-4. A subtraction algorithm that does not account for these structures will have biases in jet energy scale relative to the position of the flow event plane and an artificially increased resolution. It should be noted that while flow effects have been observed in high-multiplicity proton-proton collisions, this only occurs in cases where the full multiplicity (in these special events, greater than 100 charged particles) comes from a single proton-proton colliding pair [8]. While these events are indeed more like PbPb collisions in this respect, they represent a small fraction of the proton-proton collision cross section and are in no way typical representations of underlying event.

Given the significant differences on the production of underlying event in PbPb collisions, the approaches taken to handle underlying event in proton-proton collisions such as charged hadron subtraction and Pile Up Per Particle Identification (PUPPI) are not applicable [89]. Instead, two subtractions have been employed at CMS in PbPb collisions in recent years: iterative pedestal subtraction, or PU, and constituent subtraction, or CS. The choice of subtraction technique is driven by analysis and physics phenomena of interest, but in general when the jet as macroscopic object is the primary probe, iterative pedestal is used. When instead, the jet substructure is being probed, constituent subtraction is employed.

6.2.2 Iterative Pedestal Subtraction at CMS

Implemented as described in [90], iterative pedestal subtraction has been employed in many results studying the direct modification of jet energy [24, 25, 26, 27, 31, 50, 67, 68, 69]. While in most cases the inputs are particle flow candidates, the candidates are combined into pseudotowers following the the geometry of the HCal, $\Delta\eta$-$\Delta\phi$ of 0.087 x 0.087 at mid-pseudorapidity. The mean and width of pseudotower transverse energy is calculated per η-strip. Pseudotower transverse energy is corrected by subtracting of the calculated mean plus one sigma, the calculated UE pedestal. Pseudotowers with negative energy after this subtraction have energy set to zero. The additional subtraction of the transverse energy width is meant to compensate for this zeroing, removing negative contributions. Note that in the original iterative pedestal proposal, the compensating subtracted sigma has a prefactor that can be tuned. In CMS implementation, the prefactor is set to one always.

Subtracted towers are then clustered into jets using the anti-k_{T} sequential recombination algorithm as encoded in the FASTJET software package [85]. Jets above a chosen $p_{\mathrm{T}}^{\mathrm{jet}}$ cutoff (in CMS analysis this is 15-20 GeV) from this first iteration are used to identify the jetty regions which can bias the uncorrelated soft UE estimation. To reduce the bias resulting from hard-scatterings, a second iteration is then performed. This time, towers within a $\Delta\eta$-$\Delta\phi$ cone around the identified jetty regions are excluded in the estimation of mean and width of pseudotower transverse energy.

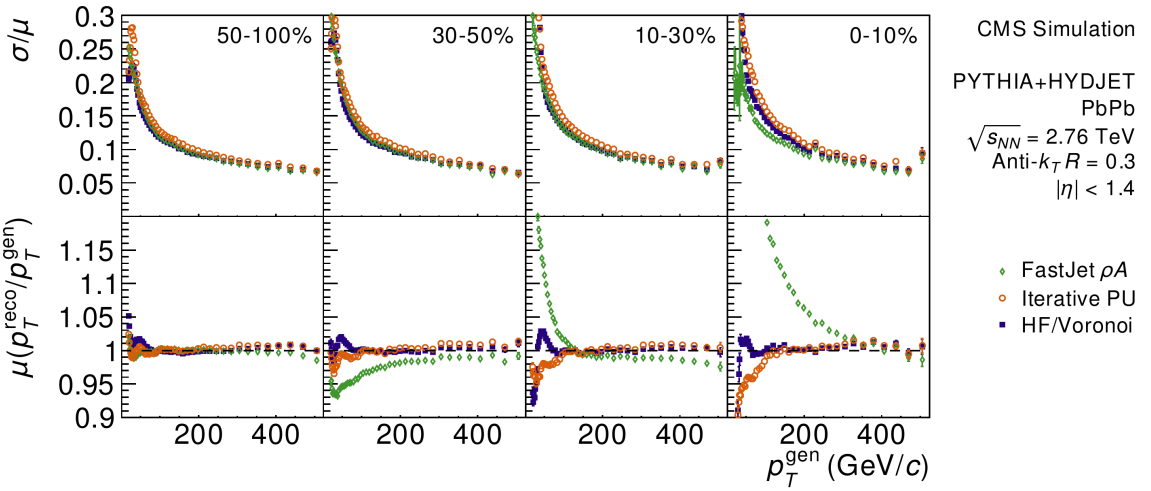

Figure 6-6: A comparison of different subtractors as implemented for the CMS detector in $\sqrt{s_{NN}}$=2.76 TeV PYTHIA+HYDJET events. Jet area [91], iterative pedestal [90], and HF/Voronoi [92] techniques are shown. While jet area technique control of scale fails completely in central most PbPb events, iterative pedestal and HF/Voronoi give a reasonable range of control. HF/Voronoi outperforms iterative pedestal in jet energy resolution. In the future, simplified implementations of HF/Voronoi technique may be preferred [88].

Caps on the number of excluded towers per η strip can be employed to prevent large fluctuations in the estimation per η-strip (depending on position in HCal, the number of towers is only 72/36). With recalculated mean and sigma for reduced jetty bias, pseudotower subtracted energy is recalculated, negative towers are zeroed, and the remaining set of towers is again clustered using the anti-k_{T} sequential recombination algorithm. The clustered set of jets in this second iteration is final.

Figure 6-6 shows the performance of iterative pedestal subtraction in fully simulated CMS reconstruction as compared to the FASTJET native area subtraction [91] and a proposed alternative technique, HF/Voronoi [92]. While simple area subtraction results in significant scale non-closure in central-most events, iterative pedestal maintains response within 5% down to 50 GeV. The alternative proposed subtraction, HF/Voronoi outperforms iterative pedestal in scale closure and minimizing resolution. This is at least in part because HF/Voronoi maps of underlying event properly accounts for azimuthal correlations in soft particle production, while in iterative pedestal this is not accounted for and results in an increased response width. Furthermore, the

HF/Voronoi algorithm involved no zeroing of negative towers, and therefore requires no additional compensating subtraction of transverse energy sum sigma. It is this zeroing and compensating subtraction that results in central scale non-closure (via over-subtraction). HF/Voronoi's improvements in this respect were overshadowed by complexity of implementation. However, in Section 6.3, a synthesis of iterative pedestal and constituent subtraction techniques addresses both issues while retaining simplicity of implementation.

6.2.3 Constituent Subtraction at CMS

First employed in CMS as a background subtraction method for measurement of the jet splitting function in pp and PbPb collisions [52], and again in measurement of groomed jet mass [70], constituent subtraction is a novel technique introduced to preserve jet substructure when correcting for background contributions to jet energy [93], [94]. Iterative pedestal subtraction as implemented for the CMS detector actively destroys jet substructure by reducing particles to pseudotowers. Since jet measurements employing this technique are only interested in the non-substructure jet quantities, this is acceptable. However, in cases like the splitting function which acts recursively backward thru the clustering history to find a subjet pair satisfying a certain parton splitting condition, pseudotowers represent an unacceptable bias.

Constituent subtraction is a particle level subtractor that exploits technology developed in the estimation of jet area for sequential combination algorithms to subtract off average energy without any resulting negative values. Jets clustered with IRC-unsafe algorithms such as iterative cone, while effectively unusable by theorists, did have advantages from the experimentalist perspective of simplicity and area definition. With the widespread adoption of sequential combination algorithms like k_{T}, Cambridge-Aachen, and anti-k_{T}, the notion of jet area became ambiguous. k_{T} and Cambridge-Aachen clustered jets had fluctuating, irregular shapes, and while anti-k_{T} retained many of the regularizing properties of iterative cone, the possibility of overlapping jets meant area was still not a simple $\Delta\eta$-$\Delta\phi$ cone defined by jet resolution parameter R. To solve this problem, an effective Monte Carlo approach was taken.

Large multiplicities of virtual particles known as ghosts of infinitesimally small energy are added to the event. These particles are included in the jet clustering, and jet area scales directly with the number of clustered ghost particles [95]. Specifically, if N ghosts are added to detector area A, and n of the N ghosts are clustered, then the jet area is n $\times$ N / A.

Constituent subtraction takes the ghosts used in the calculation of area, and adds an associated four-momentum based on some estimator of ρ. In constituent subtraction implementations used in splitting function and groomed jet mass studies, ρ is extracted by clustering unsubtracted constituents into a set of k_{T} jets, and taking the area and energy of the median k_{T} jet as eventwide ρ. Ghosts have an associated area they subtend, corresponding to the number of ghosts and area of the detector they populate. In CMS implementation, this corresponds to something slightly less than the HCal tower $\Delta\eta$-$\Delta\phi$ width of 0.087 x 0.087. Each ghost is assigned four-momentum corresponding to this area times ρ. In the following steps, the ghosts are used to subtract at particle level

1. Ghost and real particle pair is selected according to minimization of the distance metric defined as

$$\Delta R_{i,k} = (p_{\mathrm{T}})_i^{\alpha} \sqrt{(\eta_i + \eta_k)^2 + (\phi_i + \phi_k)^2} \tag{6.5}$$

   with α parameter tunable, chosen 1 at CMS

2. If the particle four-momentum exceeds that of the ghost, the particle four-momentum is reduced by the magnitude of ghost four-momentum, and ghost removed

3. If the ghost four-momentum exceeds that of the real particle, the ghost four-momentum is reduced by the magnitude of particle four-momentum, and real particle removed

4. This procedure continues until either all ghost or real particles are exhausted

The mechanism by which the subtraction is applied completely eliminates issues in iterative pedestal associated with zeroing negative energy after subtraction and compensating additional sigma, in addition to preserving jet substructure by subtracting at constituent level without need of intermediary pseudotowers. However, the issues of azimuthal correlations in the structure of the underlying event remains unaddressed, artificially increasing jet energy resolution. In addition, the ρ estimation method is not well suited for adjusting to the changing geometry of a typical collider detector, particularly in the forward regions. As a result, the CMS substructure measurements have thus far been restricted to an η of $\pm$ 1.3.

6.3 Updates to Constituent Subtraction

The two subtraction methods employed in the majority of CMS PbPb results as described both have a set of drawbacks. If the problem of subtraction is broken down into two components

1. Determination of the distribution of the underlying event (typically as a ρ map)
2. Procedure by which the underlying event is subtracted from the signal

it should be clear that the failures of iterative pedestal come primarily from the latter component, while the failures of constituent subtraction as implemented initially at CMS come primarily the former. Both fail in the construction of ρ maps that lack an azimuthal dependence. One possible solution that maintains the simplicity of the existing machinery is to take the extracted ρ map of iterative pedestal subtraction and insert it directly into the constituent subtraction procedure by which it can be subtracted. This results in a background subtraction that readily adapts to changing detector geometry that avoids all problems associated with zeroing and compensating additional subtraction. An azimuthal modulation can be added to transform $\rho(\eta) \rightarrow \rho(\eta, \phi)$, similar to a method employed by the ALICE collaboration [39]. The synthesis of iterative pedestal and constituent subtraction machinery at CMS, and addition of azimuthal modulation, is documented in [88].

To account for the azimuthal modulation of the soft particle production, event-by-event fits of ϕ-binned energy density with functional form

$$N(\phi) = N_0(1 + 2v_2\cos(2[\phi - \Psi_2]) + 2v_3\cos([\phi - \Psi_3])) \tag{6.6}$$

where event planes Ψ_2 and Ψ_3, defining the elliptical and triangular components of the azimuthal modulations, are calculated directly while the magnitudes N_0, v_2 and v_3 are fitted. Figure. 6-8 shows an example fit of a single event. Fitting is only performed in the mid-rapidity region of $\pm$ 1. In the forward region, the structure of the functional form remains a good approximation of the underlying event once refitting for N_0 in the forward region. While there is some understood decorrelation of

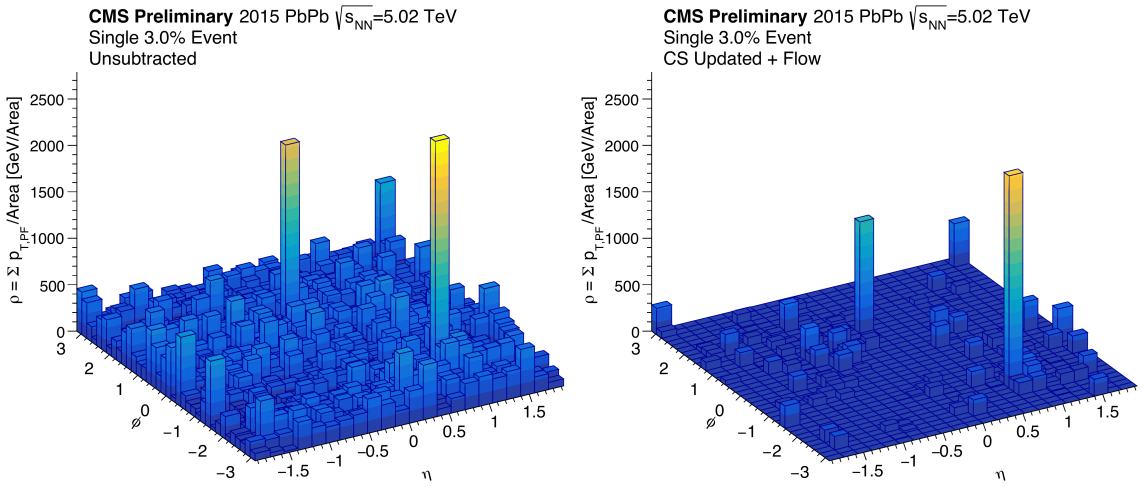

Figure 6-7: Left: Density of underlying event from nucleon-nucleon scatterings unrelated to the hard-scattering of interest before subtraction in a single central PbPb collision at 5.02 TeV, in detector coordinates of η-ϕ. Binning follows Hadronic Calorimeter Tower geometry in η, while binning in ϕ globally according to forward geometry (36 bins). Right: Density of underlying event within the same event after applying new CS subtraction with a PU-like estimation of ρ in a central PbPb collision at 5.02 TeV, in detector coordinates of η-ϕ [88].

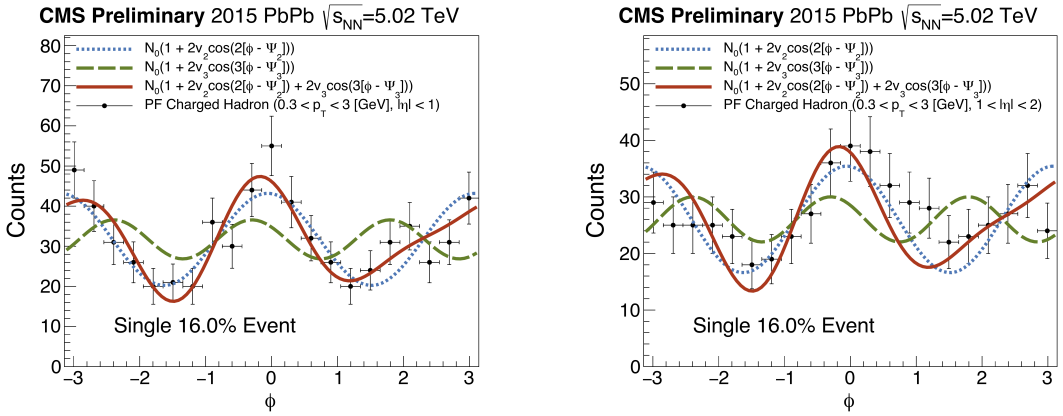

Figure 6-8: Left: Single event fit for flow as a function of detector azimuthal angle at mid-rapidity ($0 < |\eta| < 1$) for particles between $0.3 < p_{\mathrm{T}} < 3.0$ GeV/c. Right: Projection of mid-rapidity flow parameter extraction onto the forward rapidity region ($1 < |\eta| < 2$). Demonstrates mid-rapidity flow extraction is applicable through the full phase space. Event-by-Event flow fitting in ALICE [39], CMS v_2 [96]. Extraction method for v_2, v_3 uses counts rather than ρ to reduce jet contamination and to match published extractions. Baseline PU ρ_0 is then modulated in ϕ according to this extraction [88].

the azimuthal modulations between mid-rapidity and forward pseudorapidity regions, and a strong transverse momentum dependence observed in the particle v_2. Yet on average this functional form for a fixed v_2 over all transverse momentum remains a good approximation.

The progressive implementation of updates to the constituent subtraction at CMS is shown in Figure 6-9. The leftmost plot shows the original implementation of constituent subtraction, where underlying event is estimated from median unsubtracted k_{T} jet. The relevant structures in the plot are in forward pseudorapidity, where there is a marked increase in the magnitude of the underlying event as the estimator fails. The second structure in the subtracted UE is in the azimuthal periodic fluctuation, coming from the long range correlations produced in nuclear collisions. In the middle plot, the k_{T} estimation of underlying event is replaced with the iterative pedestal method. While there is still some forward uptick in the average ρ of the subtracted event, there is clear improvement. However, the azimuthal structure remains as iterative pedestal does not on its own correct for flow. Finally, the rightmost plot adds the

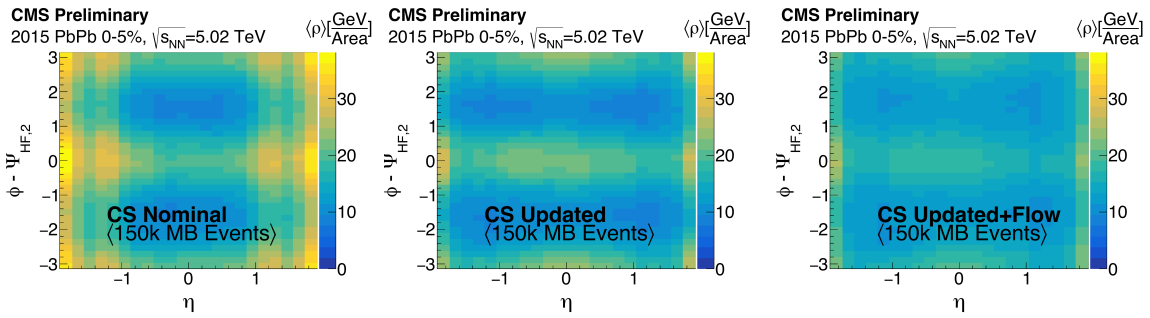

Figure 6-9: Left: Average density of underlying event in coordinates of detector η and azimuthal distance from event plane after applying nominal CS subtraction in central 0-5% PbPb events. This subtraction is employed in [52, 70]. Middle: Average density of underlying event relative in coordinates of detector η and azimuthal distance from event plane after applying updated CS subtraction in the same set of central 0-5% PbPb events. The resulting distribution is more uniform in detector η, as the PU-style estimator accounts for changing detector geometry. Right: Average density of underlying event relative in coordinates of detector η and azimuthal distance from event plane after applying updated CS subtraction and flow modulation in ϕ, in the same set of central 0-5% PbPb events. Azimuthal differences in the subtracted event are reduced relative to the position of the event plane [88].

modulation as fitted in Figure 6-8, and the periodic structure in the subtracted event decreases. The progression can be summarized as $\rho(\eta_{coarse}) \rightarrow \rho(\eta_{fine}) \rightarrow \rho(\eta_{fine}, \phi)$.

Figure 6-10 shows the average underlying event in an η-ϕ plot before and after the fully implemented $\rho(\eta_{fine}, \phi)$ map in two centrality selections. Perhaps surprisingly, the relative magnitude of structure induced by flow is greater in the semi-central selection. This is because elliptical flow effects are actually stronger in semi-central selections even as the magnitude of Poisson fluctuations decreases. Thus while the additional modulation in the underlying event in azimuth improves resolution in all centrality, it actually drives down the semi-central N term in relative resolution more than in central-most.

Impact of azimuthal modulations before and after new subtraction method is also shown in projections of the ρ maps, as shown in Figure 6-11. In central and semi-central events there is a significant flattening of the event average shape after the addition of modulation. In peripheral events the impact of modulation correction is negligible. Required minimum multiplicities and convergent fit criteria explain the

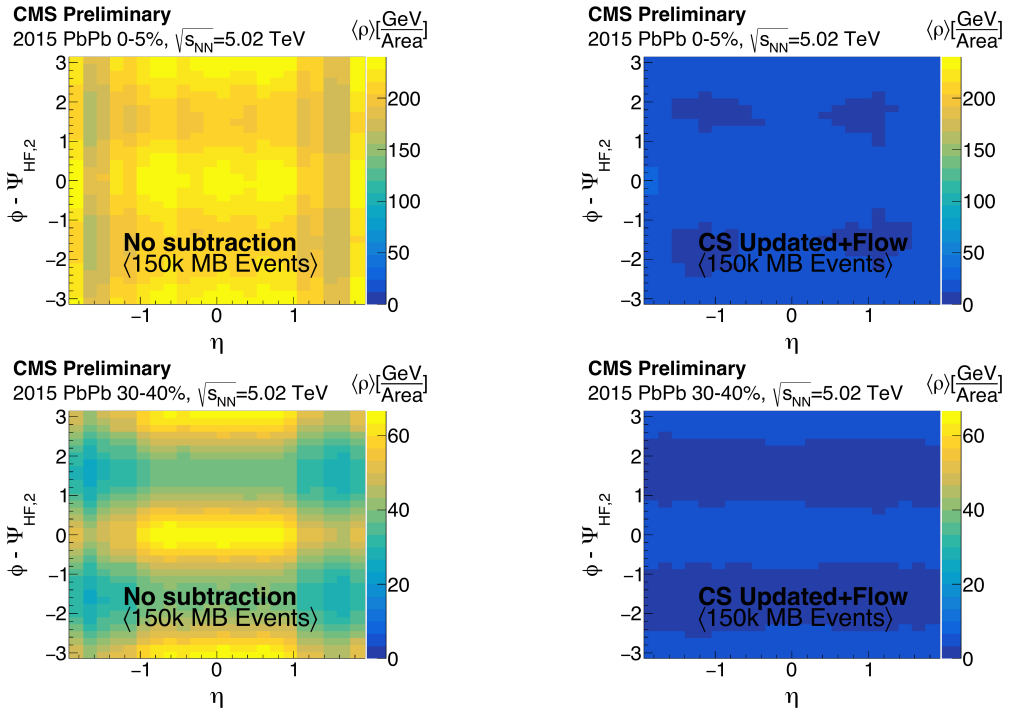

Figure 6-10: Left: Average density of underlying event in coordinates of detector η and azimuthal distance from event plane before subtraction for central 0-5% events (top) and semi-peripheral 30-40% events (bottom). Right: Average density of underlying event relative in coordinates of detector η and azimuthal distance from event plane after subtraction [88].

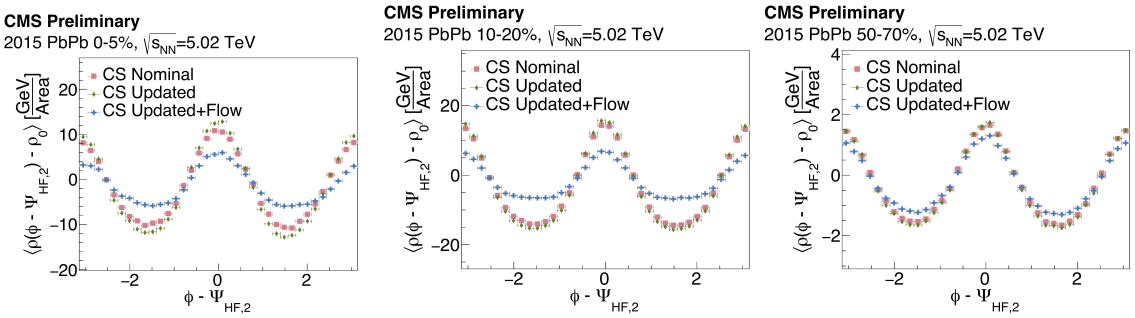

Figure 6-11: Left: Projection of underlying event density onto distance of jet azimuthal angle and event plane for three subtractions in an average of central 0-5% PbPb events: nominal CS (orange squares), CS with updated ρ estimator (green diamonds), and CS with updated ρ estimator and flow modulation (blue crosses). Middle: The corresponding projection in a semi-central 10-20% PbPb event average. Right: The corresponding projection in a peripheral 50-70% PbPb event average. The three subtractors converge as the flow correction is turned off when particle multiplicities fall below levels for reasonable single-event extraction [88].

peripheral behavior, and given the peripheral resolution is already well controlled the remaining modulation is acceptable for physics analysis.

Random cones are a standard data-driven technique for determining the effectiveness of ρ maps to be employed in underlying event subtraction. A random position in η-ϕ is selected and the difference between the sum of constituents in a defined $\Delta\eta$-$\Delta\phi$ cone around the point is taken with the value given by the ρ estimator. Binned in centrality, differences in mean of this distribution between data and Monte Carlo correspond to non-closures resulting from differences between data and simulation, while the difference in the width translates to a data-driven scale factor for correcting the N term in CSN parametrization of jet energy resolution. Figure 6-12 is a study of random cones in data and Monte Carlo with the updated constituent subtraction.

Finally, the jet energy scale and jet energy resolution is evaluated at jet level for the fully implemented update to constituent subtractor. In addition to the usual cone size used in splitting function and groomed jet mass measurements, a larger radius of R=0.8 is shown for the first time in heavy ion collisions. The large radius becomes viable primarily because of the increased kinematic reach of latest PbPb data-takings, where jets are approaching energy of 1 TeV. Figure 6-13 shows closures of the jet

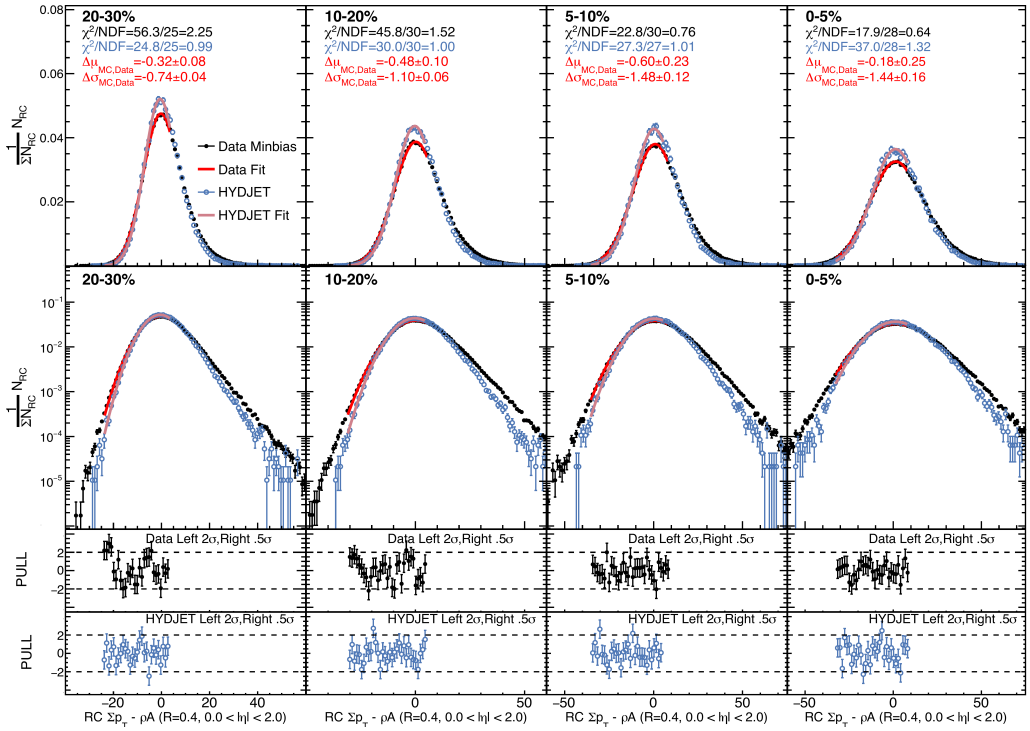

Figure 6-12: Random cone results using updated subtractor. From left to right, in centrality bins of 20-30%, 10-20%, 5-10% and 0-5%. Random cones are shown for PbPb data (black points), and HYDJET (blue points). Distributions are fitted with truncated left-hand-side Gaussians. Second set of panels from top are re-plotted on a log-y scale. Pull distributions for fits are shown in the bottom panels [88].

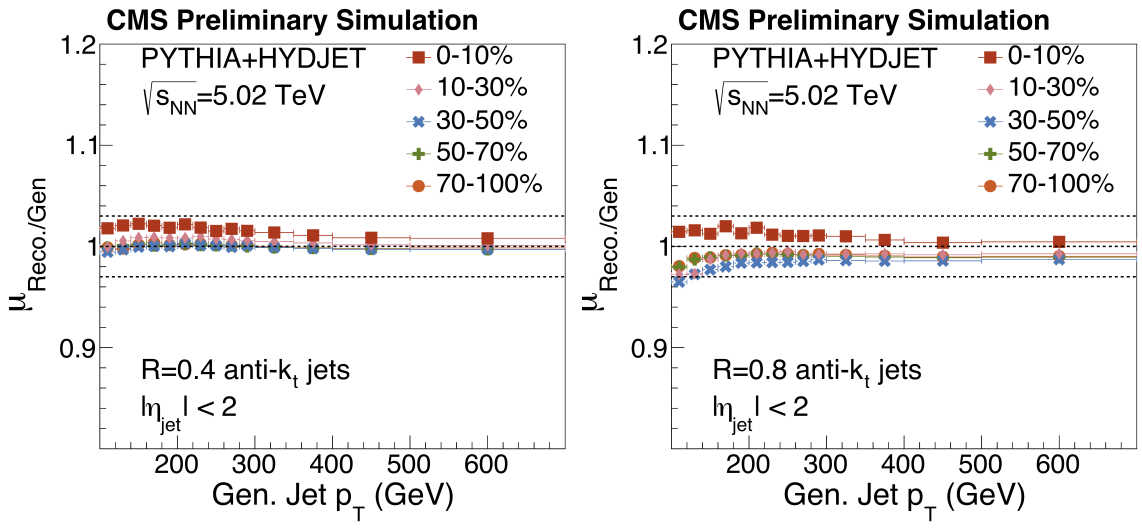

Figure 6-13: Left: Jet energy scale closure as a function of centrality and p_{T} for jets of radius parameter R=0.4. Closure is globally within 2% for all centrality. Right: Jet energy scale closure as a function of centrality and p_{T} for jets of radius parameter R=0.8. Non-closures are generally slightly greater than for corresponding R=0.4 jets. This can be interpreted as greater difficulty in avoiding self-subtraction with a larger jet cone. Jet Energy Corrections are derived on unsubtracted jets in zero pileup PYTHIA run thru Heavy-Ions reconstruction, applied globally to all centralities [88].

energy scale in PYTHIA+HYDJET Monte Carlo for a selection of jet energy scales out to pseudorapidity of $\pm$ 2. Since identical jet energy corrections are applied to all centralities, the resulting variations in the closure are purely result of imperfections in subtraction. Jets clustered with resolution parameter R=0.4 show good global scale closure for all p_{T} and centrality, with largest non-closure coming from central-most events, with a rough 1-2% non-closure. This indicates undersubtraction.

The right hand side of Figure 6-13 shows scale closure for jets reconstructed with resolution parameter R=0.8, the first such reconstruction in heavy ion collisions, intended for use in studying the radial redistribution of jet energy interacting with QGP. There is additional non-closure in peripheral events when compared with 0.4 radius jets, which indicates that the larger cone is oversubtracted as some of the jet energy is not fully excluded from the ρ estimation. Percent level non-closures correspond to roughly 10% changes in spectra, so more careful study of these over and undersubtraction effects will be essential to improving future measurement precision.

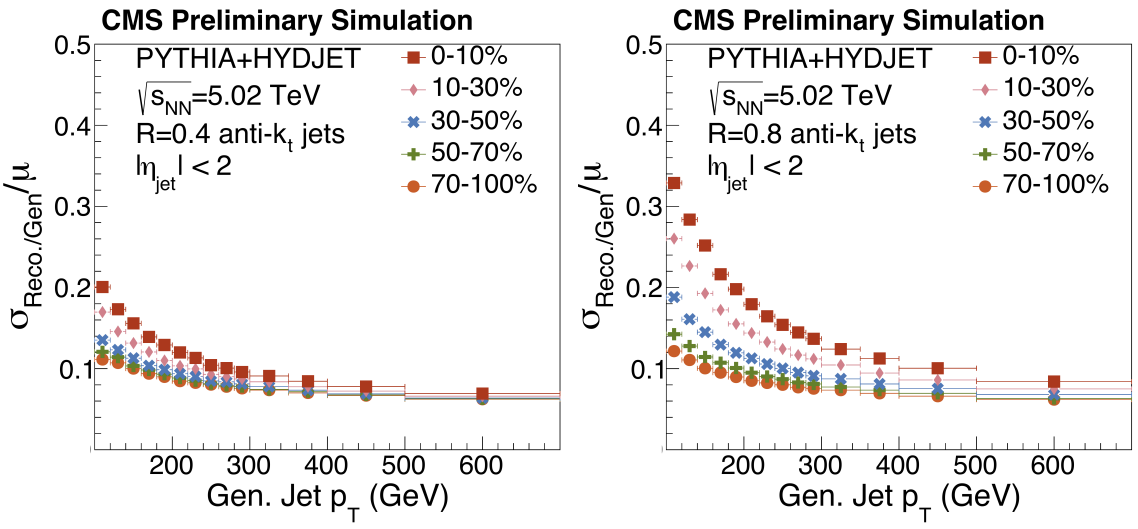

Figure 6-14: Left: Jet energy resolution as a function of centrality and p_{T} for jets of radius parameter R=0.4. Right: Jet energy resolution as a function of centrality and p_{T} for jets of radius parameter R=0.8. Increased resolution of larger cone is driven by greater contribution from underlying event fluctuations [88].

Figure 6-14 shows the corresponding jet energy resolutions for R=0.4 and R=0.8 jets binned in p_{T} and centrality for jets of pseudorapidity out to $\pm$ 2. The R=0.8 relative jet energy resolution is roughly 18% at 200 GeV,

Figure 6-15 shows event plane dependence of the jet energy scale closure with and without the correction for underlying event azimuthal modulations. While there is still some scale dependence with position of jet relative to event plane, the dependence is reduced with the introduction of underlying event modulation.

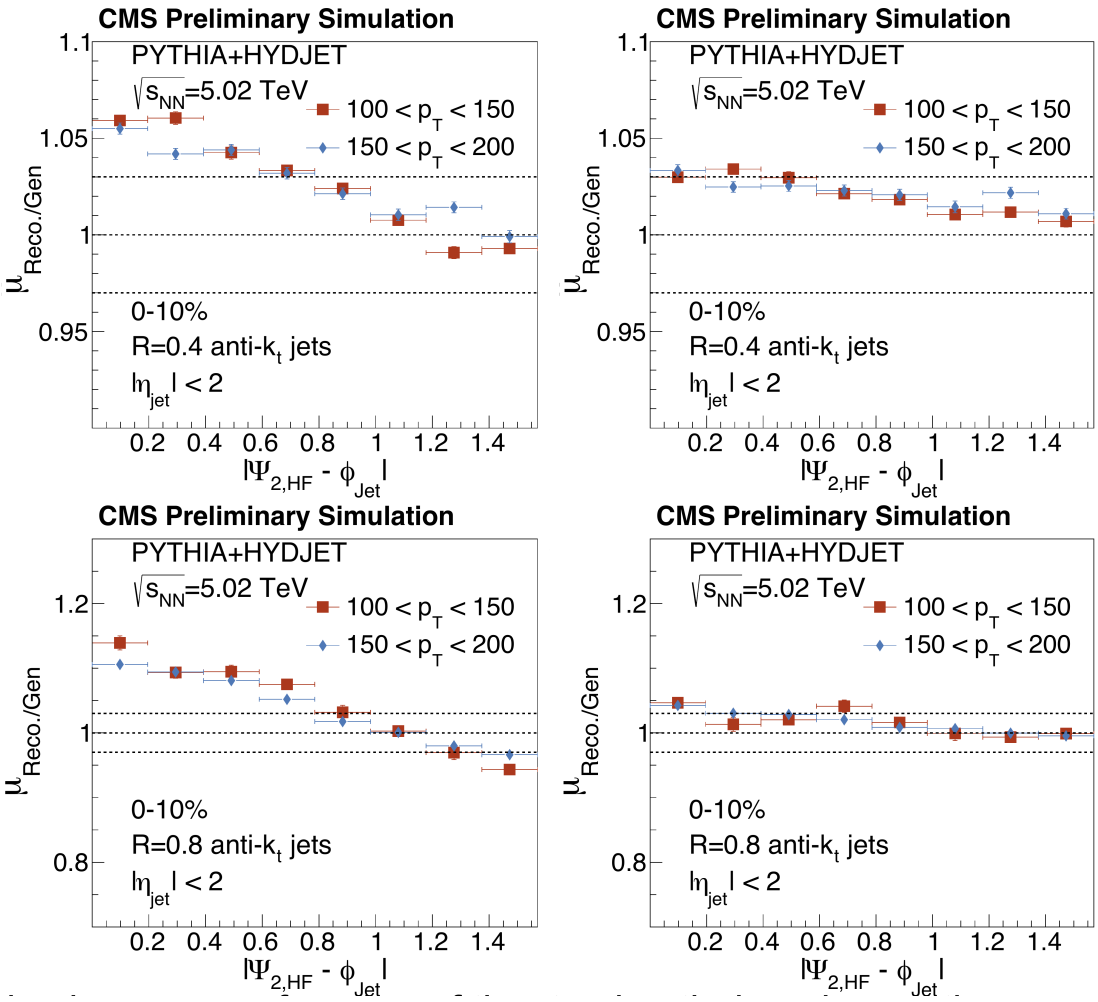

Figure 6-15: Left: Jet energy scale closure as a function of the distance between jet azimuthal angle and the event plane $\Psi_{2,HF}$, for jets subtracted without flow modulation. The top panel is for jet radius of R=0.4, the bottom panel is for jet radius of R=0.8. Right: Jet energy scale closure as a function of the distance between jet azimuthal angle and the event plane $\Psi_{2,HF}$, for jets subtracted with flow modulation. The closure improves relative to left-hand-side counterpart, significantly so for large cone [88].

6.3.1 Alternative Subtraction Methods

All methods discussed so far, minus HF/Voronoi technique, suffer from a shared flaw: the in-event estimation of underlying event means signal can always contaminate underlying event estimation, especially in the case of heavy ions where strong modification of the signal is observed. While a number strategies are employed to mitigate this contamination (exclusion of jetty regions from the calculation of ρ, using medians over means, etc.), strategies can only ever minimize this bias, and never guarentee exclusion. Therefore, the most obvious improvement to be made on this subtraction technique is to reincorporate parts of HF/Voronoi technique [92] in constructing ρ maps. Specifically, the ρ map should be constructed based on a set of global observables that are relatively independent of jets. An ensemble of minimum bias events binned in these global observables would define a given map, and all jets in events matching this set of global observables would be subtracted (likely with constituent subtraction method) but employing a map constructed from independent events. Only with the construction of independent ensemble maps for ρ can the potential of signal to bias its own subtraction be fully excluded.

In the HF/Voronoi technique, the set of global observables was defined by the distribution of energy in the HF. Figure 6-16 shows one such example from [92]. While this choice could account for many underlying substructures of the soft particle production, the likely dominant set is magnitude, elliptical and triangular flow. This is also observed in machine-learning driven subtractions such as PUMML [97], where the introduction of pileup vertex information was actually only employed in calibration of the subtractor, and not for any trajectory matched removals. A proof of concept implementation of an HF/Voronoi style subtraction map should use global observables centrality, Ψ_2, Ψ_3, and consider incorporating v_2, v_3. The magnitudes of the flow Fourier components are of less interest given the known strong p_{T} dependence and the large range of momentum scales a jets constituents range. The relative magnitude, if observed to be more p_{T} independent, might viable. Higher order harmonics are also of interest, but current ATLAS subtractions as employed in jet production cross sections

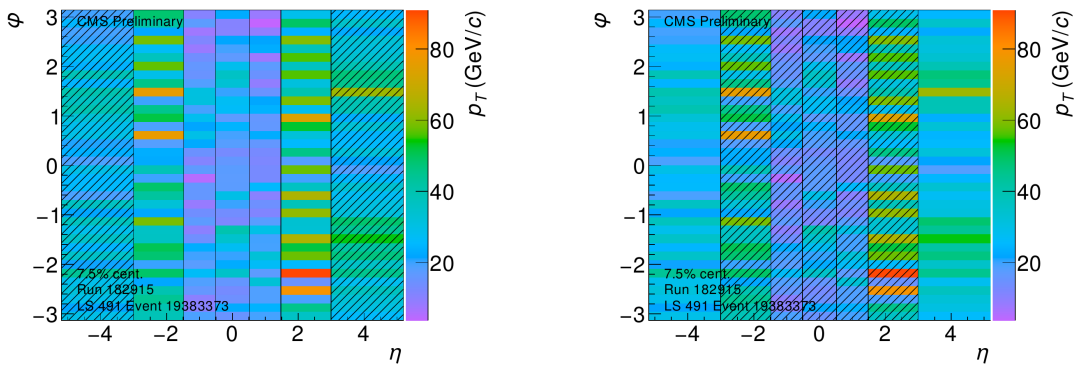

Figure 6-16: Example of HF/Voronoi map of underlying event in the CMS detector. The full forward region of the HF is split into 36 regions on either side in ϕ, defined by tower width. The distribution of UE in HF is then mapped to five distinct η regions at mid-pseudorapidity in a comparable ϕ binning. This techniques minimizes jetty contamination of UE estimation from the mid-rapidity regions jet production, while also accounting for flow modulation. The η binning acts to account for changing detector geometry. Via [92].

at $\sqrt{s_{NN}}$=5.02 TeV suggests that the impact of the fourth harmonic is relatively small compared to second and third [55].

Finally, a very careful consideration is necessary of what should be incorporated into the jet reconstruction at all. In hypothetical situation where it is known that all jets result in final state particles greater than 1 GeV, the incorporation of particles below 1 GeV in the reconstruction would artificially increase fluctuations from noise. In reality the jet final state exists at effectively all scales, but a cutoff might be reasonably defined for some fraction of the partons total energy. This would be similar to exploiting vertex information for the removal of pileup in proton-proton collisions, although with greater potential for bias.

Table 6.1: CMS jet analysis in PbPb by jet constituent reconstruction, recombination algorithm, and subtraction method. This table shows there has been a healthy mix of calorimeter vs. particle flow jets, anti-k_{T} vs. Cambridge/Aachen (CA) vs. Iterative Cone (IC) clusterings, and iterative pedestal (PU) vs. constituent subtraction (CS).

Analysis	$\sqrt{s_{_{NN}}}$ (TeV)	Calo. or PF	Algorithm	Subtraction	Reference
1st A_JMissing p_{T}	2.76	Calo.	IC	PU	[24]
p_{T} Dependent A_J	2.76	PF	anti-k_{T}	PU	[25]
Photon+jets	2.76	PF	anti-k_{T}	PU	[66]
1st Jet Frag. Func.	2.76	PF	anti-k_{T}	PU	[63]
Jet Shapes	2.76	PF	anti-k_{T}	PU	[27]
b-jet R_{AA}	2.76	PF	anti-k_{T}	PU	[64]
2nd Jet Frag. Func.	2.76	PF	anti-k_{T}	PU	[26]
2nd. Missing p_{T}	2.76	Calo.	anti-k_{T}	HF/Voronoi	[28]
Jet+track Corr.	2.76	Calo	anti-k_{T}	PU	[29]
Jet+track Balance	2.76	Calo	anti-k_{T}	PU	[30]
Jet R_{AA}	2.76	PF	anti-k_{T}	PU	[31]
Z+jets	5.02	PF	anti-k_{T}	PU	[50]
Jet z_G	5.02	PF	anti-k_{T},CA	CS	[52]
Photon+jets	5.02	PF	anti-k_{T}	PU	[67]
Photon+jets Frag. Func.	5.02	PF	anti-k_{T}	PU	[68]
b-jet A_J	5.02	PF	anti-k_{T}	PU	[65]
Jet+track Balance	5.02	Calo.	anti-k_{T}	PU	[48]
Jet Mass	5.02	PF	anti-k_{T},CA	CS	[70]
Photon+jets Shapes	5.02	PF	anti-k_{T}	PU	[69]
Large R Jet R_{AA}	5.02	PF	anti-k_{T}	CS-PU Hybrid	This document

Chapter 7

Analysis

The following two analysis share jet objects and detector, but in different run periods and for different center of mass energies. The overall focus is quantifying observed jet energy loss by measuring in a systematic way how that energy is redistributed throughout the event.

7.1 Missing p_{T}

The following section is based on data published in [28].

With the first observations of dijet asymmetry at the start of the LHC program in 2010, there was an immediate effort to quantify how the lost energy within the jet cone was redistributed throughout the event [24, 23]. Looking at the projection of track p_{T} onto the axis of the leading jet in the event gave early hints early on that energy was recoverable if going beyond the jet cone. However, these early studies were limited by sample size in PbPb, and completely lacking proton-proton vacuum reference. This analysis is a followup with factor fifteen increase in PbPb statistics, inclusion of appropriate reference, and a stronger focus on the angular distribution of the event energy relative the dijet pair. In addition, different jet populations are selected by varying jet R from 0.2 through 0.5 in increments of 0.1, to look at how the transverse p_{T} is distributed relative narrower or broader jets. Note the entire next section is primarily based on [28].

7.1.1 Analysis Samples and Observables

Missing p_{T} measurement is made with pp and PbPb data taken at $\sqrt{s_{_{NN}}}$=2.76 TeV. The PbPb sample corresponds to an integrated luminosity of 166 $\mu\mathrm{b}^{-1}$, while pp data corresponds to integrated luminosity of 5.3 pb^{-1}. Events are selected according the following global criteria

1. Fires inclusive single jet trigger of transverse p_{T} greater than 80 GeV
2. Hadronic collision event selection criteria [66]
    - At least one reconstructed vertex
    - Primary vertex of $|z| < 15$ cm
    - Total HF energy $<$ 5500 GeV (Exclude obvious pileup events)
    - 3 towers in HF_{+} and HF_{-} each with minimum energy of 3 GeV.
    - Veto on beam halo events using timing of BSC $\pm$ z signals.
    - Veto on HCal noise for purity of jet sample

After filtering on these global selections, dijet selections are applied on reconstructed calorimeter jets, which are employed in this analysis to avoid biases from auto-correlations observed between tracks and particle flow jets. A leading calorimeter jet with transverse p_{T} in excess of 120 GeV is required, along with subleading jet in excess of 50 GeV. Results will be shown for jets clustered with resolution parameter R=0.2, 0.3, 0.4, and 0.5. In each case, this selection is applied separately. This selection criteria matches that of previous missing p_{T} and dijet asymmetry analysis at CMS [24]. Both jets are required to be within $|\eta| <$2. A dijet configuration is imposed by requiring the leading and subleading jet be relatively back-to-back in azimuth, with $\Delta\phi_{1,2} > 5\pi/6$. After restricting to the set of events with leading and subleading jets satisfying these requirements, events where one of the two jets in window $1.6 < |\eta| < 2.0$ are rejected. This additional cut is employed to keep the extended radius of each dijet 0.8 units in η from the edge of the tracker acceptance of $\pm$ 2.4. This is also done after finding leading and subleading jets in the larger acceptance

(rather than restricting initial jet selection to $|\eta| < 1.6$) so that subleading or third jets are not mistaken for leading. Note that for results looking very far from the dijet axis, a further pseudorapidity restriction will be imposed of $|\eta_{1,2}| < 0.5$.

After this set of selections is applied, the dijet axis is defined relative to the dijet system. The axis,

$$\phi_{Dijet} = \phi_1 + (\phi_2 + \pi)/2 \tag{7.1}$$

is the average of the leading jet axis and the flipped subleading axis, accounting for wraparound in azimuth. The choice is made such that the projection of tracks is made on an axis that is symmetric with respect to the centroid of leading and subleading jet. This is in contrast with original analysis of missing p_{T}, where the leading jet axis was chosen for projection. The new choice reflects the focus on angular distribution of energy. When binning missing p_{T} in Δ,

$$\Delta = \sqrt{(\phi_{\mathrm{trk}} - \phi_{\mathrm{Jet}})^2 + (\eta_{\mathrm{trk}} - \eta_{\mathrm{Jet}})^2} \tag{7.2}$$

around leading jet axis, there is a non-closure that can be observed in a generator level Monte Carlo with embedded signal such as PYTHIA+HYDJET, where there are no quenching physics effects. However, switching from leading jet axis to dijet axis removes the non-closure, and any non-closure observed in data is attributable to quenching physics. Figure 7-1 demonstrates the effect in a pure background HYDJET projection, with leading and subleading jet derived from the embedded PYTHIA.

As we are working with track for final state hadrons, we must correct for tracking inefficiency and fake rate. Tracking efficiency is observed to range from 80 to 90% from 0.5 GeV to 10 GeV. The corresponding fake track reconstruction rate is roughly 2% globally. Secondary particles can also contribute up to 2%, but multiple reconstruction is sub percent. In PbPb collisions, the corresponding efficiency ranges from 30 to 70% from 0.5 to 10 GeV, and corresponding fake rate is 35% at 0.5 GeV to sub-2% by 1 GeV. However, secondary particle and multiple reconstructions are both fully negligible. Correction tables are derived based on Monte Carlo closures for factorized efficiency and fake rate (and in pp additional secondary particle and multiple

reconstruction tables). These tables are binned in particle p_{T}, η, ϕ and nearest angle to nearest jet axis above 50 GeV (a local density proxy). PbPb tables are also binned in centrality to account for changing density of particles. Each track going into sum or multiplicity gets weight according to its factorized correction factor, as

$$\mathrm{c}^{\mathrm{trk}} = \frac{(1 - \text{misreconstruction}) \times (1 - \text{secondary-particle})}{(\text{efficiency}) \times (1 + \text{multiple-reconstruction})}. \tag{7.3}$$

All observables are defined with respect to dijet axis. Hemispheres are defined by leading and subleading sides of the jet axis. Multiplicities of particles in each hemisphere calculated in bins of p_{T} and subtracted from each other to quantify produced excess. Observable

$$\Delta_{\mathrm{mult}} = N_{\mathrm{Trk}}^{\mathrm{Corrected}}|_{\Delta\phi_{\mathrm{Trk,dijet}}>\pi/2} - N_{\mathrm{Trk}}^{\mathrm{Corrected}}|_{\Delta\phi_{\mathrm{Trk,dijet}}<\pi/2}, \tag{7.4}$$

is for this difference with incorporated tracking corrections of Eq. 7.3. The observable reduces the energy redistribution to soft or hard particle components, with only angular information being hemisphere in which particle is found. For a full p_{T} imbalance and the incorporation of angular information, track corrections are introduced to projection sum as

$$p_{\mathrm{T}}^{\parallel} = -\mathrm{c}^{\mathrm{trk}} p_{\mathrm{T}}^{\mathrm{trk}} \cos\left(\phi_{\mathrm{trk}} - \phi_{\mathrm{dijet}}\right) \tag{7.5}$$

where $\mathrm{c}^{\mathrm{trk}}$ is as described in Eq. 7.3, ϕ_{dijet} is the dijet axis, and the overall negative sign defines leading jet hemisphere contribution as negative, and subleading jet hemisphere contributions as positive.

With this in mind, define the global missing p_{T} as

$$\langle \not{p}_{\mathrm{T}}^{\parallel} \rangle_{p_{\mathrm{T}}^{\mathrm{trk}}} = \sum_{\Delta} \langle \not{p}_{\mathrm{T}}^{\parallel} \rangle_{p_{\mathrm{T}}^{\mathrm{trk}},\Delta}, \tag{7.6}$$

or a sum over the full leading and subleading jet hemispheres, binned in track momentum. This is represented as sum over Δ, which is how tracks are binned in angle with respect to closest of leading or subleading jet, here ϕ_{Jet}. Note that this is specifically

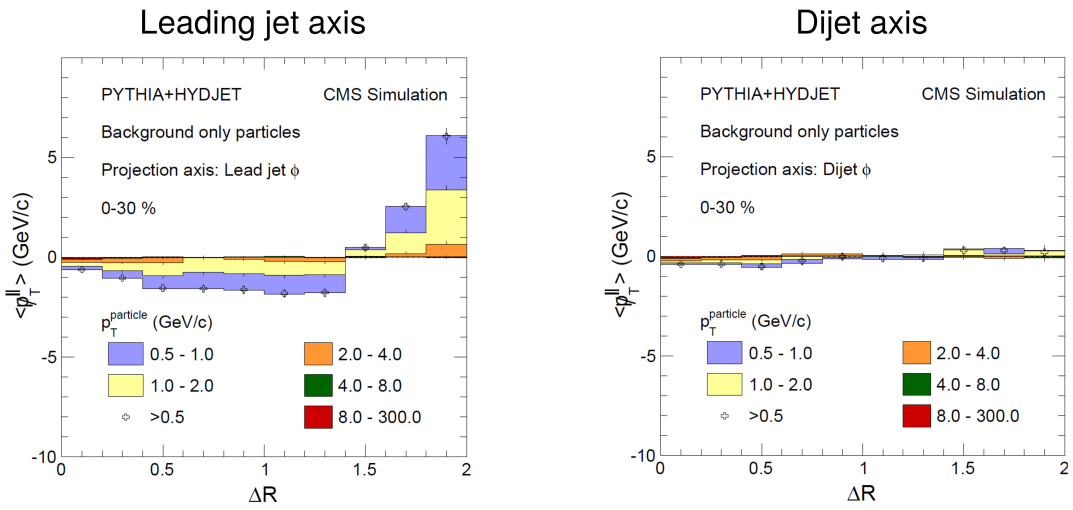

Figure 7-1: Left: Missing p_{T} projection as binned in Δ using the leading jet axis as defined by embedded PYTHIA, but projecting only generator particles coming from the uncorrelated HYDJET background. The induced structure comes purely from the choice of axis and definition of the projection. Right: Missing momentum projection as binned in Δ now using the dijet axis as defined by embedded PYTHIA. The previously observed structure from uncorrelated background particles is gone and there is good closure compared to physics effects.

not with respect to dijet axis. Dijet axis only defines the projection, and symmetrizes track projections relative to leading and subleading jet positions.

Since the sum over Δ is binned in p_{T}, closure is not expected. Even in pp, jet fragmentation differs enough between leading and subleading jet to expect different contributions to the overall momentum balance on average. To achieve true momentum balance, p_{T} binning must be collapsed. This observable is

$$\langle \not{p}_{\mathrm{T}}^{\parallel} \rangle_{\Sigma} = \sum_{p_{\mathrm{T}}^{\mathrm{trk}}} \langle \not{p}_{\mathrm{T}}^{\parallel} \rangle_{p_{\mathrm{T}}^{\mathrm{trk}}}, \tag{7.7}$$

and while full momentum balance is still not achieved because some fraction leaves tracker pseudorapidity acceptance of $\pm$ 2.4 or falls below the reconstructable track p_{T} threshold of 0.5 GeV, the remaining non-closure is small and fully replicated in generator level PYTHIA.

Finally, for study of angular distribution of missing momentum, define

$$\langle \not{p}_{\mathrm{T}}^{\parallel} \rangle_{\Delta} = \sum_{p_{\mathrm{T}}^{\mathrm{trk}}} \langle \not{p}_{\mathrm{T}}^{\parallel} \rangle_{p_{\mathrm{T}}^{\mathrm{trk}},\Delta} \tag{7.8}$$

or the sum of track momentum projected onto dijet axis and found in a chosen annulus Δ with respect to the closer of either leading or subleading jet, binned in track transverse momentum to extract contributions from soft and hard components. To study the full momentum balance per annulus, cumulative sum over Δ is also plotted, defined as

$$\langle \not{p}_{\mathrm{T}}^{\parallel} \rangle_{[0,\Delta]} = \sum_{\Delta'=0}^{\Delta'=\Delta} \langle \not{p}_{\mathrm{T}}^{\parallel} \rangle_{\Delta'}. \tag{7.9}$$

The cumulative sum over annuli shows for a fixed population of asymmetric dijets in pp and PbPb collisions the point at which full (or close to full) momentum balance is achieved.

7.1.2 Analysis Systematics

The systematics of missing momentum studies of jet energy redistribution are summarized in Tables 7.1, 7.2, and 7.3, for the observables described in the previous section. The dominant contributions tend to come from uncertainty in tracking efficiency and fake rate corrections, and uncertainty on corrections for jet energy response.

Jet energy response uncertainty has a two-fold effect. The first effect deals directly with what population of jets passes cut thresholds of leading and subleading jets. Depending on the scale uncertainty, this change to population can actually be quite sizable, as the steeply falling jet spectrum means must of the jets are just above or below the cut boundary. Uncertainty in the jet energy scale was first taken as differences in the parton flavor of the jets, or a 5% response difference for light quark and gluon jets at 50 GeV and decreasing as p_{T} increased. While a fragmentation dependent correction is applied to reduce the bias of quark-gluon fragmentation on response (in a sense mimicking what particle flow does in calorimeter jets), the remaining full difference is used as uncertainty as both flavor of jets is a-priori unknown

in PbPb and medium effects may introduce additional bias towards one population of jets. Additional scale uncertainty is taken for data-MC differences of 2% level by studying dijet imbalance in proton-proton collisions of adjacent run period and validating in peripheral sample of PbPb events. Finally, since there are known fragmentation differences between jets in Monte Carlo and in data, the impact of this difference on the fragmentation dependent corrections is taken as uncertainty.

The set of uncertainties above are on the jet energy scale. To propagate them to the observables, jet energy was varied independently in leading and subleading jets, and analysis was run over each new population passing selection cuts. The difference in central value for each population was taken as systematic and is listed in systematics tables as Jet Reconstruction, Data/MC differences for JES, and Fragmentation dependent JES.

The second effect error on scale can have is swapping effects, where either leading and subleading jets are reconstructed in opposite order, or a third jet supplants the true subleading jet. This are ultimately the effect of resolution on jet populations, and a bin-by-bin correction is applied to account for these swappings. Error on this bin-by-bin correction is also incorporated into the systematic jet reconstruction on the tables.

Potential errors from jet angular resolution was tested, but as the one sigma width of jet angular resolution even at the lowest jet momentum is less than half of the Δ bin width, the resulting non-closures were effectively negligible.

In addition to jet uncertainties, there are two sets of tracking uncertainties accounting for uncertainty in the correction tables and for potential differences between data and Monte Carlo. Tracking tables were derived in a set of Monte Carlo events, and the performance was then evaluated in a statistically independent set of Monte Carlo events. Generator level particles are compared to the set of tracks after correction tables are applied. The remaining statistically significant non-closures define the precision of the corrections and are ascribed as uncertainty. Uncertainty from differences between data and Monte Carlo are taken from the heavy ion tracking POG uncertainty on global efficiency curve, and is on the order of 5%. Correction tables

Table 7.1: Systematic uncertainties in $\langle \not{p}_{\mathrm{T}}{}^{\parallel} \rangle_{\Delta}$ for jets clustered with distance parameter of 0.3 in pp, and in central and peripheral PbPb collisions, for different $A_J$selections. Uncertainties are shown as shifts in the values in units of GeV (rather than as fractions) for two Δ selections.

	Inclusive A_J					
	pp		30-100% PbPb		0-30% PbPb	
Δ	< 0.2	0.2–2.0	< 0.2	0.2–2.0	< 0.2	0.2–2.0
Jet reconstruction	< 1	0.0–0.2	1	0.1–0.2	1	0.1–0.4
Data/MC differences for JES	1	0.1–0.2	2	0.1–0.3	2	0.1–0.3
Fragmentation dependent JES	< 1	0.1–0.2	2	0.1–0.2	1	0.1–0.4
Track corrections	< 1	< 0.1	1	0.0–0.2	2	0.2–0.9
Data/MC differences for tracking	1	0.0–0.1	1	0.1–0.2	1	0.1–0.2
Total	1	0.1–0.3	2	0.2–0.3	3	0.2–1.0
	$A_J < 0.22$					
	pp		30-100% PbPb		0-30% PbPb	
Δ	< 0.2	0.2–2.0	< 0.2	0.2–2.0	< 0.2	0.2–2.0
Jet reconstruction	< 1	0.1–0.2	1	0.1–0.2	1	0.1–0.4
Data/MC differences for JES	1	0.1–0.2	2	0.1–0.4	2	0.2–0.4
Fragmentation dependent JES	< 1	0.1	2	0.1–0.4	1	0.1–0.5
Track corrections	< 1	< 0.1	1	0.1	2	0.1–0.6
Data/MC differences for tracking	< 1	0.0–0.1	1	0.1	1	0.1
Total	1	0.1–0.3	2	0.2–0.4	3	0.2–0.6
	$A_J > 0.22$					
	pp		30-100% PbPb		0-30% PbPb	
Δ	< 0.2	0.2–2.0	< 0.2	0.2–2.0	< 0.2	0.2–2.0
Jet reconstruction	2	0.1–0.5	1	0.1–0.6	2	0.2–0.6
Data/MC differences for JES	2	0.1–0.3	3	0.2–0.5	3	0.3–0.6
Fragmentation dependent JES	1	0.1–0.5	1	0.1–0.7	1	0.2–0.6
Track corrections	< 1	0.1	1	0.1–0.3	3	0.2–1.1
Data/MC differences for tracking	2	0.1–0.2	2	0.1–0.2	2	0.1–0.3
Total	3	0.3–0.8	3	0.3–0.9	4	0.4–1.4

are modified by this value, propagated through entire analysis chain, and difference with central values taken as uncertainty on observables. Total uncertainty from these and the jet sources is taken by quadrature sum.

Table 7.2: Systematic uncertainties in $\langle \not{p}_{\mathrm{T}}^{\parallel} \rangle_{p_{\mathrm{T}}^{\mathrm{trk}},\Delta}$ in 0–30% PbPb collisions, for jets clustered with a distance parameter of 0.3, as a function of charged-particle p_{T}. Uncertainties are shown as shifts in the values in units of GeV (rather than as fractions) for two Δ selections.

	$0.5 < p_T < 2$ GeV		$2 < p_T < 8$ GeV		$p_T > 8$ GeV	
Δ	< 0.2	0.2–2.0	< 0.2	0.2–2.0	< 0.2	0.2–2.0
Jet reconstruction	0.04	0.06–0.25	0.13	0.04–0.14	0.85	0.01–0.07
Data/MC differences for JES	0.14	0.07–0.24	0.42	0.03–0.11	0.97	0.01–0.12
Fragmentation dependent JES	0.03	0.10–0.14	1.1	0.05–0.23	0.19	0.02–0.06
Track corrections	0.09	0.08–0.64	0.27	0.06–0.13	1.78	0.01–0.07
Data/MC differences for tracking	0.04	0.03–0.08	1.2	0.01–0.05	1.16	0.00–0.02
Total	0.17	0.20–0.69	1.1	0.11–0.29	2.3	0.04–0.10

Table 7.3: Systematic uncertainties in $\langle \not{p}_{\mathrm{T}}^{\parallel} \rangle_{p_{\mathrm{T}}^{\mathrm{trk}},\Delta}$ in 0–30% PbPb collisions are shown for jets clustered with distance parameters of 0.2, 0.4 and 0.5. Uncertainties are shown as shifts in the values in units of GeV (rather than as fractions) for two Δ selections.

	$R = 0.2$		$R = 0.4$		$R = 0.5$	
Δ	< 0.2	0.2–2.0	< 0.2	0.2–2.0	< 0.2	0.2–2.0
Jet reconstruction	1	0.1–0.4	1	0.1–0.5	1	0.1–0.7
Data/MC differences for JES	2	0.1–0.5	2	0.1–0.4	2	0.1–0.3
Fragmentation dependent JES	1	0.1–0.4	1	0.1–0.3	1	0.1–0.3
Track corrections	2	0.2–0.7	2	0.1–1.1	2	0.1–1.1
Data/MC differences for tracking	1	0.1–0.2	1	0.1	1	0.1
Total	3	0.2–0.9	3	0.3–1.1	3	0.2–1.1

7.2 Radial Scan of Jet R_{AA}

Jet production cross sections were previously measured for $\sqrt{s_{NN}}$=2.76 TeV collisions of PbPb and pp vacuum reference by CMS, ATLAS and ALICE [31, 37, 34]. Furthermore, measurements now exist of jet suppression at $\sqrt{s_{NN}}$=5.02 TeV in PbPb [55]. The observed suppression is modest in peripheral most collisions, with increasing magnitude as centrality goes to central-most, settling on suppression of roughly factor 2. More surprisingly, at 200 GeV the suppression appears to flatten out at 0.6. This leads to the question - at what point are jets fully recovered in momentum space? At what point is jet energy fully recovered in angular space? While missing p_{T} studies

seek to answer the latter question and has led to genuine insight in the incorporation of medium effects on observables, it has proved difficult for theoretical comparison. In contrast, not only is a radial scan of jet suppression fully calculable for all available models, a host of predictions already exist, and predictions significantly diverge in behavior. Thus a radial scan or R_{AA} to largest possible cone sizes is a priority for heavy ion physics programs. It has recently become possible with greatly reduced systematics of 2015 data-taking, with shared detector conditions for pp and PbPb, and new kinematic reach of higher $\sqrt{s_{_{NN}}}$ and integrated luminosity.

7.2.1 Analysis Samples and Observables

Radial scan of jet production cross section is made with pp and PbPb data taken at $\sqrt{s_{_{NN}}}$=5.02 TeV. The PbPb data sample corresponds to integrated luminosity of 404 $\mu\mathrm{b}^{-1}$ and the pp sample corresponds to integrated luminosity of 27.4 pb^{-1}. Global event selection is very similar to that made at $\sqrt{s_{_{NN}}}$=2.76 TeV [28, 54].

1. Fires inclusive single jet trigger of transverse momentum greater than 100 GeV (80 GeV in pp)

2. Hadronic collision event selection criteria [66]

    - At least one reconstructed vertex
    - Primary vertex of $|\mathrm{z}| < 15$ cm
    - Total HF energy $<$ 5500 GeV (Exclude obvious pileup events)
    - 3 towers in HF_{+} and HF_{-} each with minimum energy of 3 GeV.
    - Veto on beam halo events using timing of BSC $\pm$ z signals.
    - Veto on HCal noise for purity of jet sample

Jets are clustered from particle flow objects with anti-k_{T} algorithm, and binned in p_{T}, η, and in case of PbPb centrality. The ratio between pp and PbPb jet spectra, or R_{AA} is defined as

$$R_{\mathrm{AA}} = \frac{d^2N^{AA}/dp_T d\eta}{T_{\mathrm{AA}}\ d^2\sigma^{PP}/dp_T d\eta} \tag{7.10}$$

or the ratio of per minimum bias PbPb event differential jet production (N^{AA}) with the differential cross section of jet production in proton-proton collisions (σ^{pp}), scaled by the nuclear overlap function $T_{\rm AA}$,

$$T_{\rm AA} =< N_{Coll} > /\sigma^{pp}_{inel}. \tag{7.11}$$

which is extracted via Glauber modeling of ion collisions [98]. Table 7.4 shows the set of values used for $T_{\rm AA}$ along with associated errors. In addition to the normalizing $T_{\rm AA}$, the delivered luminosity is necessary for determining the proton-proton jet cross section. This is also shared with other CMS analyses at $\sqrt{s_{_{NN}}}$=5.02 TeV, and is 27.4 pb^{-1} with an error of 2.3% [54].

Table 7.4: Table of $T_{\rm AA}$ values with associated uncertainties. This set of values is shared with other CMS analyses at $\sqrt{s_{_{NN}}}$=5.02 TeV, in particular measurement of charged hadron suppression [54].

Centrality	TAA [mb^{-1}]	% Error Up	% Error Down
0-10%	23.22	1.9	3.0
10-30%	11.51	2.6	3.4
30-50%	3.819	5.4	5.4
50-90%	0.543	11.2	7.3

Reconstructed jets are counted in bins of $p_{\rm T}$, η, and centrality. This spectrum of pure counts is then unfolded according to response matrices dictated by the η, centrality and jet algorithm using the D'Agostini method as encoded in RooUnfold software package [99, 100]. The response matrices are PYTHIA6 embedded in HYDJET at $\sqrt{s_{_{NN}}}$=5.02 TeV with detector conditions matching data-taking. Both nominal distribution is unfolded using this response, and for responses corresponding to systematic errors in energy scale, resolution, fake rate, etc. Typical number of iterations necessary to termination point is 3, with exception for extreme variations of prior (re-weighting the PYTHIA6 prior up and down one power in the $p_{\rm T}$ dependence, resulting slopes well beyond previous observed modification). Termination criteria is χ^2 probability with previous iteration in excess of 95%, accounting for correlated statistical errors. The arbitrariness of the criteria is accounted for by taking adjacent

iterations as systematic band. This is globally subdominant even restricting to just the set of systematics associated with the unfolding procedure.

Fully unfolded jet spectra, now corrected for resolution and non-closure effects, are normalized by η bin width, p_{T} bin width, and normalized by integrated luminosity, in case of pp, or by total number of delivered minimum bias events, in case of PbPb. At this stage spectra measurement is complete, and any additional scaling modification is done for visual aid only.

To compare the production of jets in pp and PbPb, nuclear modification factor is calculated by ratio of PbPb production to pp production scaled by T_{AA}. T_{AA} varies per centrality bin, as shown in Table 7.4 with associated asymmetric errors. The ratio is shown ranging from 200 to 1000 GeV.

Finally, we introduced a new observable R-R_{AA}, or an R_{AA} ratio defined as

$$\mathrm{R}-R_{\mathrm{AA}} = \left(\frac{d^2N^{AA}/dp_T d\eta}{T_{\mathrm{AA}}\ d^2\sigma^{PP}/dp_T d\eta}\right)^R / \left(\frac{d^2N^{AA}/dp_T d\eta}{T_{\mathrm{AA}}\ d^2\sigma^{PP}/dp_T d\eta}\right)^{R=R_0} \tag{7.12}$$

where R_0 is a chosen normalizing resolution parameter. In this measurement, the typical limitations are driven experimentally by limitations of the jet reconstruction, so a good choice for R_0 is R=0.2. Equation 7.12 is written out as it would be from the perspective of two R_{AA}. The full T_{AA} and its associated systematics will cancel completely. Similarly, the luminosity and its associated error will cancel completely, as both R and R_0 must share these. So we can re-write the observable as

$$\mathrm{R}-R_{\mathrm{AA}} = \left(\frac{d^2N^{AA}/dp_T d\eta}{d^2N^{PP}/dp_T d\eta}\right)^R \left(\frac{d^2N^{PP}/dp_T d\eta}{d^2N^{AA}/dp_T d\eta}\right)^{R=R_0} \tag{7.13}$$

or as

$$\mathrm{R}-R_{\mathrm{AA}} = \frac{(d^2N^{AA}/dp_T d\eta)^R}{(d^2N^{AA}/dp_T d\eta)^{R_0}} \frac{(d^2N^{PP}/dp_T d\eta)^{R_0}}{(d^2N^{PP}/dp_T d\eta)^R} \tag{7.14}$$

At which point it is clear that this is a ratio of spectra of simultaneous data-taking period. Indeed, the pp spectra ratio systematics should be almost entirely from unfolding as the scale and resolution differences for changing jet resolution parameter are driven almost entirely by underlying event, and data was taken with an average

pileup of 1.4, for negligible contribution to jet energy at 200 GeV or higher. Spectra ratio in PbPb will have non-negligible scale and resolution error, but there will still be strong cancellation. Finally, there will be large correlations statistically between each spectra, as a significant fraction of jets entering the spectra at normalizing R_0 will also contribute to larger R. This is fully accounted for and statistical errors are reduced accordingly from fully independent assumption to correlated assumption.

7.2.2 Analysis Systematics

Systematics for radial scan of jet cross section production and nuclear modification factors are summarized in Tables 7.5, 7.6, 7.7, 7.8. The sources can be divided into three distinct categories: uncertainty from jets, global uncertainty, and uncertainty from unfolding. Of these,the dominant and most persistent uncertainty comes from jets.

The jet uncertainty on scale has three components, scale error from Monte Carlo non-closures, scale error from data/Monte Carlo differences, and scale error from underlying event. The first two of these are highly correlated between pp and PbPb, Monte Carlo and data, because the detector conditions are effectively identical between PbPb and pp thanks to adjacent data-taking period. The error in scale coming from underlying event cannot cancel so simply in ratios, as it is highly dependent on jet R, and is effectively absent from pp data-taking (pileup of 1.4).

Systematics from non-closure in Monte Carlo is evaluated per jet R, as a function of p_{T} and in coarse η binning of 0 to 1, and 1 to 2. In these bins, deviations in the reconstructed p_{T} ratio with truth p_{T} from 1 are taken as scaling factors. The full analysis apparatus is rerun with jet p_{T} rescaled to new values based on these factors. The deviation in the central values after this rescaling is taken as the uncertainty.

Systematic from non-closures coming from data/Monte Carlo differences are shared with all jet analysis of 2015 data, and was extracted as part of dijet-η analysis [101]. Study of dijet imbalance in pp gave an η dependent non-closure that reached 2% at $|\eta|$ of 2. The full 2% variation is conservatively adopted here, and is propagated through in manner identical to the Monte Carlo level non-closures.

Finally, underlying event error is extracted by looking at the closure of random cone measurements in data and in Monte Carlo. The random cone deviations from zero translate directly to scale non-closures. A 1 GeV non-closure in a random cone for example, is a roughly 3% error on 30 GeV jet. While the random cone non-closures tend to get worst for the largest R, the increasing momentum thresholds at which the measurements begin means they are generally scaled away. Non-closure in random cone is used to vary jet energy in absolute value (for example non-closure given, $\pm$ 1 GeV), and resulting deviations of central values are propagated to final result systematics.

Table 7.5: Systematics on measurements of jet production cross sections in pp and PbPb, binned in centrality. The table shows maximum and minimum values over all p_{T} and R for which the spectra is plotted.

	Percent Error				
	PP	50-90%	30-50%	10-30%	0-10%
JES, MC Non-Closures	9.9-13.4	10.3-11.9	9.9-13.3	10.3-13.6	11.9-14.1
JES, Data/MC Differences	9.9-13.4	10.3-11.9	9.9-13.3	10.3-13.6	11.9-14.1
JES, Underlying Event	0.0-0.0	0.0-3.1	0.0-1.8	0.0-4.3	0.0-4.1
JER, MC Uncertainty	1.1-2.1	1.3-2.5	1.6-2.5	1.7-3.5	2.5-3.5
JER, Data/MC Differences	1.8-2.9	2.1-3.4	2.2-3.6	2.6-4.8	3.7-5.8
Fake Jet Contributions	0.0-0.0	0.0-0.0	0.0-0.0	0.0-0.0	0.0-0.0
Unfolding, Prior Choice	0.0-1.0	0.5-1.4	0.3-2.7	0.3-2.6	0.4-2.0
Unfolding, MC Statistics	0.0-0.2	0.0-0.0	0.0-0.1	0.0-0.3	0.0-0.2
Unfolding, Method Choice	0.0-2.4	1.3-2.3	0.8-1.9	1.1-4.9	0.1-2.8
Unfolding, Termination Point	0.0-0.6	0.0-0.5	0.0-0.8	0.0-1.5	0.4-0.9
Luminosity Uncertainty	2.2-2.2	0.0-0.0	0.0-0.0	0.0-0.0	0.0-0.0
Nuclear Overlap Uncertainty	0.0-0.0	10.0-10.0	5.1-5.1	2.5-2.5	1.8-1.8
Total	14.4-19.4	18.5-19.9	15.8-20.1	16.0-21.3	18.0-21.7

In addition to errors in scale, jet energy resolution, or the width of the response, has significant implications for the unfolding procedure. There are two associated errors from jet energy resolution, a resolution error from the Monte Carlo extraction, and a resolution error from data/Monte Carlo difference. The former error is taken as a flat 7%, and is the rough parameter variation necessary to produce an overlapping band of CSN resolution fits that envelops points. Data/Monte Carlo differences are

taken from dijet-η study of dijet imbalance, and from adjacent run periods [101]. The scale factor for the difference is roughly 10%, with an additional conservative error band taken as 10% around it. So resolution is smeared 10% in the construction of the unfolding matrices globally, and an additional smearing is applied for error calculation. Again, difference with central values is taken as systematic.

Table 7.6: Systematics on ratio measurements of jet production cross sections in pp, for R=0.2 through R=0.8, normalized to R=1.0. The table shows maximum and minimum values over all p_{T} and R for which the spectra is plotted. Strong cancellations in errors associated with jet energy scale and resolution, along with full cancellation of luminosity error, drives most of the reduction when compared with 7.5.

	Percent Error PP
JES, MC Non-Closures	0.0-1.1
JES, Data/MC Differences	0.0-1.1
JER, MC Uncertainty	1.4-2.0
JER, Data/MC Differences	0.0-1.1
Unfolding, Prior Choice	0.0-4.1
Unfolding, MC Statistics	0.0-0.1
Unfolding, Method Choice	0.6-3.3
Unfolding, Termination Point	0.0-2.1
Total	1.8-5.8

Fake jet contributions are globally quite negligible, but are listed here for completeness. Mostly it is intended to illustrate the starting threshold for each spectra in p_{T}, R and centrality is well above background fluctuations and potential fake jets induced from badly reconstructed tracks are not present.

Global observable uncertainties are shared with other CMS analysis such as the charged hadron R_{AA} [54], and come into the normalization of various spectra. Luminosity has an estimated error of 2.3%. This is propagated by varying the 27.4 pb^{-1} by 2.3% and taking difference with nominal (this is why the actual value in the table is not 2.3% in some places, as the variation is in denominator). Likewise, T_{AA} error is estimated per centrality, and variation is carried out as with luminosity.

The final set of uncertainties are associated with the unfolding procedure and account for the impact of prior, finite statistics in the Monte Carlo, the method of

Table 7.7: Systematics on ratio of per-event jet production in minimum bias PbPb events with proton-proton jet production cross section, scaled by nuclear overlap factors in each centrality bin, or R_{AA}. The resultant reductions in uncertainty compared to spectra measurement is largely result of large correlation of energy scale and resolution in pp and PbPb because of shared data-taking conditions of adjacent run periods.

	Percent Error			
	50-90%	30-50%	10-30%	0-10%
JES, MC Non-Closures	0.0-0.3	0.0-1.6	0.0-1.7	0.4-0.8
JES, Data/MC Differences	0.0-0.3	0.0-1.6	0.0-1.7	0.4-0.8
JES, Underlying Event	0.0-3.1	0.0-1.8	0.0-4.3	0.0-4.1
JER, MC Uncertainty	1.3-2.5	1.6-2.5	1.7-3.5	2.5-3.5
JER, Data/MC Differences	0.0-0.9	0.0-1.4	0.0-2.7	1.3-3.7
Fake Jet Contributions	0.0-0.0	0.0-0.0	0.0-0.0	0.0-0.0
Unfolding, Prior Choice	0.5-1.4	0.3-2.7	0.3-2.6	0.4-2.0
Unfolding, MC Statistics	0.0-0.0	0.0-0.1	0.0-0.3	0.0-0.2
Unfolding, Method Choice	1.3-2.3	0.8-1.9	1.1-4.9	0.1-2.8
Unfolding, Termination Point	0.0-0.5	0.0-0.8	0.0-1.5	0.4-0.9
Luminosity Uncertainty	2.3-2.3	2.3-2.3	2.3-2.3	2.3-2.3
Nuclear Overlap Uncertainty	10.0-10.0	5.1-5.1	2.5-2.5	1.8-1.8
Total	10.6-11.2	6.1-7.0	4.3-8.5	4.6-7.9

unfolding, and the arbitrariness in the termination point of the D'Agostini method. These uncertainties are fully independent in all ratios and as a result actually dominate the pp spectra ratio uncertainties.

All uncertainties evaluated above are combined by quadrature sum to give the total uncertainty. In addition to this handling of uncertainty, in certain plots the spectra are highly correlated statistically. In these specific cases, the correlation is evaluated using MC toys, and the uncertainty is reduced by an appropriate factor to account for the correlation. The plotted data has statistical error with full accounting of correlation to maximize significance of results.

Table 7.8: Systematics on double ratio of per-event jet production in minimum bias PbPb events with proton-proton jet production cross section, here denoted R-R_{AA}. The resultant reductions in uncertainty compared to spectra measurement is largely result of large correlation of energy scale and resolution in pp and PbPb because of shared data-taking conditions of adjacent run periods. Furthermore, the luminosity and nuclear overlap uncertainties cancel completely as the centralities are completely shared for a given R/R_0.

	Percent Error			
	50-90%	30-50%	10-30%	0-10%
JES, MC Non-Closures	0.0-0.3	0.0-3.2	0.0-0.8	0.0-1.4
JES, Data/MC Differences	0.0-0.3	0.0-3.2	0.0-0.8	0.0-1.4
JES, Underlying Event	0.0-3.1	0.0-1.8	0.0-5.9	0.0-5.2
JER, MC Uncertainty	0.0-2.3	0.0-4.5	0.0-5.4	0.0-7.2
JER, Data/MC Differences	0.0-0.8	0.0-1.5	0.0-4.3	0.0-5.6
Unfolding, Prior Choice	0.0-3.1	0.0-3.5	0.0-4.2	0.0-7.9
Unfolding, MC Statistics	0.0-0.1	0.0-0.3	0.0-0.7	0.0-0.2
Unfolding, Method Choice	0.0-2.5	0.0-2.9	0.0-9.3	0.0-5.2
Unfolding, Termination Point	0.0-0.6	0.0-0.9	0.0-1.8	0.0-0.8
Total	0.0-4.8	0.0-6.2	0.0-13.9	0.0-13.1

Chapter 8

Results

The following set of results will explore medium modification of jet energy by looking at radial distributions in two different ways. In the first method, studies of missing momentum, particles are projected onto an axis defined by dijet pairs and summed, binned in centrality, dijet asymmetry, and angle relative to dijet axis. In the second method, radial scan of R_{AA}, jet cross sections are measured in pp and PbPb for a wide range of jet resolution parameters R. The ratio of jet production in PbPb and appropriately scaled pp reference is studied for each R, with observed suppression of PbPb jets at small R modestly recovered at the largest R. These two methods inspire new understanding of the interactions between QGP and hard-scattered parton, with the first inspiring serious considerations and implementations of medium recoils in a Monte Carlo quenching models. The second exploits strong cancellations of experimental uncertainties in an observable that is theoretically calculable to strongly constrain the mechanisms by which medium can modify parton energy distribution.

8.1 Missing p_{T} Results in PbPb

All results in the following section are published in [28].

8.1.1 Measurements of Missing p_{T} in PbPb

Figure 8-1 is the multiplicity difference of particles in different p_{T} bins as found in leading and subleading hemisphere. There is a clear enhanced multiplicity of softer particles in the direction of the subleading jets, compensating for a very slight multiplicity enhancement of high-p_{T} particles in the leading jet hemisphere. Since this is not a momentum weighted plot, the multiplicity disparity is sensible (many soft particles compensating for small quantity of harder particles). This effect is indeed observed both in pp and PbPb collisions, and the impact of the medium is not in kind of behavior but rather in magnitude. The difference observed in this magnitude exceeds five standard deviations for p_{T} of particles less than 2 GeV.

There is also a clear ordering in the behavior of jets clustered with different R parameters, almost all of which is coming from the jets in PbPb. Largest cone shows the greatest enhancement of softer particles. As cone size decreases, so does particle enhancement. The ordering is not obviously present in the proton-proton collisions, implying that the additional jet populations introduced with each R in PbPb (by definition broader jets since the additional energy to push the jet above p_{T} threshold must be at the periphery) preferentially interact with the medium in a way that increases the soft particle production. The implication is either that the greater the area over which a jet is distributed, the greater the medium effects, or that the medium interactions that produce broader jets are also more correlated with softer particles. The exact causality is unknown.

Figure 8-2 shows the distribution of the missing momentum projections onto dijet axis in angular bins relative to closest jet of dijet pair for all dijets passing selections. In pp, peripheral PbPb, and central PbPb, there is an observed initial momentum imbalance towards leading jet that is comprised entirely of highest p_{T} particles. The imbalance is slowly reduced at the away side by a collection of lower momentum particles, until getting to a Δ of 2. What distinguishes the PbPb recovery from the pp recovery is the exact nature of the compensating constituents. In pp, the constituents are preferentially intermediate momentum particles, coming from $2 <$

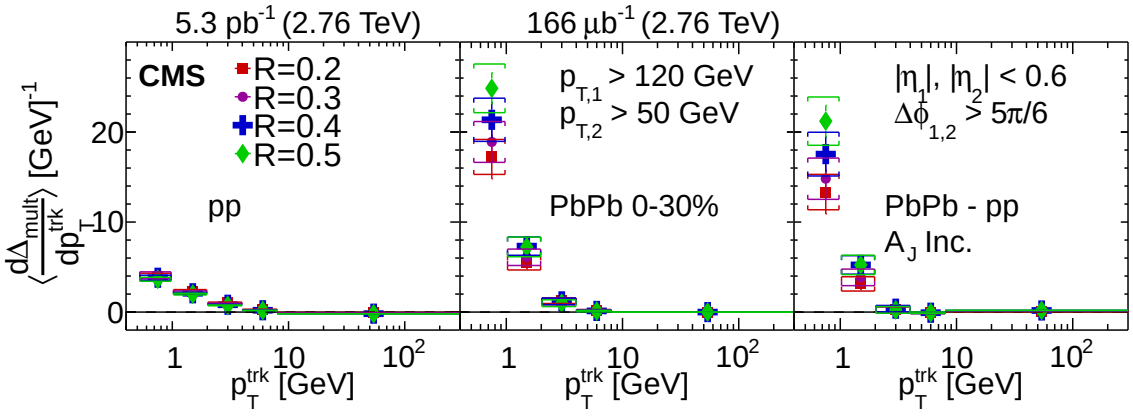

Figure 8-1: Difference in differential multiplicity $\langle \frac{d\Delta_{\rm mult}}{dp_{\rm T}{}^{\rm trk}} \rangle$ between the away-side and leading-jet hemispheres as a function of track $p_{\rm T}$, using an inclusive dijet asymmetry selection. Left panel has measurements in pp for jet radii $R = 0.2, 0.3, 0.4$, and 0.5, and the middle panel displays similar measurements in PbPb. Right panel provides the difference in $\langle \frac{d\Delta_{\rm mult}}{dp_{\rm T}^{\rm trk}} \rangle$ between PbPb and pp collisions for each momentum range. Systematic uncertainties are shown as boxes. Error bars represent statistical uncertainties.

$p_{\rm T} < 8$ GeV. In peripheral PbPb selection of 30-100%, there is still some contribution from this bin, but some of the compensating momentum is now replaced by particles in the $0.5 < p_{\rm T} < 1$ GeV range. Finally, in central most PbPb, the majority of compensating momentum is coming from these softer particles, and they are found at larger angles than is found in the pp case.

The magnitude of the observed recovered momentum and set of particles on the subleading jet side can be controlled not only with PbPb centrality selection, but also by selecting jet asymmetry. For example, in Figure 8-3 we see that for a balanced dijet selection, $A_J < 0.22$, that the magnitude of the imbalance is reduced, as is the soft particle contribution to subleading jet hemisphere. However, if we select highly asymmetric jets, as in Figure 8-4, the signal from soft particles is not only dramatically enhanced, but it is now clear that the particles of $2 < p_{\rm T} < 8$ are missing at all angles (bottom right panel, PbPb - pp and of green and orange on leading jet hemisphere). This represents a mixing of physics effects. In proton-proton collisions, highly asymmetric dijets are usually indicative of a multijet configuration, with remainder of momentum balance being compensated by a third jet. The third

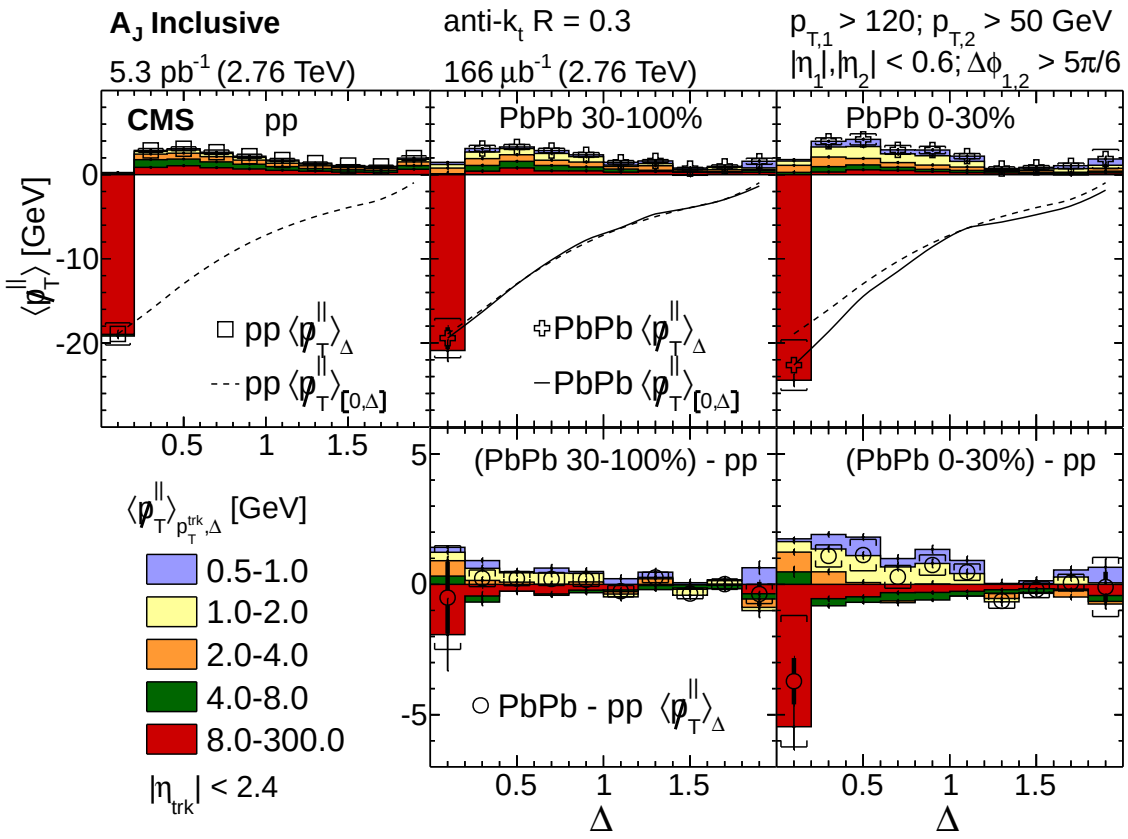

Figure 8-2: Upper row: $\langle \not{p}_{\mathrm{T}}^{\parallel} \rangle_{p_{\mathrm{T}}^{\mathrm{trk}},\Delta}$ distributions for pp, and for 30–100% and 0–30% PbPb data for five track-p_{T} ranges (colored boxes), for momentum ranges from $0.5 < p_{\mathrm{T}} < 1$ GeV (light blue) to $8 < p_{\mathrm{T}} < 300$ GeV (red), as a function of Δ. Also shown is $\langle \not{p}_{\mathrm{T}}^{\parallel} \rangle_{\Delta}$ as a function of Δ for pp (open squares) and PbPb data (open plus symbols). Dashed lines (pp) and solid lines (PbPb) show $\langle \not{p}_{\mathrm{T}}^{\parallel} \rangle_{[0,\Delta]}$ (i.e. integrating the $\langle \not{p}_{\mathrm{T}}^{\parallel} \rangle_{\Delta}$ over Δ from Δ=0 up to the point of interest). Lower row: Difference between the PbPb and pp $\langle \not{p}_{\mathrm{T}}^{\parallel} \rangle_{p_{\mathrm{T}}^{\mathrm{trk}},\Delta}$ distributions according to the range in p_{T}, as a function of Δ (colored boxes), and difference of $\langle \not{p}_{\mathrm{T}}^{\parallel} \rangle_{\Delta}$ as a function of Δ (open circles), error bars and brackets represent statistical and systematic uncertainties, respectively.

jet would be comprised of these intermediate particle momentum and could occupy the full Δ angular range available in η. In PbPb multijet configurations are still present, but the medium effect acts to additionally enhance the asymmetry of true dijet events. This effect will also be evident in radial scans.

Figure 8-5 sums over Δ to remove the angular information and just measures projected momentum sums as a function of the dijet imbalances in pp and PbPb centrality bins 50-100%, 30-50%, 10-30%, and 0-10%. The p_{T}-binned imbalance in pp shows that the leading jet imbalance dominated by particles from highest momentum is mostly balanced by intermediate momentum particles. Moving to PbPb collisions and to more central events, these intermediate particles are preferentially replaced by particles in lowest momentum bin, of $0.5 < p_{\mathrm{T}} < 2.0$. One interesting aspect of this transition is that the lost particles seem to come almost exclusively from $4 < p_{\mathrm{T}} < 300$, and $2 < p_{\mathrm{T}} < 4$ is constant. This is not indicative of no modification of hadrons in this region. Rather, it suggests that the inflow of particles from higher momentum perfectly balances the outflow of these particles to lower momentum, at least relatively between leading and subleading jet. There is an overall observed momentum imbalance in asymmetric jet configurations for pp and PbPb events, but this is attributed to uncorrected acceptance effects (pseudorapidity and momentum cutoffs) and they are clearly shared between the systems within statistical and systematic uncertainty.

Figure 8-6 shows the p_{T}-bin collapsed multiplicity measurement of Figure 8-1. Peripheral PbPb and pp collisions have leading-subleading hemisphere multiplicities that are one sigma compatible in all $A_J$selections. The pp multiplicities are also well modeled by PYTHIA, as well as PYTHIA embedded in HYDJET to simulate the addition of PbPb background but without quenching effects on jets. As the centrality goes to central-most, the multiplicity difference is enhanced to the 2-3 sigma level, depending on centrality and A_J. This demonstrates that the observed enhancements are the effect of quenching physics, as the PYTHIA+HYDJET does not follow this trend.

Figure 8-7 is the Δ binned momentum projection in pp and central PbPb events

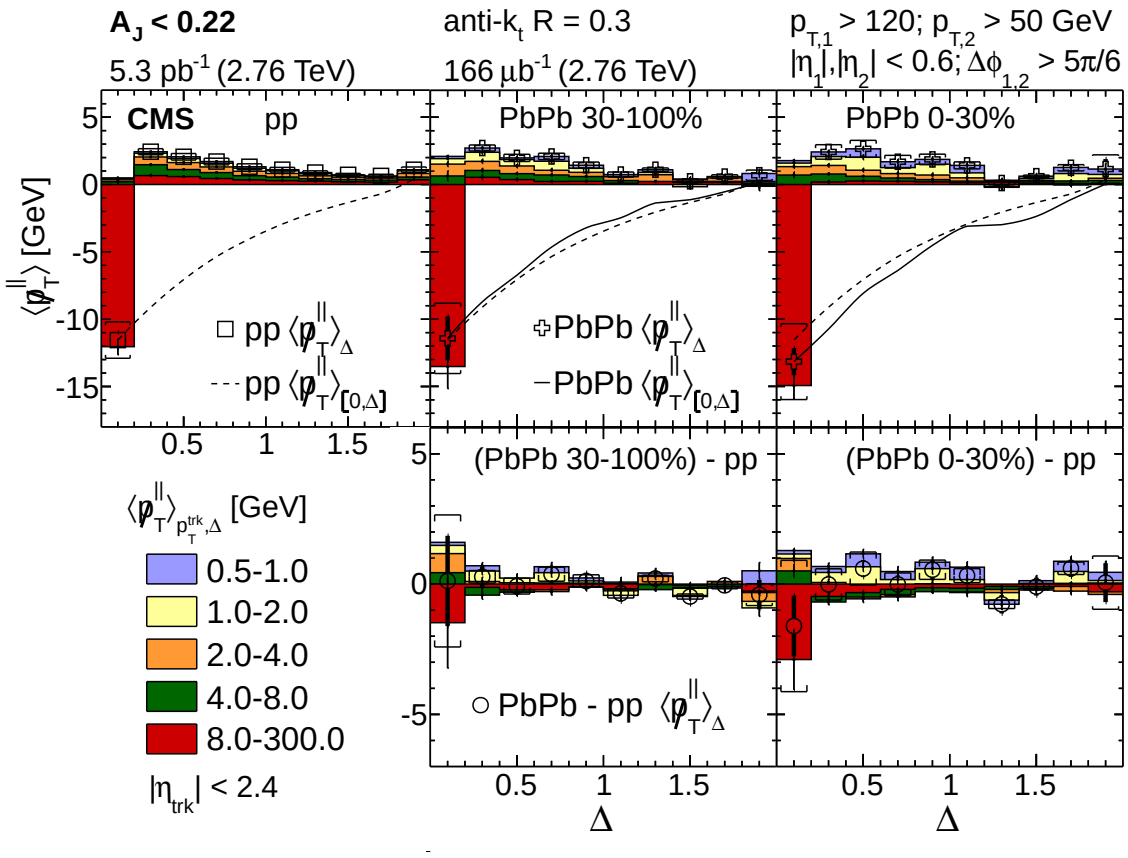

Figure 8-3: Same as Fig. 8-2, but with a balanced dijet selection ($A_J < 0.22$). Upper row: $\langle \not{p}_{\mathrm{T}}^{\parallel} \rangle_{p_{\mathrm{T}}^{\mathrm{trk}},\Delta}$ distributions for pp, and for 30–100% and 0–30% PbPb data for five track p_{T} ranges (colored boxes), as a function of Δ. Also shown is $\langle \not{p}_{\mathrm{T}}^{\parallel} \rangle_{\Delta}$ as a function of Δ for pp (open squares) and for PbPb data (open plus symbols). Dashed lines (pp) and solid lines (PbPb) show $\langle \not{p}_{\mathrm{T}}^{\parallel} \rangle_{[0,\Delta]}$ (i.e. integrating the $\langle \not{p}_{\mathrm{T}}^{\parallel} \rangle_{\Delta}$ over Δ from $\Delta = 0$ up to the point of interest). Lower row: Difference in the $\langle \not{p}_{\mathrm{T}}^{\parallel} \rangle_{p_{\mathrm{T}}^{\mathrm{trk}},\Delta}$ distributions for the PbPb and pp according to the range in p_{T}, as a function of Δ (colored boxes), and difference of $\langle \not{p}_{\mathrm{T}}^{\parallel} \rangle_{\Delta}$ as a function of Δ (open circles). Error bars and brackets represent statistical and systematic uncertainties, respectively. The y-axis range on the top panels are smaller than in Fig. 8-2.

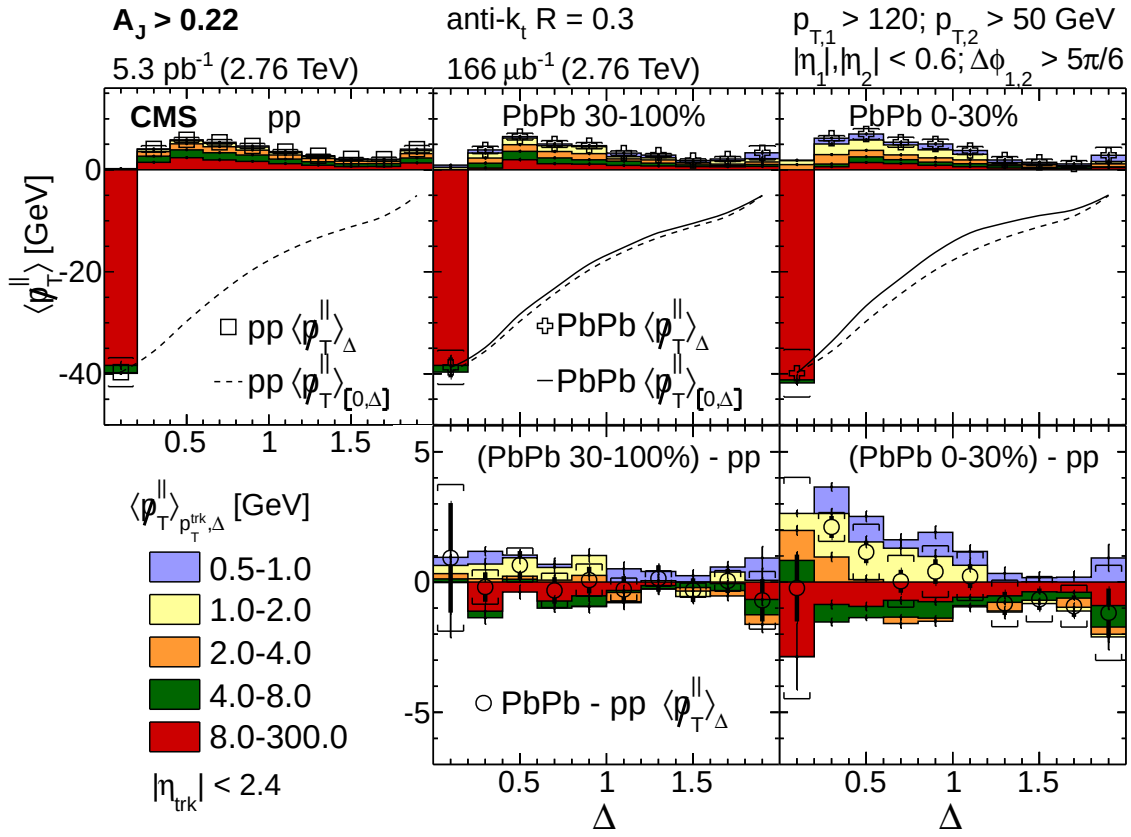

Figure 8-4: Same as Fig. 8-2, but with an unbalanced dijet selection ($A_J > 0.22$). Upper row: $\langle \not{p}_T^{\parallel} \rangle_{p_T^{trk},\Delta}$ distributions for pp, and for 30–100% and 0–30% PbPb data for five track p_T ranges, as a function of Δ. Also shown is $\langle \not{p}_T^{\parallel} \rangle_{\Delta}$ as a function of Δ for pp and for PbPb data. Dashed lines (pp) and solid lines (PbPb) show $\langle \not{p}_T^{\parallel} \rangle_{[0,\Delta]}$ (i.e. integrating the $\langle \not{p}_T^{\parallel} \rangle_{\Delta}$ over Δ from $\Delta = 0$ up to the point of interest). Lower row: Difference in the $\langle \not{p}_T^{\parallel} \rangle_{p_T^{trk},\Delta}$ distributions for the PbPb and pp. Error bars and brackets represent statistical and systematic uncertainties, respectively. The y-axis range on the top panels are larger than in Fig. 8-2.

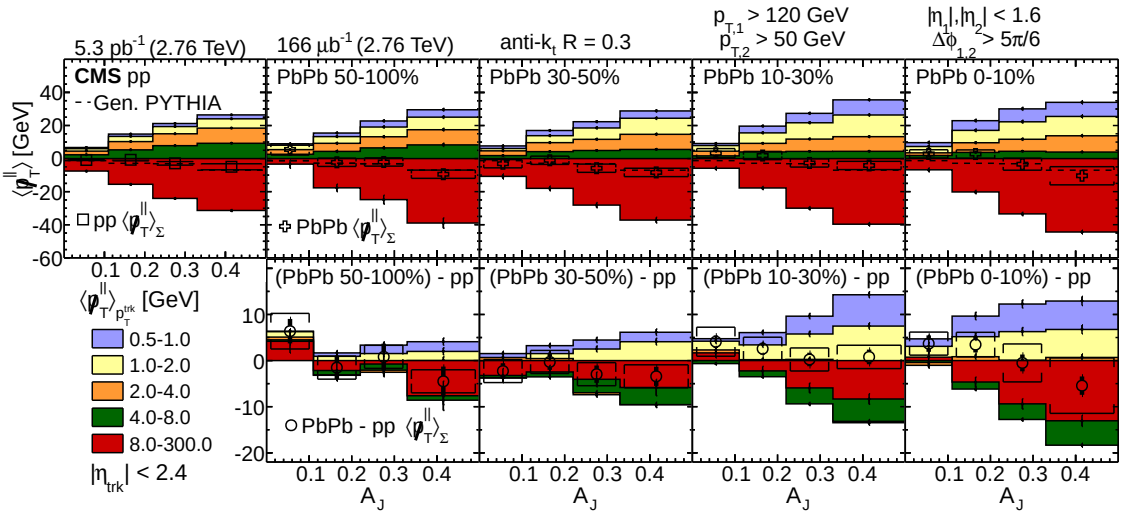

Figure 8-5: Upper row has $\langle \not{p}_{\mathrm{T}}^{\parallel} \rangle_{p_{\mathrm{T}}^{\mathrm{trk}}}$ and $\langle \not{p}_{\mathrm{T}}^{\parallel} \rangle_{\Sigma}$ in pp collisions (leftmost) and in four selections of PbPb for collision centralities from 50–100% to 0–10%. The open markers show $\langle \not{p}_{\mathrm{T}}^{\parallel} \rangle_{\Sigma}$, p_{T} balance for tracks with $0.5 < p_{\mathrm{T}} < 300$ GeV, while the colored boxes show the $\langle \not{p}_{\mathrm{T}}^{\parallel} \rangle_{p_{\mathrm{T}}^{\mathrm{trk}}}$ contributions for different track p_{T} ranges. For each panel, $\langle \not{p}_{\mathrm{T}}^{\parallel} \rangle_{p_{\mathrm{T}}^{\mathrm{trk}}}$ and $\langle \not{p}_{\mathrm{T}}^{\parallel} \rangle_{\Sigma}$ values are shown as a function of dijet asymmetry. The lower row shows the difference between $\langle \not{p}_{\mathrm{T}}^{\parallel} \rangle_{p_{\mathrm{T}}^{\mathrm{trk}}}$ and $\langle \not{p}_{\mathrm{T}}^{\parallel} \rangle_{\Sigma}$ for PbPb and pp data. Error bars and brackets represent statistical and systematic uncertainties, respectively.

for 4 different populations of jets, keeping momentum and pseudorapidity selection criteria constant but varying the R parameter from 0.2 to 0.5 in increments of 0.1. The dijet asymmetry is inclusive in this plot. In pp, the increasing R has a two-fold impact: the initial asymmetry drops as more of the subleading jet radiation at cone edge is recovered, and the subleading hemisphere peak migrates to large Δ. In part this is because the added populations of jets with each R tend to be more balanced near axis, and multijet configurations become more important.

In contrast, the initial momentum imbalance in PbPb shows less dependence on R, and while the peak still shifts towards larger Δ with increasing R, the shift is smaller in PbPb. This is consistent with the previously discussed interplay between multijet configurations and medium effect on dijet configuration in PbPb.

The bottom panel shows the difference in distributions of PbPb and pp momentum balance for all R. While the enhancement of soft particles is seen globally, it is most pronounced with the addition of jets that only pass cuts at large R, jets with energy

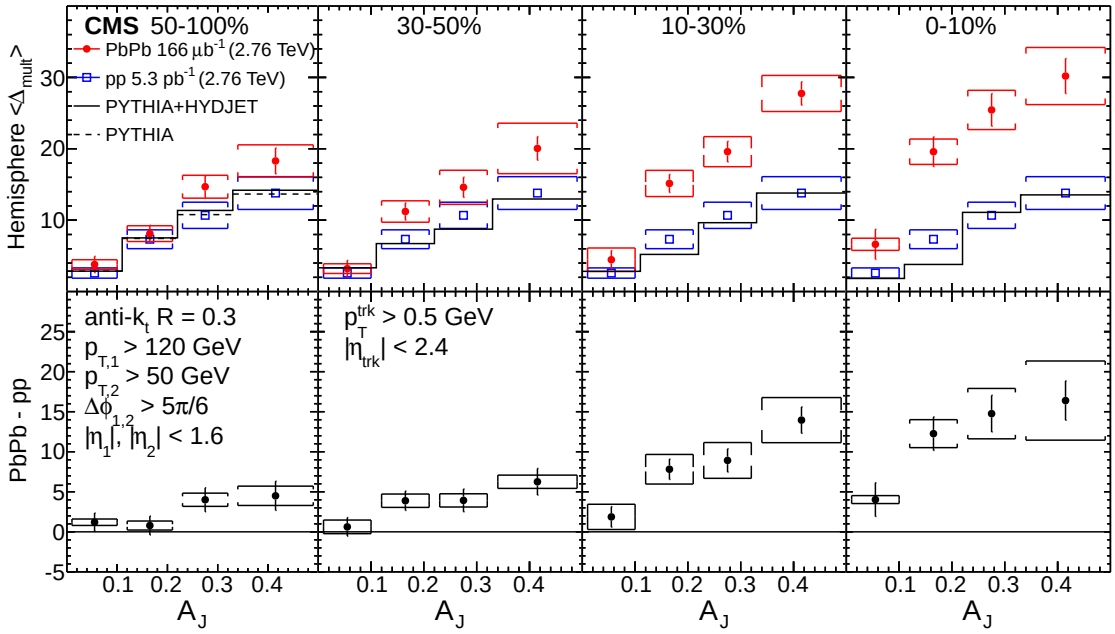

Figure 8-6: Upper panels show the comparison of the mean difference in multiplicity $\langle\Delta_{\mathrm{mult}}\rangle$ between the subleading jet hemisphere and leading jet hemisphere, as a function of dijet asymmetry $A_J$for pp (blue squares), PbPb (red filed circles), PYTHIA (dashed histogram), and PYTHIA+HYDJET events (black histogram). The centralities of PbPb collisions are 50–100%, 30–50%, 10–30 %, and 0–10%, respectively, from leftmost to rightmost panel. Lower panels provide the difference in $\langle\Delta_{\mathrm{mult}}\rangle$ between PbPb and pp collisions. Statistical and systematic uncertainties are shown as error bars and brackets, respectively.

more broadly distributed.

Figure 8-8 is collapses the Δ distribution into an angle integrated momentum balance binned in asymmetry. Magnitude of soft particle enhancement has a strong dependence on R for all A_J, again suggesting that the broader jets are more sensitive to medium interaction, or that the medium is preferentially producing final state configurations of greater broadness.

8.1.2 Impact of Missing p_{T} on Medium Modeling

Missing momentum studies have had significant impact on generator implementations of energy loss, specifically refocusing attention on the soft particles resulting from energy loss previously ignored. For example, Figure 8-9 shows hybrid model with and without the recoiling medium incorporated into its study of missing momentum. Qualitatively it is clear that the hybrid model cannot adequately explain the missing momentum measurements from the final state quenched jet alone. However, the incorporation of the medium shows soft particles distributed through large angles. Indeed, this was already a conclusion of the original missing momentum studies by CMS and had been incorporated in studies like those in [102] of Q-PYTHIA, as seen in Figure 8-10, but whereas original studies used a very coarse binning of inside or outside a cone of 0.8 with respect to leading jet axis, a finer binning is now incorporated.

Likewise, the JEWEL model has refocused on the incorporation of medium with the release of a custom subtraction technique in version 2.0. In particular, Figure 8-11 clarifies the pitfall in replicating physics effects in medium with Monte Carlo. Traditionally jet quenching physics has focused on jet signal and underlying event as background. Correlated background in this figure is meant to highlight that jet energy "lost" to medium interaction, if it remains local, will still be reconstructed as part of the jet. Medium interaction may be stronger than even dijet asymmetry or spectra suppression indicates, as some fraction of the interaction leaves energy local to be captured by clustering algorithm. Monte Carlo implementations that simply throw away this lost jet energy will fail to capture the full interaction, and a more careful treatment is necessary. Linearized Boltzmann Transport model, or LBT, is

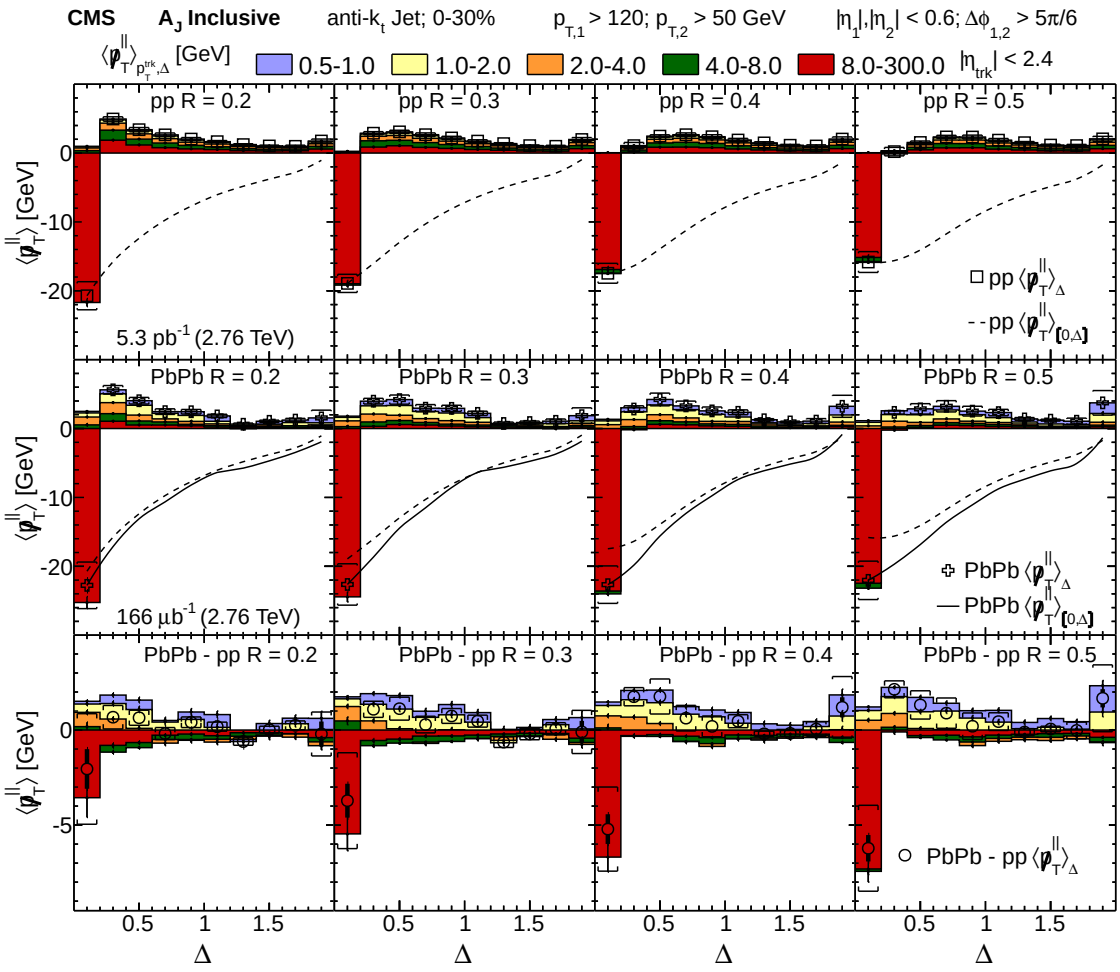

Figure 8-7: Upper row shows $\langle \not{p}_{\mathrm{T}}^{\parallel} \rangle_{p_{\mathrm{T}}^{\mathrm{trk}},\Delta}$ in pp collisions as a function of Δ, for a distance parameter $R = 0.2, 0.3, 0.4$, and 0.5, from left to right for different ranges of track p_{T}, and $\langle \not{p}_{\mathrm{T}}^{\parallel} \rangle_{\Delta}$ (i.e. $\langle \not{p}_{\mathrm{T}}^{\parallel} \rangle_{p_{\mathrm{T}}^{\mathrm{trk}},\Delta}$ summed over all p_{T} for a given Δ bin). Dashed lines indicate cumulative results for $\langle \not{p}_{\mathrm{T}}^{\parallel} \rangle_{[0,\Delta]}$ in pp, for each distance parameter (i.e. integrating $\langle \not{p}_{\mathrm{T}}^{\parallel} \rangle_{\Delta}$ over the Δ range from $\Delta = 0$ to the point of interest). Middle row provides $\langle \not{p}_{\mathrm{T}}^{\parallel} \rangle_{p_{\mathrm{T}}^{\mathrm{trk}},\Delta}$ and $\langle \not{p}_{\mathrm{T}}^{\parallel} \rangle_{\Delta}$ in PbPb collisions of centrality range 0–30% as a function of Δ, for distance parameters $R = 0.2, 0.3, 0.4$, and 0.5 from left to right. Solid line indicates $\langle \not{p}_{\mathrm{T}}^{\parallel} \rangle_{[0,\Delta]}$ in PbPb for each distance parameter. Lower row has the difference between PbPb and pp. Error bars and brackets represent statistical and systematic uncertainties, respectively. The results are inclusive in the dijet asymmetry parameter A_J.

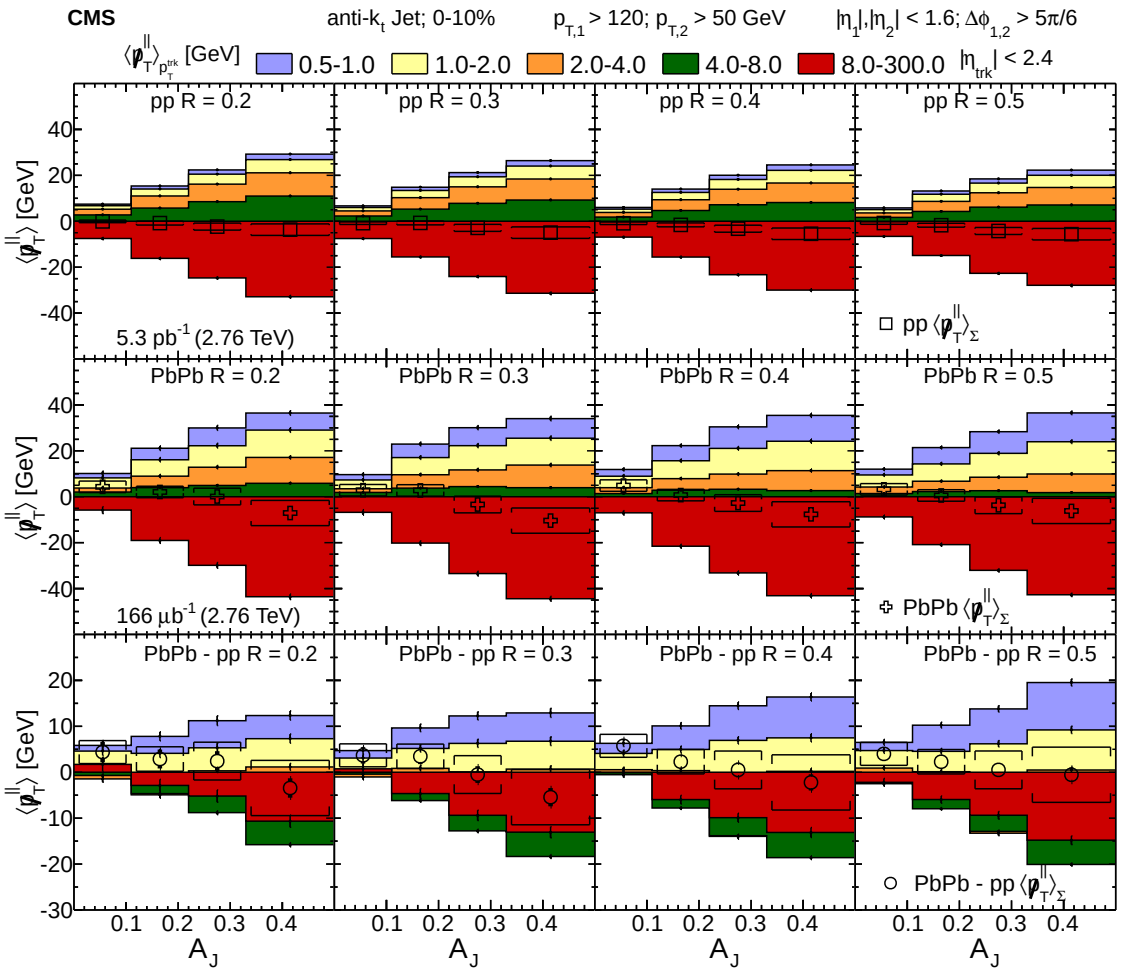

Figure 8-8: Upper row shows $\langle \not{p}_{\mathrm{T}}^{\parallel} \rangle_{p_{\mathrm{T}}^{\mathrm{trk}}}$ (the individual track p_{T}) and $\langle \not{p}_{\mathrm{T}}^{\parallel} \rangle_{\Sigma}$ (sum over all ranges of track p_{T}) as a function of $A_J$in pp collisions for distance parameters $R = 0.2, 0.3, 0.4$, and 0.5, from left to right. The dijet asymmetry ranges from almost balanced ($A_J < 0.11$) to unbalanced ($A_J > 0.33$) dijets. Middle row provides $\langle \not{p}_{\mathrm{T}}^{\parallel} \rangle_{p_{\mathrm{T}}^{\mathrm{trk}}}$ and $\langle \not{p}_{\mathrm{T}}^{\parallel} \rangle_{\Sigma}$ as a function of $A_J$in PbPb collisions of centrality range 0–10%, for distance parameter $R = 0.2, 0.3, 0.4$, and 0.5, from left to right. Lower row has the difference PbPb – pp of the $\langle \not{p}_{\mathrm{T}}^{\parallel} \rangle_{p_{\mathrm{T}}^{\mathrm{trk}}}$, and $\langle \not{p}_{\mathrm{T}}^{\parallel} \rangle_{\Sigma}$, which are shown in the upper panels. Error bars and brackets represent statistical and systematic uncertainties, respectively.

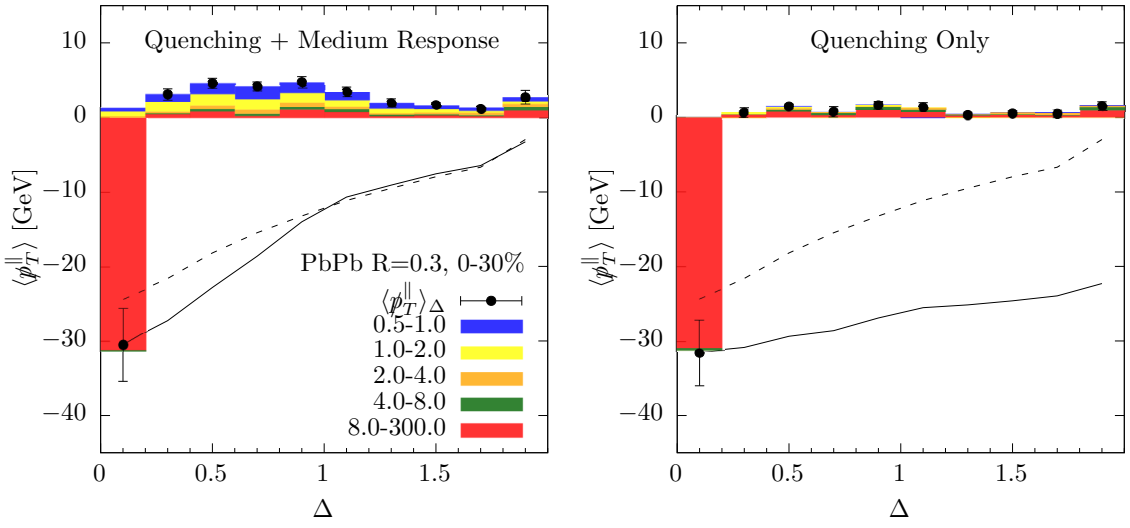

Figure 8-9: Missing momentum studies with the hybrid model of jet quenching [43]. The left plot ignores the impact of the medium recoil and just shows the quenched jet, while the right plot incorporates this additional physics of medium recoil.

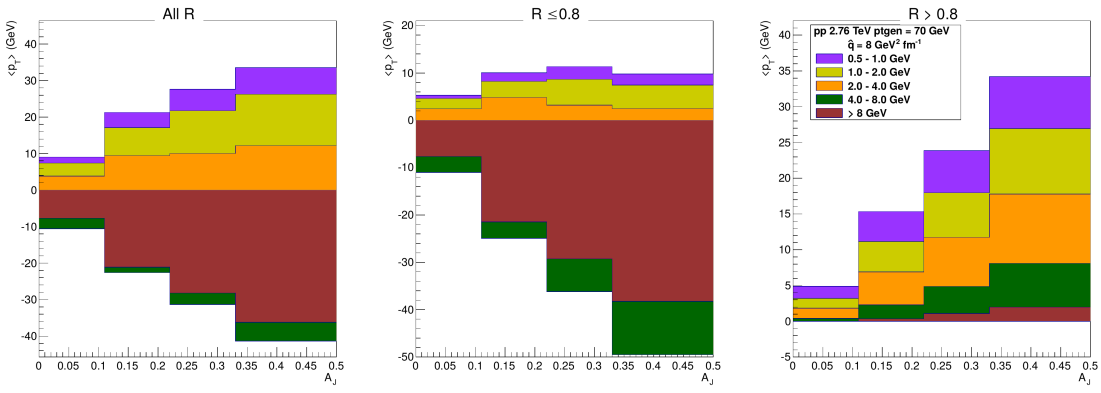

Figure 8-10: Q-PYTHIA studies of missing momentum based on initial studies by CMS in 2011 [24]. Figure via [102].

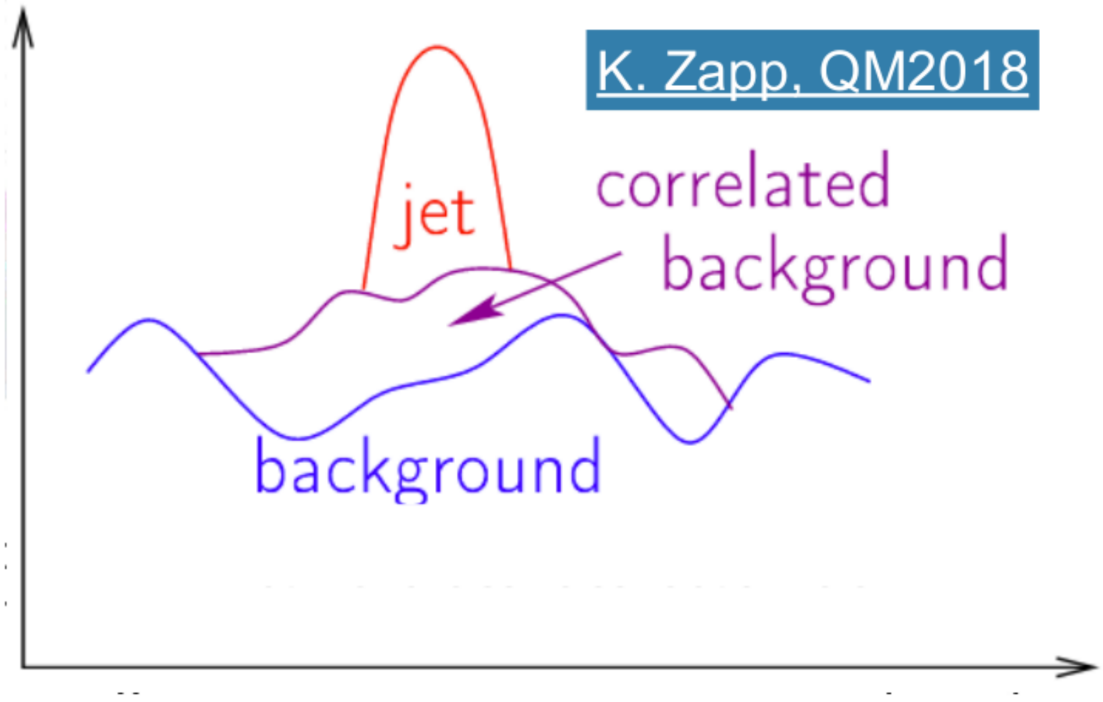

Figure 8-11: Diagram of energy categories in jet quenching measurements. The signal and background categories are those traditionally studied, but the correlated background coming from jet energy deposited in medium is more ambiguously treated historically. Adapted from talk by Korinna Zapp at 2018 Quark Matter.

quite similar to JEWEL insomuch as quenching manifests as 2-to-2 scatterings that are fully perturbative. However, energy lost bu the jet is imparted on soft thermal medium particles (the transport component) and if still local as described above may be kept in the jets reconstruction. Figure 1-21, top left panel labeled CCNU, shows the prediction of LBT model with and without the possibility of recapturing local energy loss in a large R-RAA. The impact of medium on this measurement changes final result from no dependence to strong monotonic dependence.

8.2 Radial Scan of Jet R_{AA}

Figure 8-14 shows a radial scan of pp jet spectra for resolution parameters R=0.2 thru R=0.8, normalized to the spectra of R=1.0 jets. Similar measurements have been made in the past by ALICE and CMS [62, 103]. The measurement of jet spectra ratios by radius is particularly constraining as in the absence of significant underlying event, the systematics associated with jet energy scale and resolution will mostly cancel. Additionally, statistical errors are highly correlated as jets contributing to spectra at one resolution parameter R will likely contribute to other R. The statistical errors in Figure 8-14 are reduced accounting for these correlations using toy studies, increasing the significance of the result. The reduction in statistical error is largest in R=0.8 case as it is closest to normalizing radius R=1.0, while it is smallest for R=0.2. Error associated with luminosity determination cancels completely.

Data comparisons to PYTHIA6 and PYTHIA8 are shown in Fig. 8-14. The spectra ratios show already that in vacuum, a leading order reference point of PYTHIA6 or PYTHIA8 deviates from data going from largest to smallest radius by up to 20%, outside of the experimental error. The relative production of R=1.0 jets from R=0.2 jets in data exceeds the LO prediction. Thus a proper comparison must take an NLO reference if it wishes to correctly replicate the medium effects. As example, a model of quenching that matches the results of the R-RAA but takes as its reference point the LO Monte Carlo like PYTHIA will be working from an incorrect radial distribution of jet energy. Since in many models there is an assumed difference in quenching

strength for jets of different broadness (perhaps partially explained by correlation between wider jets and gluon color charge), the model would in fact not correctly describe medium interactions. This measurement is therefore essential to understand quenched jets and the redistribution of energy throughout the event. The conclusion that LO Monte Carlo is insufficient to characterize jet spectra ratios is shared by CMS analysis at $\sqrt{s_{NN}}$ =7 TeV [103].

Figures 8-15, 8-16 show measured R_{AA} for small and large cone choices. Depending on centrality and jet R, measurement is restricted to its plotted p_{T} range because of underlying event fluctuations limiting the ability to reliably reconstruct jets. Comparing each plot on its own gives a very consistent picture of jet quenching at all R: roughly factor 2 suppression in central most binning, with some modest recovery at high-pt, for all R. However, many of the systematic and statistical errors are shared between the pp and PbPb data points. Figures 8-17, 8-18 of the R_{AA} ratios feature the reduced the systematic and statistical errors by accounting for these correlations, to show that there is statistically significant reduction in jet energy suppression when going from R=0.2 to R=1.0, although it is roughly 20% recovery.

The modest recovery of the jet spectra at largest R is more in line with the predictions of the Hybrid model, than JEWEL or LBT. In addition, the observation seems to contradict the naive expectation set out by the missing momentum study. How at this R value have we still not recovered all jets? The question is partially answered by the spectra ratio in vacuum. At each step in R, we introduce significant new populations of jets all the way up to R=1. The observed factor 2 suppression at R=0.2 is also the full magnitude of jets introduced when we move to R=1.0. As a result, one can fully recover the energy of jets that were reconstructed at R=0.2 to R=0.3, but have suppressed the full set of new jets introduced, because the energy on their periphery has been quenched beyond the cone. While this is a simplification of the overall interactions, it is intended to illustrate that jets exist at many different scales of momentum and angle, and just because a jet is defined for a given R does not mean that the parton's energy instantaneously terminates.

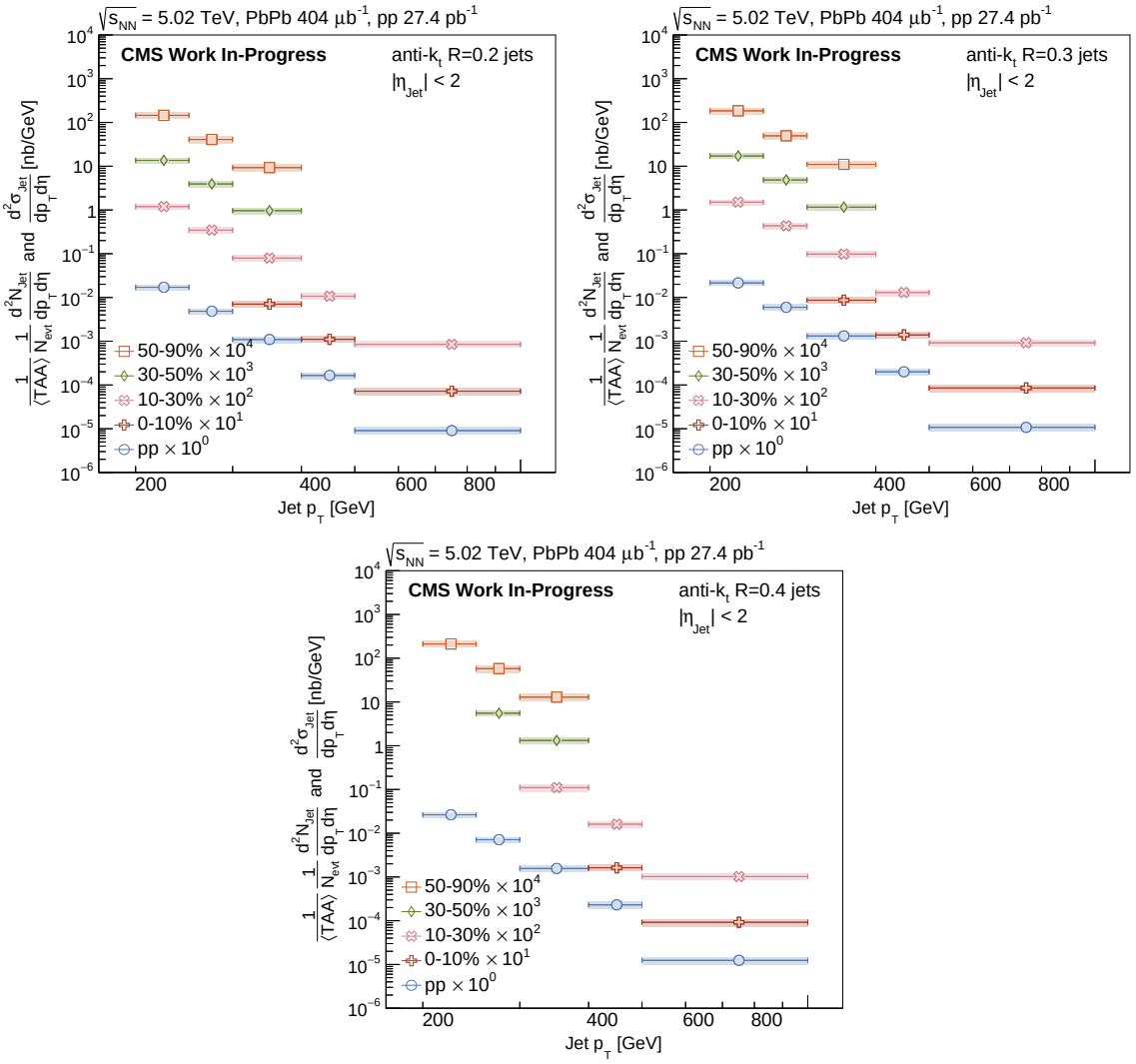

Figure 8-12: The unfolded p_{T} spectra of jets reconstructed with radius parameter, from left to right, top to bottom, $R = 0.2$, $R = 0.3$, and $R = 0.4$ in pp and PbPb collisions of $\sqrt{s_{NN}}$ =5.02 TeV.

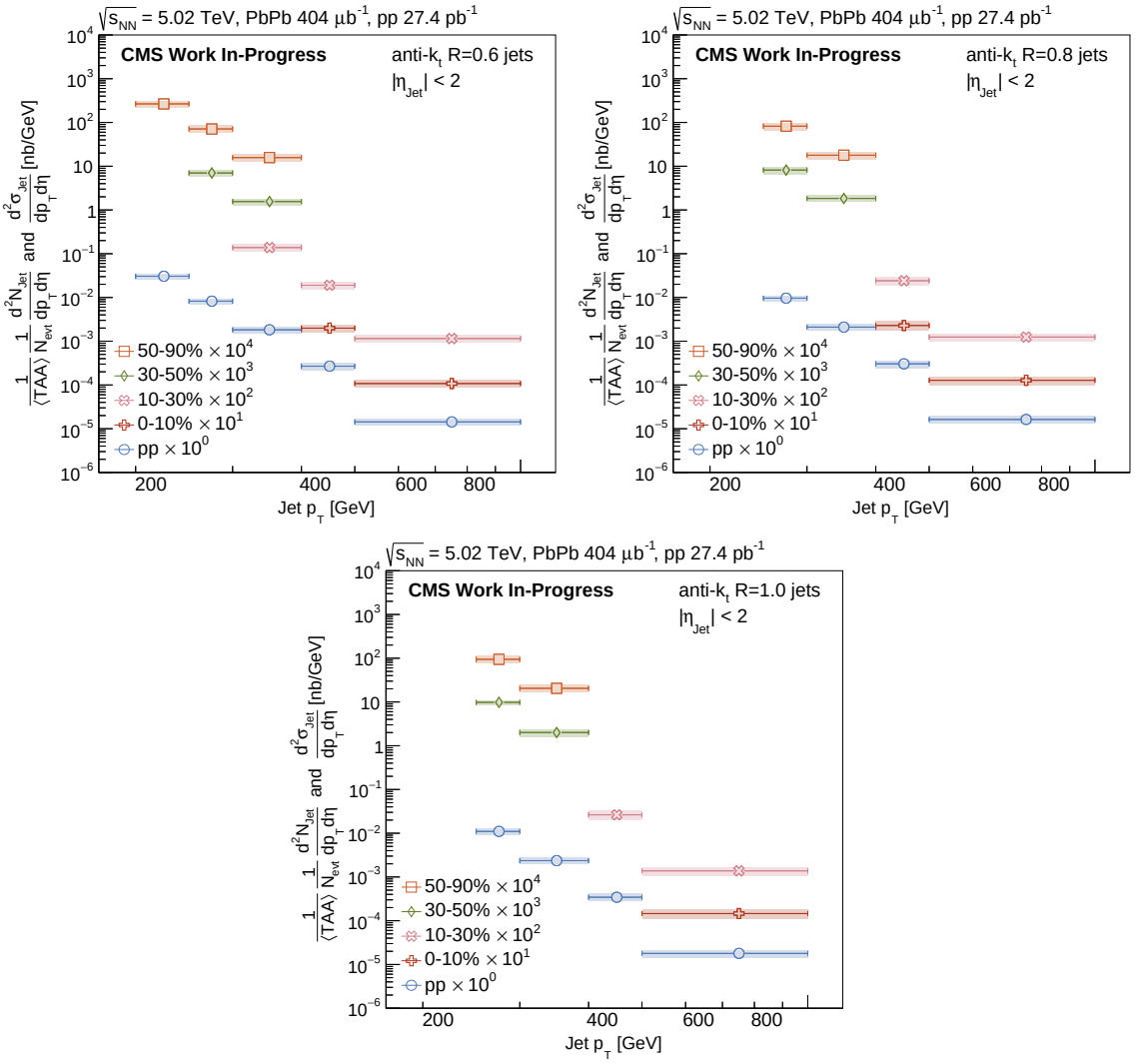

Figure 8-13: The unfolded p_{T} spectra of jets reconstructed with radius parameter, from left to right, top to bottom, $R = 0.6$, $R = 0.8$, and $R = 1.0$ in pp and PbPb collisions of $\sqrt{s_{NN}}$ =5.02 TeV.

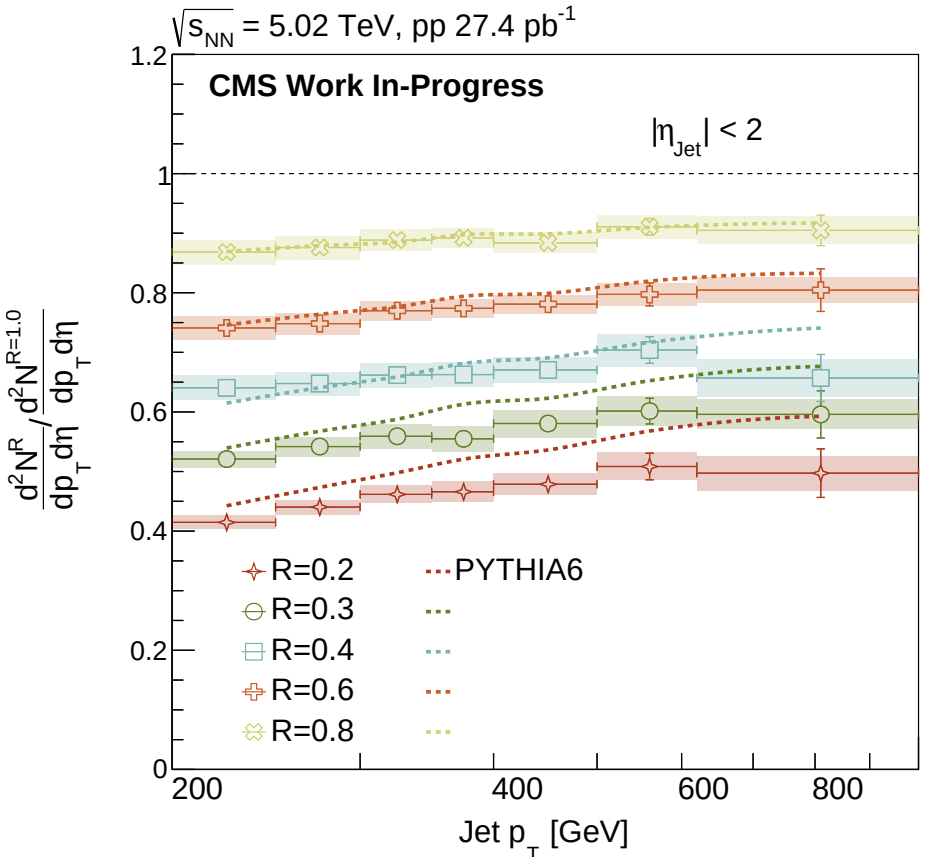

Figure 8-14: Ratio of fully unfolded jet spectra as produced in proton-proton collisions at 5.02 TeV, for resolution parameters R=0.2 thru R=0.8 with respect to R=1.0, for transverse momentum of 160 GeV/c to 1000 GeV/c. Systematics related to jet energy scale, resolution, and luminosity all cancel strongly. The remaining systematics are dominated by those related to unfolding. Correlations between the spectra themselves are fully accounted for in the statistical errors. The resulting spectra strongly constrains the reference spectra for theoretical comparisons. In particular, leading order perturbative calculations of jet spectra ratios are excluded by the data at the available precision.

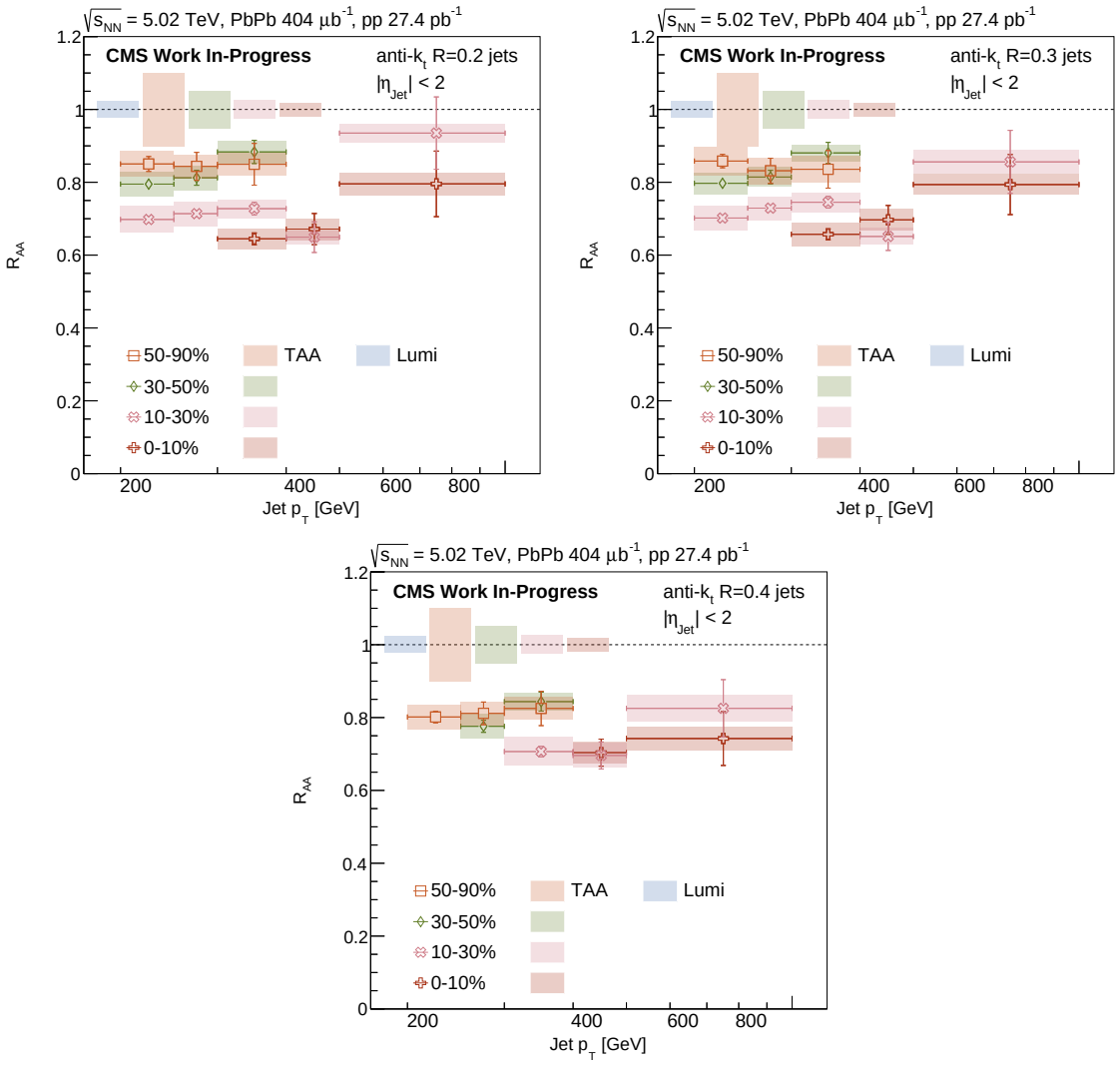

Figure 8-15: The jet RAA using jets reconstructed with radius parameter from left to right, top to bottom, $R = 0.2$, $R = 0.3$, and $R = 0.4$ in pp and PbPb collisions of $\sqrt{s_{NN}}$ =5.02 TeV. Strongest suppression is observed in central-most events, 0-10%. RAA increases as centrality goes to peripheralmost, 50-90%.

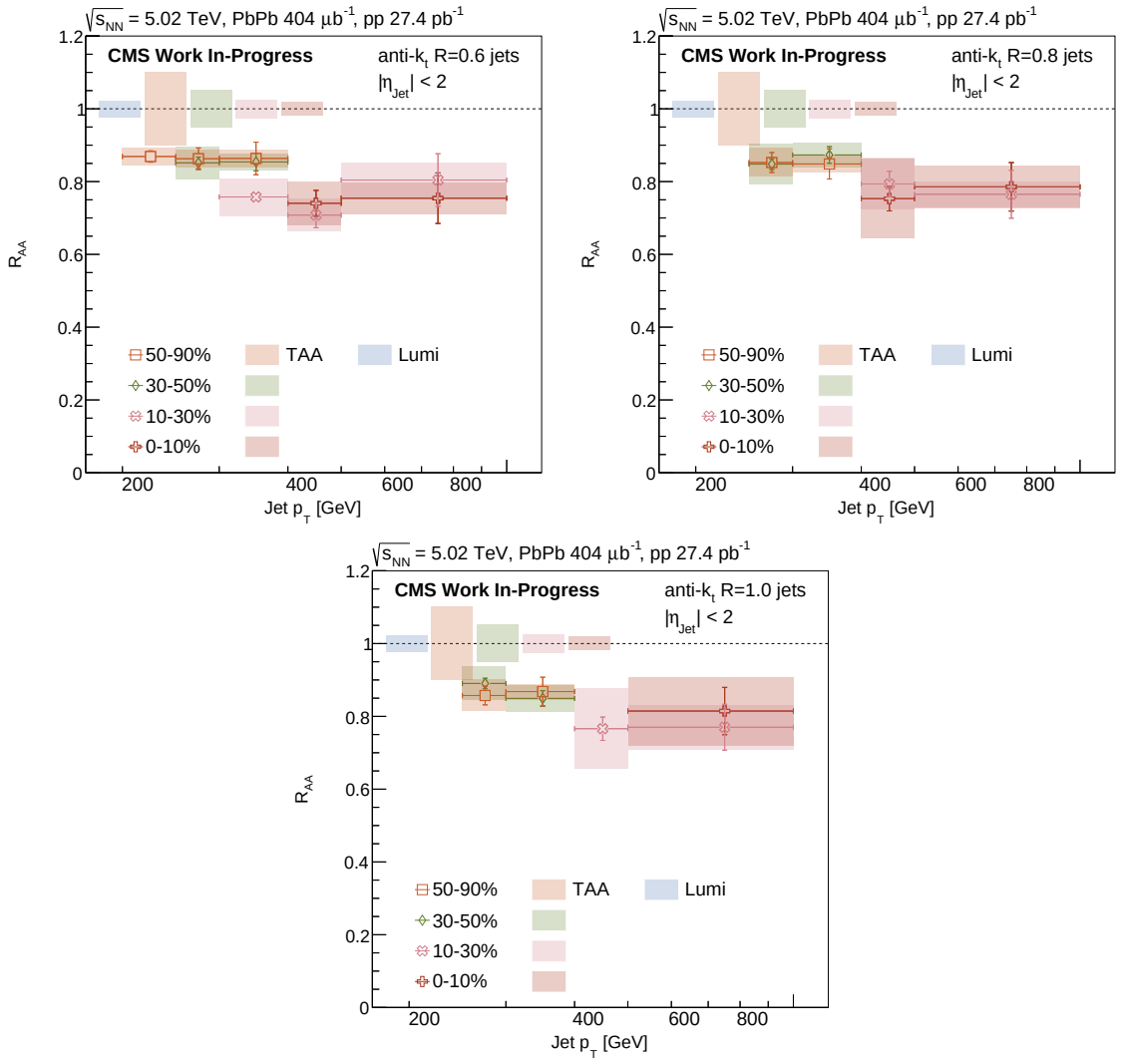

Figure 8-16: The jet RAA using jets reconstructed with radius parameter from left to right, top to bottom, $R = 0.6$, $R = 0.8$, and $R = 01.0$ in pp and PbPb collisions of $\sqrt{s_{NN}}$ =5.02 TeV. Strongest suppression is observed in central-most events, 0-10%. RAA increases as centrality goes to peripheral-most, 50-90%. Large fluctuations in underlying event in central-most collisions limits the large cone RAA to the highest available p_T.

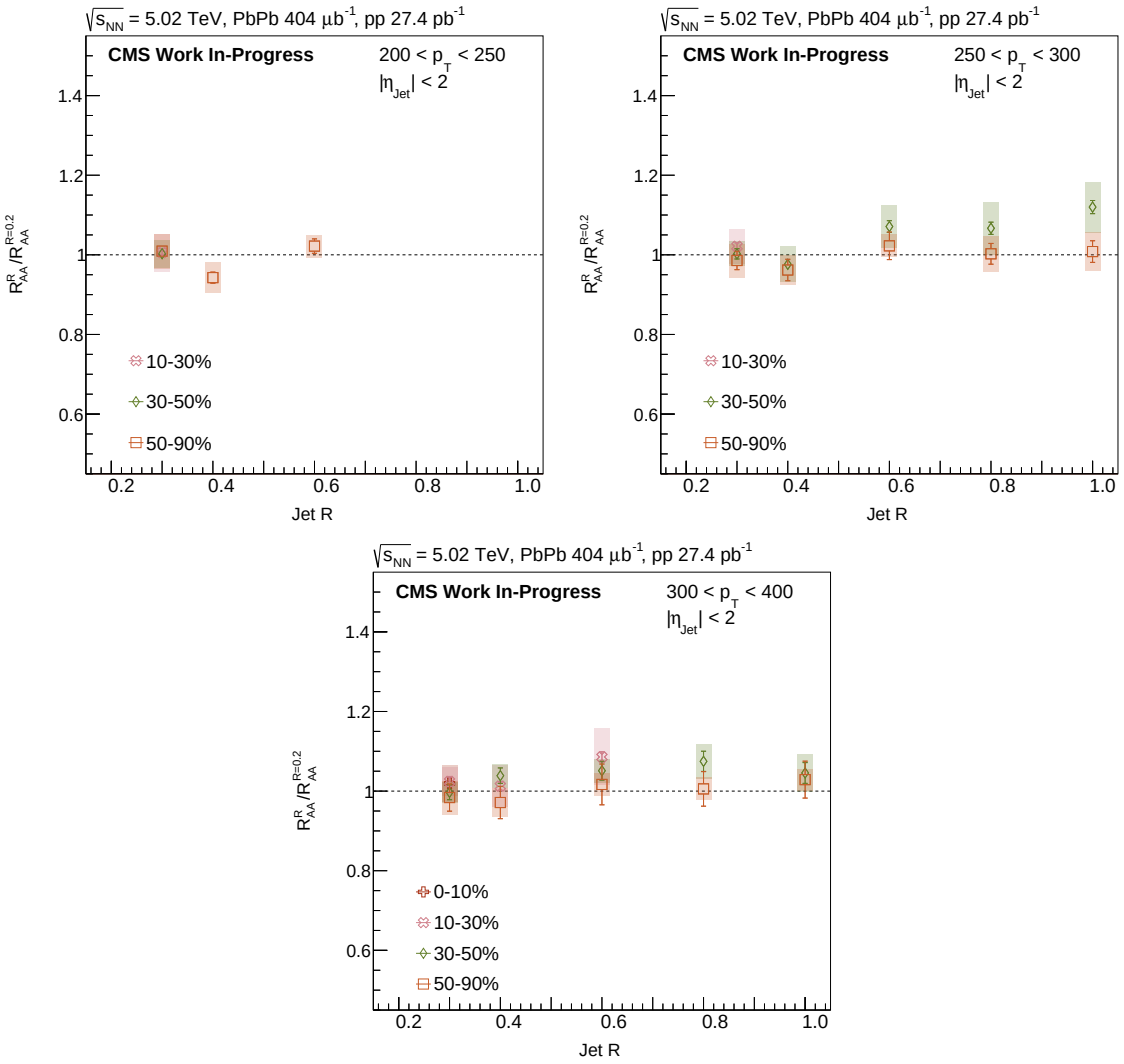

Figure 8-17: The unfolded jet R=0.3−1.0 RAA ratio with RAA R=0.2, using jets reconstructed in pp and PbPb collisions. From left to right, top to bottom, the plots are for $200 < p_{\mathrm{T}} < 250$, $250 < p_{\mathrm{T}} < 300$, and $300 < p_{\mathrm{T}} < 400$. This figure exploits fully shared systematics of TAA and luminosity, along with partially shared scale and resolution errors, for a reduction in systematics. In addition, correlations in statistical errors between large R with R=0.2 is fully accounted for and statistical errors are reduced accordingly.

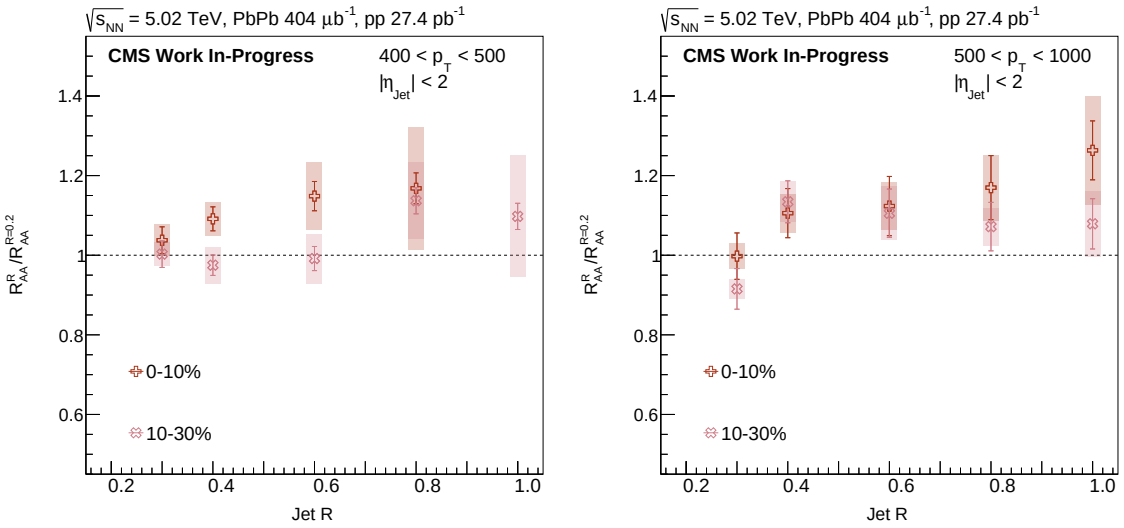

Figure 8-18: The unfolded jet R=0.3−1.0 RAA ratio with RAA R=0.2, using jets reconstructed in pp and PbPb collisions. Left plot is for $400 < p_{\mathrm{T}} < 500$ while right plot is for $500 < p_{\mathrm{T}} < 1000$. This figure exploits fully shared systematics of TAA and luminosity, along with partially shared scale and resolution errors, for a reduction in systematics. In addition, correlations in statistical errors between large R with R=0.2 is fully accounted for and statistical errors are reduced accordingly.

Chapter 9

Conclusions

9.1 Conclusions From Missing Momentum

Jets are reconstructed with anti-k_{T} algorithm for resolution parameter ranging R=0.2 through R=0.5. Dijet pairs passing selection are used in construction of a dijet axis symmetric with respect to both jets, and track transverse momentum are projected onto the dijet axis and summed in bins of angle out to Δ of 2. At bin Δ nearest dijet axis, there is a significant starting asymmetry in both pp and PbPb as would be expected from leading jet selection. Full momentum balance requires large angle sum, in PbPb out to R=2 for selection on dijet asymmetry $A_J >$ .22. The recovery of imbalance in PbPb is preferentially through softer particles when compared to selection and energy matched pp dijet pairs. The implication of the measurement is that the parton-medium interaction redistributes the quenched energy of the jet to large angle and soft particle, rather than say semi-hard particles clustered at cone edge.

Revisiting the big questions of jet physics in medium, the primary impact of the result on the field as whole is a more careful consideration of both soft and hard component of jet insomuch as it pertains to understanding the exact nature of the parton-medium interactions. For example, in first implementations of JEWEL momentum was not conserved and jet energy lost in medium interaction was discarded. While this was sufficient for qualitative replication of macro-jet observables such as

dijet asymmetry, it resulted in significant failures when considering energy flow of event relative to parton on whole. Likewise, Hybrid model jet quenching implementation can replicate jet suppression at R=0.4 without considering recoiling medium, but it is only with the introduction of the recoiling medium that it sees the recovery of momentum in softer, large angle particles. Currently, both the JEWEL and Hybrid model implementation of the recoiling medium are trivial backreaction of immediately interacting particles of the energy loss for momentum conservation, and not induced more complex structures like the wake [43, 45]. The LBT and Co-LBT models include wake like structures and while missing p_{T} cannot distinguish the two cases, neither is currently inconsistent either [47].

Beyond this, radial energy profile study through momentum projection has inspired interest in the large angle distribution of energy, and has lead to jet shape measurements by CMS well beyond the jet cone [48], and preliminary results from ATLAS on long range jet-particle correlations [104]. The long range study of energy flow structure in QGP will in long run tease out exact characteristic of wake structure. Furthermore, long range correlation of particles at intermediate p_{T} ($2 < p_{\mathrm{T}} < 4$ GeV) ranges might tease out the Rutherford picture, as these are more likely to hit a hard scattering center defined by a quasiparticle and backscatter while still being distinguishable above the soft particle background [105]. In contrast, particles at highest-p_{T} likely plow throw hard scattering centers and we should not expect backscatters except in extreme cases.

9.2 Conclusions From Radial Scan of R_{AA}

As yet the implications of large R scan of R_{AA} are unclear. Observed suppression and its reduction going to largest R is in the middle of expectations from JEWEL and Hybrid model implementations of jet energy loss. A direct mapping of R_{AA} result onto dijet-axis momentum or large angle jet shape results are not as simple as naive expectation, as vacuum spectra of jets at different R also changes significantly. Together, the conclusion is that for a fixed population of jets momentum imbalance

can be recovered beyond the cone, but that for increased cone size R, enough jet energy exists at periphery to still be lost beyond the cone from medium interaction.

A careful comparison of theory calculation to data will be necessary for each model, and insomuch as models change when compared to the available predictions, those changes must be clearly stated and understood. However, in contrast with missing p_{T}, this is a pure jet result scanning the radial distribution of jets. As result calculations and comparisons should be on firmer theoretical ground compared to corresponding charged particle maps.

In answering the big questions on medium-parton interaction, we now have a solid map for the angular redistribution of the jet energy that can, in theory, be handled fully perturbatively, without infrared or collinear safetry issues, and minimal additional biases from hadronization. That the R_{AA} itself is not unity at any R suggests that we have not yet reached the Rutherford point where the medium interaction is fully quasiparticle, perturbative in nature, at least if expectation is that very rare in medium hard scatterings would be only remaining process. Of course, even R_{AA} of unity for a particle cone size R is insufficient. As our understanding of the energy deposited in the medium has evolved, we know now that energy lost from the jet that remains local can still be reconstructed as part of the jet, and therefore have no impact on measured R_{AA} despite there being internal modification. As a result, future search at higher energy should couple large R R_{AA} with substructure observables like z_g or jet shapes to determine that the jet is both internally unmodified and that the final state observed production is consistent with scaled vacuum. At this point, we will have mapped the full transition from strong to weak coupling in QGP.

Finally, the large jet R_{AA}, in the commissioning of large jet reconstruction in heavy ions, also opens up significant avenue for future study. While substructure technique is already viable at small jet cone, 10% of the typical light parton energy can be found beyond the cone. In medium, quenching increases the fraction and substructure study can only benefit from larger cone. In a more exotic use case, large cone in vacuum is typically used in the reconstruction of boosted heavy boson or top quark. While the additional reconstruction challenges would be tremendous, a measurement

of hadronic W decay in QGP using boosted jet reconstruction techniques already commissioned and used at CMS for proton-proton collisions would provide give an incredibly valuable data point on relationship between energy loss and mass. The W→cb have sizable mass difference, and per event would travel through an almost identical fraction of medium. In a similar vein, there are already available proposals for top quark as probe to study medium at multiple times t based on decay time of booth top and daughter W [106]. Large cone jet reconstruction will be valuable in this regard as well, and top discovery has already been made in pPb [107] for the first time by CMS.

9.3 Conclusions on Big Questions in Little Plasma

Restating the big questions of the field as concerns the jet program,

1. What is the characteristic energy loss of parton in medium (QCD Bethe-Bloch)?

2. How does collective behavior emerge from an asymptotically free theory such as QCD?

    - Alternatively, we know QCD is asymtotically free at high Q^2, and therefore we should see quasiparticles and Rutherford-like scatterings. Experimentally however, there is so far no evidence. Where is Rutherford hiding?

3. How is the energy lost by jets to the medium redistributed? Is it a trivial medium backreaction, or does it induce more complicated structures such as a wake or mach cone?

In this thesis, we have added significantly to the QCD Bethe-Bloch curve, as we provide the first ever energy loss of partons with characteristic energy broadness of R=1.0. Furthermore, on question 2, we do not see any R_{AA} of unity, much less R_{AA} of unity coupled with no internal structure modification. As such, we deduce that the fully weak regime where the jet is only modified by additional rare scattering off quasiparticle in medium is not yet accessible at current energy. Finally, on the third

question, we now have a map of the energy redistribution in the medium that is not sensitive to collinear or infrared safety issues and is minimally biased by hadronization. As such, we hope by comparing to theory with fixed underlying loss mechanisms but increasing complexity of induced structures in the energy redistribution to medium, to understand whether we have simple backreaction or wake from jets. Future study of large R jet should go to higher-p_{T} and incorporate substructure measurements in order to more fully map the full parton evolution, but as first step we know the limits of the reconstruction and where to go next. Finally, at current date we expect another factor 20 increase in integrated luminosity delivered by LHC at $\sqrt{s_{_{NN}}}$=5.02 TeV for PbPb, which will further aid in search for fully weak regime [108].

List of Figures

List of Tables

Bibliography

[1] U. Heinz *et al.*, "Exploring the properties of the phases of QCD matter - research opportunities and priorities for the next decade,"

[2] W. Busza, K. Rajagopal, and W. van der Schee, "Heavy Ion Collisions: The Big Picture, and the Big Questions," *Ann. Rev. of Nuc. and Particle Science*, vol. 68, 2018.

[3] Y.-J. Lee, A. Yoon, and W. Busza, "http://web.mit.edu/mithig/movies/lhcanmation.mov,"

[4] S. Chatrchyan *et al.*, "Long-range and short-range dihadron angular correlations in central PbPb collisions at $\sqrt{s_{NN}} = 2.76$ TeV," *Eur. Phys. J. C*, vol. 72, p. 10052, 2012.

[5] S. Chatrchyan *et al.*, "Observation of sequential Upsilon suppression in PbPb collisions," *Phys. Rev. Lett.*, vol. 109, p. 222301, 2012.

[6] M. Tanabashi *et al.*, "PDG," *Phys. Rev. D.*, vol. 98, p. 030001, 2018.

[7] J. D. Bjorken, "Energy loss of energetic partons in QGP: possible extinction of high p_{T} jets in hadron-hadron collisions." FERMILAB-PUB-82-059-THY, 1982.

[8] S. Chatrchyan *et al.*, "Observation of Long-Range Near-Side Angular Correlations in Proton-Proton Collisions at the LHC," *JHEP*, vol. 9, p. 91, 2010.

[9] G. Altarelli and G. Parisi, "Asymptotic Freedom in Parton Language," *Nucl. Phys. B*, vol. 126, pp. 298–318, 1977.

[10] Y. L. Dokshitzer, "Calculation of the Structure Functions for Deep Inelastic Scattering and e+ e- Annihilation by Perturbation Theory in Quantum Chromodynamics.," *Sov. Phys. JETP*, vol. 46, 1977.

[11] V. Gribov and L. Lipatov, "Deep inelastic e p scattering in perturbation theory," *Sov. J. Nucl. Phys.*, vol. 15, pp. 438–450, 1972.

[12] R. Baier, Y. L. Dokshitzer, A. Mueller, S. Peign, and S. D., "Radiative energy loss and p⊥ broadening of high energy partons in nuclei," *Nucl. Phys. B*, vol. 484, pp. 265–282, 1997.

[13] B. Zakharov, "Radiative energy loss of high energy quarks in finite-size nuclear matter and quark-gluon plasma," *JETP Lett.*, vol. 65, pp. 615–620, 1997.

[14] P. Arnold, G. D. Moore, and L. G. Yaffe, "Photon Emission from Quark-Gluon Plasma: Complete Leading Order Results," *JHEP*, vol. 0112, p. 009, 2001.

[15] P. Arnold, G. D. Moore, and L. G. Yaffe, "Photon Emission from Ultrarelativistic Plasmas," *JHEP*, vol. 0111, p. 057, 2001.

[16] P. Arnold, G. D. Moore, and L. G. Yaffe, "Photon and Gluon Emission in Relativistic Plasmas," *JHEP*, vol. 0206, p. 030, 2002.

[17] N. Armesto *et al.*, "Comparison of Jet Quenching Formalisms for a Quark-Gluon Plasma "Brick"," *Phys. Rev. C.*, vol. 86, p. 064904, 2012.

[18] K. C. Zapp, F. Krauss, and U. A. Wiedemann, "A perturbative framework for jet quenching," *JHEP*, vol. 03, p. 80, 2013.

[19] J. Casalderrey-Solona, D. C. Gulhan, J. G. Milhano, D. Pablos, and K. Rajagopal, "A hybrid strong/weak coupling approach to jet quenching," *JHEP*, vol. 10, p. 19, 2014.

[20] C. Adler *et al.*, "Evidence from d+Au measurements for final-state suppression of high p_{T} hadrons in Au+Au collisions at RHIC," *Phys. Rev. Lett.*, vol. 91, p. 072304, 2003.

[21] C. Adler *et al.*, "Disappearance of back-to-back high pT hadron correlations in central Au+Au collisions at $\sqrt{s_{NN}}$ = 200 GeV," *Phys. Rev. Lett.*, vol. 90, p. 082302, 2003.

[22] K. Adcox *et al.*, "Suppression of Hadrons with Large Transverse Momentum in Central Au+Au Collisions at $\sqrt{s_{NN}}$ = 130 GeV," *Phys. Rev. Lett.*, vol. 88, p. 022301, 2002.

[23] G. Aad *et al.*, "Observation of a Centrality-Dependent Dijet Asymmetry in Lead-Lead Collisions at $\sqrt{s_{NN}}$= 2.76 TeV with the ATLAS Detector at the LHC," *Phys. Rev. Lett.*, vol. 105, p. 252303, 2010.

[24] S. Chatrchyan *et al.*, "Observation and studies of jet quenching in PbPb collisions at $\sqrt{s_{NN}}$ = 2.76 TeV," *Phys. Rev. C*, vol. 84, p. 024906, 2011.

[25] S. Chatrchyan *et al.*, "Jet momentum dependence of jet quenching in PbPb collisions at $\sqrt{s_{NN}}$ = 2.76 TeV," *Phys. Lett. B*, vol. 712, p. 176, 2012.

[26] S. Chatrchyan *et al.*, "Measurement of jet fragmentation in PbPb and pp collisions at $\sqrt{s_{NN}}$ = 2.76 TeV," *Phys. Rev. C*, vol. 90, p. 024908, 2014.

[27] S. Chatrchyan *et al.*, "Modification of jet shapes in PbPb collisions at $\sqrt{s_{NN}}$ = 2.76 TeV," *Phys. Lett. B*, vol. 730, p. 243, 2014.

[28] S. Chatrchyan *et al.*, "Measurement of transverse momentum relative to dijet systems in PbPb and pp collisions at $\sqrt{s_{NN}}$ = 2.76 TeV," *JHEP*, vol. 01, p. 006, 2016.

[29] S. Chatrchyan *et al.*, "Correlations between jets and charged particles in PbPb and pp collisions at $\sqrt{s_{NN}} = 2.76$ TeV," *JHEP*, vol. 02, p. 156, 2016.

[30] S. Chatrchyan *et al.*, "Decomposing transverse momentum balance contributions for quenched jets in PbPb collisions at $\sqrt{s_{NN}} = 2.76$ TeV," *JHEP*, vol. 11, p. 055, 2016.

[31] S. Chatrchyan *et al.*, "Measurement of inclusive jet cross sections in pp and PbPb collisions at $\sqrt{s_{NN}} = 2.76$ TeV," *Phys. Rev. C*, vol. 96, p. 015202, 2017.

[32] G. Aad *et al.*, "Measurement of the jet radius and transverse momentum dependence of inclusive jet suppression in lead-lead collisions at $\sqrt{s_{NN}} = 2.76$ TeV with the ATLAS detector," *Phys. Lett. B*, vol. 719, p. 220, 2013.

[33] G. Aad *et al.*, "Measurement of the Azimuthal Angle Dependence of Inclusive Jet Yields in Pb+Pb Collisions at $\sqrt{s_{NN}} = 2.76$ TeV with the ATLAS detector," *Phys. Rev. Lett.*, vol. 111, p. 152301, 2013.

[34] G. Aad *et al.*, "Measurements of the Nuclear Modification Factor for Jets in Pb+Pb Collisions at $\sqrt{s_{NN}} = 2.76$ TeV with the ATLAS Detector," *Phys. Rev. Lett.*, vol. 114, p. 072302, 2015.

[35] G. Aad *et al.*, "Measurement of the production of neighbouring jets in lead-lead collisions at $\sqrt{s_{NN}} = 2.76$ TeV with the ATLAS Detector," *Phys. Lett. B*, vol. 751, p. 376, 2015.

[36] G. Aad *et al.*, "Measurement of inclusive jet charged-particle fragmentation functions in Pb+Pb collisions at $\sqrt{s_{NN}} = 2.76$ TeV with the ATLAS detector," *Phys. Lett. B*, vol. 739, pp. 320–342, 2014.

[37] J. Adam *et al.*, "Measurement of charged jet suppression in Pb-Pb collision at $\sqrt{s_{NN}} = 2.76$ TeV," *JHEP*, vol. 30, p. 013, 2014.

[38] J. Adam *et al.*, "Measurement of jet quenching with semi-inclusive hadron-jet distributions in central Pb-Pb collisions at $\sqrt{s_{NN}} = 2.76$ TeV," *JHEP*, vol. 09, p. 170, 2015.

[39] J. Adam *et al.*, "Azimuthal anisotropy of charged jet production in $\sqrt{s_{NN}} = 2.76$ TeV Pb-Pb collisions," *Phys. Lett. B*, vol. 753, pp. 511–525, 2016.

[40] J. Adam *et al.*, "First measurement of jet mass in Pb-Pb and p-Pb collisions at the LHC," *Phys. Lett. B*, vol. 776, pp. 249–264, 2018.

[41] J. Adam *et al.*, "Medium modification of the shape of small-radius jets in central Pb-Pb collisions at $\sqrt{s_{NN}} = 2.76$ TeV," *JHEP*, vol. 10, p. 139, 2018.

[42] J. Casalderrey-Solona, D. C. Gulhan, J. G. Milhano, D. Pablos, and K. Rajagopal, "Predictions for boson-jet observables and fragmentation function ratios from a hybrid strong/weak coupling model for jet quenching," *JHEP*, vol. 3, p. 53, 2016.

[43] J. Casalderrey-Solona, D. C. Gulhan, J. G. Milhano, D. Pablos, and K. Rajagopal, "Angular structure of jet quenching within a hybrid strong/weak coupling model," *JHEP*, vol. 03, p. 135, 2017.

[44] K. C. Zapp, "Jewel 2.0.0 - directions for use," *EPJC*, vol. 74, p. 2762, 2014.

[45] R. K. Elayavalli and K. C. Zapp, "Medium response in jewel and its impact on jet shape observables in heavy ion collisions," *JHEP*, vol. 07, p. 141, 2017.

[46] Y.-T. Chien and I. Vitev, "Towards the understanding of jet shapes and cross sections in heavy ion collisions using soft-collinear effective theory," *JHEP*, vol. 05, p. 23, 2016.

[47] Y. Tachibana, N.-B. Chang, and G.-Y. Qin, "Full jet in quark-gluon plasma with hydrodynamic medium response," *Phys. Rev. C*, vol. 95, p. 044909, 2017.

[48] S. Chatrchyan *et al.*, "Jet properties in PbPb and pp collisions at $\sqrt{s_{NN}} = 5.02$ TeV," *JHEP*, vol. 05, p. 006, 2018.

[49] G. Aad *et al.*, "Comparison of fragmentation functions for light-quark- and gluon-dominated jets from pp and Pb+Pb collisions in ATLAS," *Submitted to Phys. Rev. Lett.*, 2019.

[50] S. Chatrchyan *et al.*, "Study of jet quenching with Z+jet correlations in PbPb and pp collisions at $\sqrt{s_{NN}} = 5.02$ TeV," *Phys. Rev. Lett.*, vol. 119, p. 082301, 2017.

[51] G. Aad *et al.*, "Measurement of photon-jet transverse momentum correlations in $\sqrt{s_{NN}} = 5.02$ Pb+Pb and pp collisions with ATLAS," *Phys. Lett. B*, vol. 789, p. 167, 2019.

[52] S. Chatrchyan *et al.*, "Measurement of the splitting function in pp and PbPb collisions at $\sqrt{s_{NN}} = 5.02$ TeV," *Phys. Rev. Lett.*, vol. 120, p. 142302, 2018.

[53] J. Adam *et al.*, "Exploration of jet substructure using iterative declustering in pp and Pb-Pb collisions at LHC energies," *Submitted PLB*, 2019.

[54] S. Chatrchyan *et al.*, "Charged-particle nuclear modification factors in PbPb and pPb collisions at $\sqrt{s_{NN}} = 5.02$ TeV," *JHEP*, vol. 04, p. 039, 2017.

[55] G. Aad *et al.*, "Measurement of the nuclear modification factor for inclusive jets in Pb+Pb collisions at $\sqrt{s_{NN}} = 5.02$ TeV with the ATLAS Detector," *Phys. Lett. B*, vol. 790, p. 108, 2019.

[56] M. Spousta and B. Cole, "Interpreting single jet measurements in pbpb collisions at the lhc," *Eur. Phys. Journal C*, vol. 76, p. 50, 2016.

[57] J. Adam *et al.*, "Measurement of jet suppression in central Pb-Pb collision at $\sqrt{s_{NN}} = 2.76$ TeV," *Phys. Lett. B*, vol. 746, p. 1, 2015.

[58] G. Aad *et al.*, "Measurement of jet pT correlations in Pb+Pb and pp collisions at $\sqrt{s_{NN}} = 2.76$ TeV with the ATLAS Detector," *Phys. Lett. B*, vol. 774, p. 379, 2017.

[59] S. Chatrchyan *et al.*, "Measurement of inclusive jet production and nuclear modifications in pPb collisions at $\sqrt{s_{NN}} = 5.02$ TeV," *Eur. Phys. J. C*, vol. 76, p. 372, 2016.

[60] G. Aad *et al.*, "Centrality and rapidity dependence of inclusive jet production in $\sqrt{s_{NN}} = 5.02$ TeV proton-lead collisions with the ATLAS detector," *Phys. Lett. B*, vol. 748, pp. 392–413, 2015.

[61] J. Adam *et al.*, "Constraints on jet quenching in p-Pb collisions at $\sqrt{s_{NN}} = 5.02$ TeV measured by the event-activity dependence of semi-inclusive hadron-jet distributions," *Phys. Lett. B*, vol. 783, p. 95, 2018.

[62] J. Adam *et al.*, "Measurement of charged jet cross section in pp collisions at $\sqrt{s_{NN}} = 5.02$ TeV," *Submitted PRD*, 2019.

[63] S. Chatrchyan *et al.*, "Measurement of jet fragmentation into charged particles in pp and PbPb collisions at $\sqrt{s_{NN}} = 2.76$ TeV," *JHEP*, vol. 10, p. 087, 2012.

[64] S. Chatrchyan *et al.*, "Evidence of b-jet quenching in PbPb collisions at $\sqrt{s_{NN}} = 2.76$ TeV," *Phys. Rev. Lett.*, vol. 113, p. 132301, 2014.

[65] S. Chatrchyan *et al.*, "Comparing transverse momentum balance of b jet pairs in pp and PbPb collisions at $\sqrt{s_{NN}} = 5.02$ TeV," *JHEP*, vol. 03, p. 181, 2018.

[66] S. Chatrchyan *et al.*, "Studies of jet quenching using isolated-photon+jet correlations in PbPb and pp collisions at $\sqrt{s_{NN}} = 2.76$ TeV," *Phys. Lett. B*, vol. 718, p. 773, 2012.

[67] S. Chatrchyan *et al.*, "Study of jet quenching with isolated-photon+jet correlations in PbPb and pp collisions at $\sqrt{s_{NN}} = 5.02$ TeV," *Phys. Lett. B*, vol. 785, p. 14, 2018.

[68] S. Chatrchyan *et al.*, "Observation of medium induced modifications of jet fragmentation in PbPb collisions at $\sqrt{s_{NN}} = 5.02$ TeV using isolated-photon-tagged jets," *Phys. Rev. Lett.*, vol. 121, p. 242301, 2018.

[69] S. Chatrchyan *et al.*, "Jet shapes of isolated photon-tagged jets in PbPb and pp collisions at $\sqrt{s_{NN}} = 5.02$ TeV," *Phys. Rev. Lett.*, vol. 122, p. 152001, 2019.

[70] S. Chatrchyan *et al.*, "Measurement of the groomed jet mass in PbPb and pp collisions at $\sqrt{s_{NN}} = 5.02$ TeV," *JHEP*, vol. 10, p. 161, 2018.

[71] C. Collaboration, *CMS Physics: Technical Design Report Volume 1: Detector Performance and Someftware*. Technical Design Report CMS, Geneva: CERN, 2006. There is an error on cover due to a technical problem for some items.

[72] A. M. Sirunyan *et al.*, "Particle-flow reconstruction and global event description with the CMS detector," *JINST*, vol. 12, p. P10003, 2017.

[73] T. Sjöstrand, S. Mrenna, and P. Skands, "PYTHIA 6.4 physics and manual," *JHEP*, vol. 05, p. 026, 2006.

[74] T. Sjostrand, S. Mrenna, and P. Z. Skands, "A Brief Introduction to PYTHIA 8.1," *Comput. Phys. Commun.*, vol. 178, pp. 852–867, 2008.

[75] T. Sjostrand, S. Mrenna, and P. Z. Skands, "Parton Fragmentation and String Dynamics," *Phys.Rept.*, vol. 97, pp. 31–145, 1983.

[76] I. P. Lokhtin and A. M. Snigirev, "A model of jet quenching in ultrarelativistic heavy ion collisions and high-p_T hadron spectra at RHIC," *Eur. Phys. J.*, vol. C45, p. 211, 2006.

[77] R. Brun, F. Carminati, and S. Giani, "GEANT Detector Description and Simulation Tool," 1994.

[78] A. Tapper and Darin Acosta, "Cms technical design report for the level-1 trigger upgrade," *Technical Design Report CMS*, vol. CMS-TDR-12, 2013.

[79] A. Collaboration, "Performance of the ALEPH detector at LEP," *Nucl. Instrum. Meth. A*, vol. 611, p. 25, 2009.

[80] G. Aad *et al.*, "Jet reconstruction and performance using particle flow with the atlas detector," *Eur. Phys. J. C*, vol. 77, p. 466, 2017.

[81] F. R. Rene Brun, "Root âĂŤ an object oriented data analysis framework," *Nucl. Inst. and Meth. in Phys. Res. A*, vol. 389, no. 1–2, pp. 81–86, 1997.

[82] S. Chatrchyan *et al.*, "Pseudorapidity distributions of charged hadrons in xenon-xenon collisions at $\sqrt{s_{NN}} = 5.44$ TeV," *Submitted PLB*.

[83] M. Cacciari, G. P. Salam, and G. Soyez, "The anti-k_t jet clustering algorithm," *JHEP*, vol. 04, p. 063, 2008.

[84] M. Cacciari and G. P. Salam, "Dispelling the n^3 myth for the kt jet-finder," *Phys.Lett.B*, vol. 641, pp. 57–61, 2006.

[85] M. Cacciari, G. P. Salam, and G. Soyez, "Fastjet user manual," Nov. 2011.

[86] M. Cacciari, G. P. Salam, and G. Soyez, "Softkiller, a particle-level pileup removal method," *Eur. Phys. J. C*, vol. 75, p. 59, 2015.

[87] CMS Collaboration, "Pileup removal algorithms," *CMS Physics Analysis Summary*, vol. CMS-PAS-JME-14-001, 2014.

[88] "Updates to constituent subtraction in heavy ions at cms," *CMS Detector Performance Summary*, vol. CMS-DP-2018-024, 2018.

[89] M. L. N. T. Daniele Bertolini, Philip Harris, "Pileup per particle identification," *JHEP*, vol. 1410, p. 59, 2014.

[90] O. Kodolova, I. Vardanian, A. Nikitenko, and A. Oulianov, "The performance of the jet identification and reconstruction in heavy ions collisions with CMS detector," *Eur. Phys. J. C*, vol. 50, p. 117, 2007.

[91] M. Cacciari and G. P. Salam, "Pileup subtraction using jet areas," *Phys.Lett.*, vol. B659, pp. 119–126, 2008.

[92] "Underlying-event subtraction for particle flow," *CMS Detector Performance Summary*, vol. CMS-DP-2013-018, 2011.

[93] P. Berta, M. Spousta, D. W. Miller, and R. Leitner, "Particle-level pileup subtraction for jets and jet shapes," *JHEP*, vol. 6, p. 92, 2014.

[94] P. Berta, L. Masetti, D. W. Miller, and M. Spousta, "Pileup and Underlying Event Mitigation with Iterative Constituent Subtraction," 2019.

[95] M. Cacciari, G. P. Salam, and G. Soyez, "The Catchment Area of Jets," *JHEP*, vol. 0804, p. 005, 2008.

[96] S. Chatrchyan *et al.*, "Non-Gaussian elliptic-flow fluctuations in PbPb collisions at $\sqrt{s_{NN}} = 5.02$ TeV," *Phys. Lett. B*, vol. 789, p. 643, 2019.

[97] P. T. Komiske, E. M. Metodiev, B. Nachman, and M. D. Schwartz, "Pileup Mitigation with Machine Learning (PUMML)," *JHEP*, vol. 12, p. 051, 2017.

[98] M. L. Miller, K. Reygers, S. J. Sanders, and P. Steinberg, "Glauber modeling in high energy nuclear collisions," *Ann. Rev. Nucl. Part. Sci.*, vol. 57, pp. 205–243, 2007.

[99] T. Adye, "Unfolding algorithms and tests using RooUnfold," 2011.

[100] G. D'Agostini, "A multidimensional unfolding method based on Bayes' theorem," *Nucl. Instrum. Meth. A*, vol. 362, no. 2–3, pp. 487–498, 1995.

[101] S. Chatrchyan *et al.*, "Constraining gluon distributions in nuclei using dijets in proton-proton and proton-lead collisions at $\sqrt{s_{NN}} = 5.02$ TeV," *Phys. Rev. Lett.*, vol. 121, p. 062002, 2018.

[102] L. C. Liliana Apolinario, Nestor Armesto, "An analysis of the influence of background subtraction and quenching on jet observables in heavy-ion collisions," *JHEP*, vol. 02, p. 022, 2013.

[103] S. Chatrchyan *et al.*, "Measurement of the ratio of inclusive jet cross sections using the anti-kt algorithm with radius parameters R = 0.5 and 0.7 in pp collisions at $\sqrt{s_{NN}} = 7$ TeV," *Phys. Rev. D*, vol. 90, p. 072005, 2014.

[104] G. Aad *et al.*, "Measurement of angular and momentum distributions of charged-particles within and around jets in Pb+Pb and pp collisions at $\sqrt{s_{NN}}$= 5.02 TeV with the ATLAS at the LHC," 2018.

[105] F. D'Eramo, K. Rajagopal, and Y. Yin, "MoliÃĺre Scattering in Quark-Gluon Plasma: Finding Point-Like Scatterers in a Liquid," *JHEP*, vol. 01, p. 172, 2019.

[106] G. P. S. C. A. S. Liliana Apolinario, Jose Guilherme Milhano, "Probing the time structure of the quark-gluon plasma with top quarks," *Phys. Rev. Lett.*, vol. 120, p. 232301, 2018.

[107] S. Chatrchyan *et al.*, "Observation of top quark production in proton-nucleus collisions," *Phys. Rev. Lett.*, vol. 119, p. 242001, 2017.

[108] Z. Citron *et al.*, "Future physics opportunities for high-density QCD at the LHC with heavy-ion and proton beams,"